-

Institute for Materials Research
School of Process, Environmental
& Materials Engineering

High-speed imaging and computational modelling of close-coupled gas atomization

Shahed Motaman

Submitted in accordance with the requirement for the degree of
Doctor of philosophy
University of Leeds
Institute for Materials Research
School of Process, Environmental and Materials Engineering
December 2013

The candidate confirms that the work submission is his own, except where work, which has formed part of jointly authored publications, has been included. The contribution of the candidate and the other authors to this work has been explicitly indicated below.

The published papers were edited and revised in a good proof of english by Prof. Andrew M. Mullis and Dr. Duncan Borman.

The above collaboration resulted in three jointly authored publications listed below, where the papers have been written by the author. This work is the authors own analysis of data. This is summarized below.

Chapter 6.3.2 use of CFD for analyzing the effect of melt nozzle tip length and Prof. Andrew M. Mullis and Dr. Duncan Borman have analyzed mismatch angle of external wall on flow separation. In addition, the PLI image of back stream flow in figure 96 has been taken from PhD thesis of “Optical investigation into close-coupled gas atomization”, University of Leeds by Ian N. McCarthy.

1- S.Motaman, A.M.Mullis, R.Cochrane and D.Borman, Use of computational modelling for investigating the effect of melt delivery nozzle tip length on gas flow separation in supersonic gas atomization. ICLASS; 12th Triennial International Conference on Liquid Atomization and Spray Systems; Heidelberg; Germany; September 2012.

2- S.Motaman, A.M.Mullis, R.Cochrane, D.Borman, The effect of melt nozzle geometry on close-coupled gas atomization. International Conference on Powder Metallurgy & Particulate Materials 2012; 10-13 June 2012, Nashville, TN, CD proceedings ISBN: 978-9853397-2-2; MPIF 2012; 02/01-02/12.

3- S.Motaman, A.M.Mullis, R.Cochrane, D.Borman, I.N. McCarthy, Numerical and experimental modelling of back stream flow during close-coupled gas atomization, Journal of Computers & Fluids, **vol** 88, pp.1-10, 2013.

The candidate confirms that the work submitted is his own and that appropriate credit has been given where reference has been made to the work of others.

Acknowledgments

Foremost, I would like to express my sincere gratitude to my advisors Prof. Andrew Mullis, Dr Robert Cochrane and Dr Duncan Borman for the continuous support of my PhD study and research, for his patience, motivation, enthusiasm, and immense knowledge. Their guidance helped me in all the time of research and writing of this thesis. Also, many thanks to my technician, Diane Cochrane and Mr Robert Simpson , for their expert advice on the many technical aspects of this project.

On a personal note, I would like to thank specially my devoted wife Niloofar, who without her support and patience; I could not have completed this project.

Finally, my Special thanks and love also goes to my son Mehrsam, my parents Siroos and Behrokh and my parent-in-law Shahnaz and pedar Mohammad ali who have offered their unflinching support and constant encouragement throughout this work.

To Professor ‘Salahedin Ali Nader Angha’
for his inspiration

Abstract

Gas atomization process, especially Closed Coupled Gas Atomization (CCGA) is a very efficient processing method to produce ultra fine, spherodised metal powders. In this process, the high-pressure gas jet is used to disintegrate the molten metal stream in to the spherical powders. Due to hydrodynamic and thermal interaction between high-pressure gas jet and molten metal stream especially near melt delivery nozzle, this technique is very complex and challenging for atomization industries.

Melt delivery nozzle design is one of the key factors to control powders properties. The optical Schlieren technique and analogue water atomizer along with Computational Fluid Dynamics (CFD) numerical methods are practical methods for observing the single or two-phase flow of gas-metal interaction during CCGA.

This research is focused on the optical Schlieren and numerical CFD techniques to observe single-phase gas flow behaviour with different melt nozzles tip design and gas dies profile. The CFD numerical results are validated by the experimental Schlieren test results. The effect of melt tip design on open to closed-wake condition near melt nozzle was investigated. Comparing the CFD velocity field and velocity streamlines of different nozzle design at different atomization gas pressure could help to propose a new hypothesis of how open to closed-wake condition occurs at different nozzle tip design. In addition, the flow separation problem around melt nozzle by two different gas die systems was investigated. The results showed there are two major mechanisms for this phenomenon, which depends on gas die system set-up, melt nozzle tip protrusion length and mis-match angle of external nozzle wall to the gas jet direction.

Table of Contents

List of figures

List of Table

Abbreviations

AS-CF: Annular Slit Confined Feed

CCGA: Close-Coupled Gas Atomization

CFD: Computational Fluid Dynamics

C-D: Convergent-Divergent

DJ-CF: Discrete Jet Confined Feed

DJPI: Discrete Jet Pressure Inversion

DES: Direct Numerical Simulation

FVM: Finite Volume Method

FEM: Finite Element Method

FDM: Finite Difference Method

HPGA: High Pressure Gas Atomization

LES: Large Eddy Simulation

MIM: Metal Injection Modelling

PM: Powder Metallurgy

PLI: Pulse Laser Imaging

RANS: Reynolds Averaged Navier-Stokes

RNG: Re-Normalise Group

SST: Shear Stress Transport

USGA: Ultrasonic Gas Atomiser

WCP: Wake Closure Pressure

List of symbols

Symbol	Description and Unit
u_r	Relative velocity between the liquid and gas (m s^{-1})
ρ_A	Density of gas (kg m^{-3})
d_0	Diameter of liquid column (m)
W_{eA}	Aerodynamic Weber number (dimensionless)
σ	Liquid surface tension (N m^{-1})
$\frac{A}{A_t}$	Ratios of exit to throat area of C-D (dimensionless)
Υ	Ratio of specific heat capacities (dimensionless)
M	Mach number (dimensionless)
λ	Light wavelength (m)
n	Light reflective index (dimensionless)
G (λ)	Gladstone-Dale number (kg^{-1} m^{3})
υ_L	Liquid kinematic viscosity (m^{2} s^{-1})
M	Liquid mass flow rate (kg s^{-1})
A	Air mass flow rate (kg s^{-1})
d	Diameter of the melt nozzle (m)
v_g	Kinematic viscosity of gas (m^{2} s^{-1})
b	Constant which depends on atomization situation
u_g	Gas velocity (m s^{-1})
d_{50}	Mass median diameter (m)
We	Weber number (dimensionless)
D	Mean particle diameter (m)
r	Average powders radius (m)
$\frac{P_s}{P_m}$	The ratio of input and output power (dimensionless)
ρ	Fluid density (kg m^{-3})
u	Fluid velocity (m s^{-1})
p	Pressure (Pa)
T	Total stress tensor

Symbol	**Description and Unit**
f	Body force per unit (kg m s^{-2})
$\hat{u}_{i}$	Average fluid velocity components at x_i (m s^{-1})
$\hat{u}_{j}$	Average fluid velocity components at x_j (m s^{-1})
$\hat{p}$	Average static pressure (Pa)
$\hat{v}_{ij}$	Average viscous stress (kg $s^{-1}m^{-1}$)
U_i	Mean motion velocity at x_i (m s^{-1})
p	Mean motion pressure (Pa)
v	Mean motion viscous stress (kg $s^{-1}m^{-1}$)
u_i	Fluctuating velocity component (m s^{-1})
p_v	Fluctuating pressure component (Pa)
τ_{ij}	Fluctuating viscous component (kg $s^{-1}m^{-1}$)
K	Kelvin temperature
K	Turbulent kinetic energy
ε	Turbulent dissipation
ω	Specific dissipation
t	Time (s)
v	Viscous stress (kg $s^{-1}m^{-1}$)
g	Earth's standard acceleration due to gravity (m s^{-2})
R_u	Universal gas constant
ϑ_m	Molecular mass of air
u_{sound}	Speed of sound (m s^{-1})

1 Introduction

Metal powders have been widely used for producing different metal parts in powder metallurgy (PM) companies over the recent seventy years. The first industries that used metal powders in the 1900' s were lighting industries, which produced tungsten filament for bubble light; and since then, the use of metal powders products have been gradually growing among different industries [1]. The range of using these products vary from Metal Injection Moulding (MIM) for complex carrier gear sets in automobile gearbox and self-lubricating bearings to the high strength powder-forged rods. The estimated production of metal powders is about 1 million tonnes per year worldwide [1]. Automobile companies consume the largest amounts of these products. The annual sale of PM industries was around £19.5 billion by 2012 worldwide [1]. These ranges of annual sales have been obtained regarding to the economical recession worldwide in the recent years. Significant development of the modern technology in different areas of the manufacturing such as pigmentation, catalysis, and MIM industries; which require high degree of purity of metal powders and powder size as fine as 10 µm, result in many challenges for PM industries. Some of the problems, which PM industries face with, are listed as follows:

1- Producing exceptionally fine powders with an average particle diameter less than 10 µm with the low particulate size distribution, which may increase both the energy consumption and the price of the final product.

2- Highly-purified powders for specific application. Existence of impurities in the molten metal during powders solidification act as heterogeneous nucleation and cause low under cooling solidification, where metal stable phase formation is required.

There are different ways for producing metal powders such as crushing, casting or melting atomization methods and each of these processes has some advantages and disadvantages [2]. However, most of metal powders are produced via atomization due to production of finer powders and higher solidification rate. Two of the well-known commercial atomization methods for producing metal powders are:

- Water atomization
- Gas atomization

Each of the above-mentioned processes is different in design and is used for producing a specific size and shape of metal powders. Some parameters such as powder size, energy cost, powder properties and powder uniformity are the main factors, which commercial atomizers consider for choosing one of the above-mentioned methods [2, 3]. The melt atomizer covers a wide range of metals from low melting point like tin, lead, and aluminium to the high melting point such as stainless steel and titanium [3]. There are different melt atomizer types in use and the vast majority of them are categorised as two-phase fluid atomizers. Due to the type of second fluid used to break-up the molten metal; either water or gas, these categories of melt atomizers are widely used in the commercial melt atomizers [2, 3, 4].

1.1 Water atomization

In this process, the molten metal is disintegrated by the direct impact of high velocity and high-pressure water jet and powder droplets become solidified during a large heat exchange with water [5]. Then, the solidified particles are collected at the bottom of the collecting tank. Figure 1 shows the schematic view of this process.

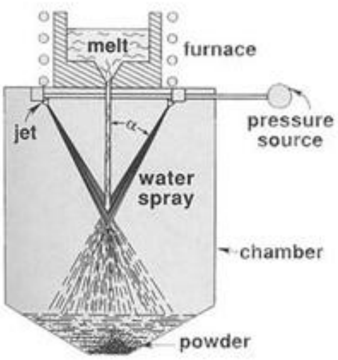

Figure 1. The schematic view of water atomization process [5].

The most pronounced parameters in this process for controlling the particle size distribution are viscosity and surface tension of molten metal. In addition, the controlling factors of the atomization operation are water jet velocity and pressure [5, 6]. Increasing the water jet velocity, pressure and jet angle of α (In figure 1) combined with the low melt viscosity and surface tension may lead to the fine particles with size of less than 40µm [6,7].

The high thermal conductivity of the water causes heat to dissipate faster from molten metal and increases the solidification rate. Other variables such as water/melt ratio and atomization chamber atmosphere may also affect the outcome, but are of less significance [7]. Despite the fact that, the lower cost of this process compared to the other atomization techniques is an advantage, the shape of the particles is reasonably irregular. Furthermore, unlike the other melt atomization methods which use inert gas as the second phase of melt break-up, some problems such as surface oxidation and low tap density (which is defined as density of packed powder) make this process unsuitable for reactive metals [7, 8]. Figure 2 shows the lead powders shape achieved by the water atomization.

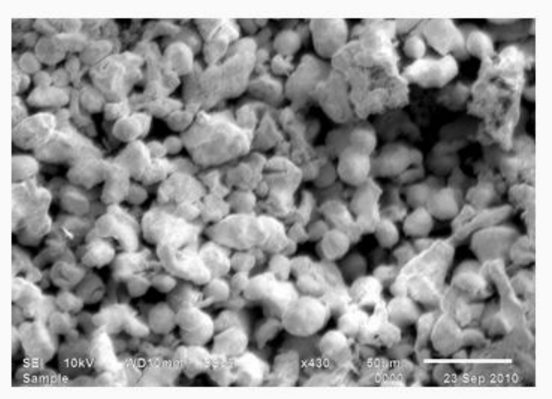

Figure 2. The irregular lead powders achieved by the water jet atomization [7].

1.2 Gas atomization

The gas atomization process is employed to produce a wide variety of ultra fine and highly spherical metal powders and alloys (Figure 3) [8]. In this process, the molten metal pours from a tundish, which acts as a reservoir to control the flow rate of metal into the atomization chamber. The chamber consists of the melt delivery nozzle and the gas die. At this chamber, the liquid metal is disrupted by the direct impact of the high velocity gas jet such as air, nitrogen, or argon just below the melt delivery nozzle tip, and the melt droplets are solidified to form of spherical particles [8].

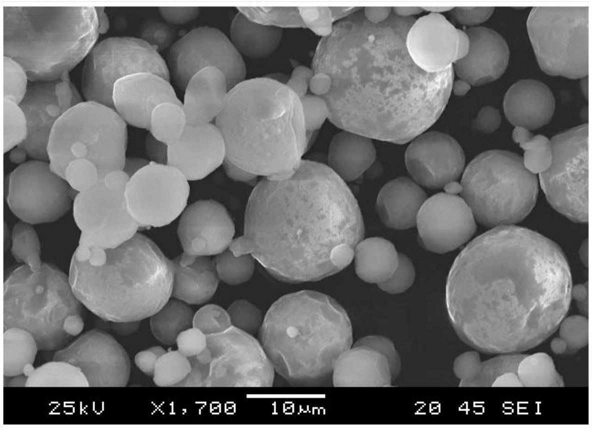

Figure 3. Copper powders produced by the gas atomization process [7].

Selection of gas type depends on the metal properties in respect to prevention of metal oxidation. Due to the high cooling rate (10^2 to 10^5 K s^{-1}) of melt solidification, powders have a refined microstructure and homogeneity including improved structural and chemical properties [8].

Because of complexity of the gas atomization process and a deficiency of knowledge about the gas and melt interaction behaviour there are many unknown issues about this process. However, this method is still the most practical method for producing high quality metal powders and still is more an “art” than a science [9, 11]. There are two general methods for the gas atomization process; free-fall and Close-Coupled Gas Atomization (CCGA).

In the free-fall atomization, the molten metal falls a short distance from the melt delivery nozzle under gravity before being broken apart by impinging the high velocity gas jet. A positive aspect of the free-fall design is easier controlling of the gas and melts interaction compared to the CCGA design. On the other hand, in the free-fall designs, the particle size distribution is difficult to control and the process efficiency is lower than CCGA [8, 9]. As such, most commercial atomizer companies prefer to choose a CCGA process. In this method, the molten metal wets the whole tip of the melt delivery nozzle circumference by ‘pre-filming’ mechanism. After that, the melt is disrupted by the direct impact of the high velocity gas jet just below the melt delivery nozzle tip, forming melt droplets, which subsequently are solidified to form the spherical particles.

Due to the close proximity between the gas die exit jet area and the melt delivery nozzle in the CCGA, the melt ligament can be more efficiently disrupted by the gas jet compared to the free-fall atomization process. This minimizes the dissipation of the gas energy, and as a result of that, the particles are finer in size and the process is more efficient in energy consumption than free-fall. Figures 4 and 5 show a schematic view of the free-fall and the CCGA processes.

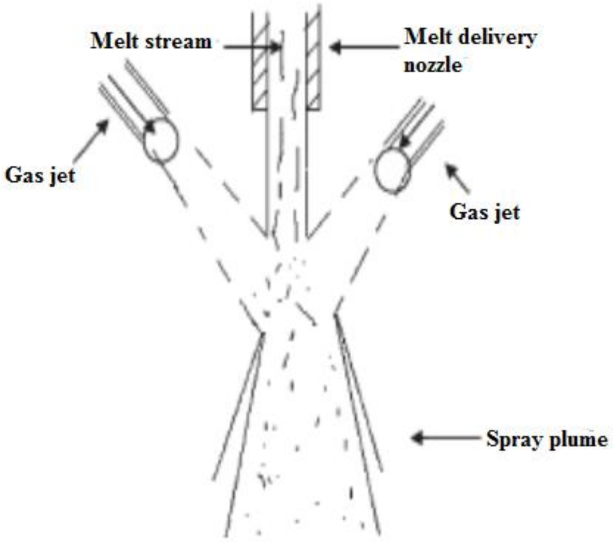

Figure 4. A sketch of a free-fall gas atomization process [6]

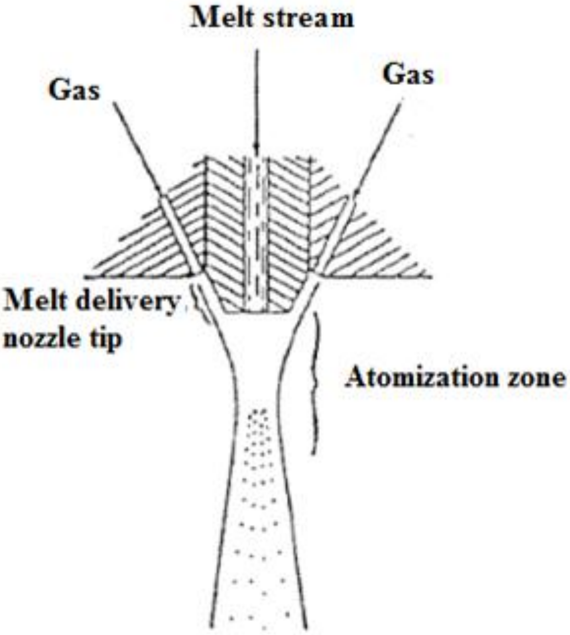

Figure 5. A sketch diagram of CCGA process [6]

1.3 Objectives

This thesis investigates the CCGA process through physical and mathematical modelling of the process, particularly focusing on the gas flow behaviour around the melt delivery nozzle; and the influence of changing key physical design parameters such as the effect of changing the melt nozzle internal design on the gas flow behaviour. The main objectives of this research can be listed as follows:

- To physically investigate the single-phase gas flow using an analogue atomizer and optical Schlieren technique to further understanding of the gas flow behaviour regarding to melt nozzle tip design variation.

- To improve understanding of the melt delivery nozzle tip design effect on the gas wake condition around the melt nozzle with the numerical modelling and validate the numerical results (and predictions) with those from physical experiments.

- Through undertaking a comprehensive mathematical simulation, provide further understanding of the important factors that need to be considered during open and closed-wake condition and proposing a new model for open to closed-wake condition occurrence at different melt nozzle tip design.

- Use of mathematical modelling to investigate the gas flow separation around the melt nozzle during CCGA.

2 Literature review

In order to present a better overview on the scientific aspect of CCGA, the literature review splits into three parts. The first part deals with the fundamental science of the melt liquid primary and secondary break-up mechanism. The second part discusses the gas flow behaviour, optical visualization technique to observe the gas flow field such as Schlieren method and melt/gas nozzle design specification. At the last part, the mathematical modelling of the single-phase gas flow modelling at the CCGA process is also discussed.

As mentioned in the previous chapter, producing the ultra-fine metal powders with small standard deviation and a high level of purity with the CCGA requires a comprehensive understanding of the parameters controlling this process. The early research conducted into gas atomization, especially CCGA process, was started around 1948 [10]. Although, these studies started over 64 years ago, this method still is not fully understood. The other reason for the surprisingly few investigations and published papers about this process is that the commercial powder companies do not reveal their knowledge and details of atomization process, and such information is confidential. Therefore, investigation on the real powder atomizer is one of the main problems for researchers. Additionally, due to the above-mentioned problems, the cost of the research and investigation on this process is also too high [10, 11].

2.1 Melt break-up at the gas atomization process

In the gas atomization process, the bulk liquid ligament converts to the small droplets with different sizes and shapes that may vary from spherical to irregular shape. One of the reasons that cause the particles form in a spherical shape during atomization is surface tension [12]. In addition, temperature has a direct influence on the surface tension and as it increases, the surface tension decreases and vice versa [11, 12].

Different physical factors including surface tension, viscosity, and density influence the droplet size after emerging from nozzle orifice at the gas atomization. The liquid metal with higher surface tension has a larger average droplet size than the liquid metal with a lower surface tension [12].

Viscosity is another factor that affects the liquid break-up. Increasing the viscosity tends to prevent liquid break-up leading to a larger average particle size distribution [13, 14].

Density causes the liquid to resist against acceleration. Generally, the liquid with a higher density has a larger average particle size distribution during the gas atomization process [14].

2.1.1 Primary break-up

Normally, the gas atomization of liquid metals with the high-velocity gas jet consists of four steps: 1-Ligament formation; 2-Atomizing of liquid ligament to liquid droplets, which is known as primary break-up; 3-Breaking liquid droplets to the smaller drops known as secondary break-up; and 4-Spherodising and cooling liquid droplets to solidify powders.

Savart conducted the early modern study of droplets formation in 1833 [15]. He was the first person that proposed the laws governing liquid column break-up. Although, experimental observation of liquid break-up requires some photographic techniques; since the timescale in which it is taking place is so short, but Savart could extract some accurate and remarkable series of images of this process just with naked eyes [15]. To do this, he moved a black belt, interrupted by narrow white stripes in a parallel direction of jet. This method leaded an effective stroboscopic observation of the gas jet [15]. Figure 6 shows the early observations of Savart on liquid break-up. The crucial role of the surface tension at liquid disintegration was investigated by Plateau in 1849 [16] who introduced “Plateau tank” for elimination of the gravity effect on his study.

Figure 6. The early image of Savart’s observation on 6 mm in diameter liquid jet break-up [15].

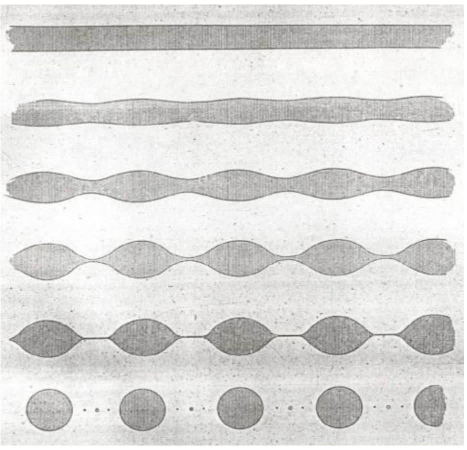

Figure 7. The schematic image of liquid column break-up of oil suspended in a mixture of water and alcohol observed by Plateau [16].

His early sketch of investigation on the break-up process of viscous fluid of oil in the mixture of alcohol and water is depicted in figure 7. In 1879, Plateau investigations were followed by Lord Rayleigh [17] who added the flow dynamics to the description of the break-up process. He proposed the liquid break-up is the consequence of the hydrodynamic instability [17]. He also observed the liquid disintegration mechanism by injecting the liquid column in to the ambient gas chamber. Rayleigh’s investigations were developed by other people such as Eotvos (1886) [18], Quincke (1877) [19], Lenard (1887) [20], and Bohr (1909) [21].

According to the previous studies and observations [21, 22], the liquid break-up occurs by one of the following four mechanisms of:

- Liquid dripping
- Liquid column break-up
- Liquid films break-up
- Liquid ligament break-up

In all of these four mentioned mechanisms; which are known as primary break-up, the bulk of liquid stream is broken into the small droplets.

2.1.1.1 Liquid dripping

This mechanism is unlikely to occur in the gas atomization process; due to the gravity force, which is the less effective on liquid break-up at this process. The break-up process at the gas atomization is normally more justified by the combination of three above mentioned mechanisms.

2.1.1.2 Liquid column break-up

This mechanism is mostly observed on the low gas pressure condition on both free-fall and CCGA. This method was first observed by Rayleigh [17], then this mechanism was expanded via different methods by Kuehn (1925) [22], Weber (1931) [23], and DeJuhasz et al. (1931) [24]. Also, Laufer (1950) [25] and Ranz (1956) [26] had some investigations on the behavior of turbulent single-phase jet on liquid column break-up, while Tennekes & Lumley (1972) [27], Hinze (1975) [28] and Schlichting (1979) [29], reviewed and reported similar work. All of these researchers had agreed about this break-up mechanism and these studies were modified by Meister & Koowalewski (1992) [30]. Moreover, Fargo & Chigier (1992) [31] used high speed imaging technique to reveal various flow conditions of aerodynamic 'Weber number' (W_{eA}) and break-up mechanism. This can be shown as below:

$$W_{eA} = \frac{\rho_A \ \mathrm{d}_0 \ u_r^{\ \mathbf{2}}}{\sigma} \qquad (1)$$

Where u_r is relative velocity between the liquid and gas (m s^{-1}) , ρ_A is the density of gas (kg m^{-3}), d_0 is diameter of liquid column (m); and σ is liquid surface tension (N m^{-1}). Based on the Weber number variation, they classified the liquid break-up into the three main categories of; (1) $0 < W_{eA} < 25$ is known as Rayleigh type break-up or normal pulsing, (2) $25 < W_{eA} < 70$ is Jet disintegration via the stretched sheet mechanism (membrane type ligaments) and (3) $70 < W_{eA} < 500$ is super pulsing and jet disintegration via 'Fibre type' ligament that peels-off the liquid gas interface [31]. Figure 8 illustrates these three regimes.

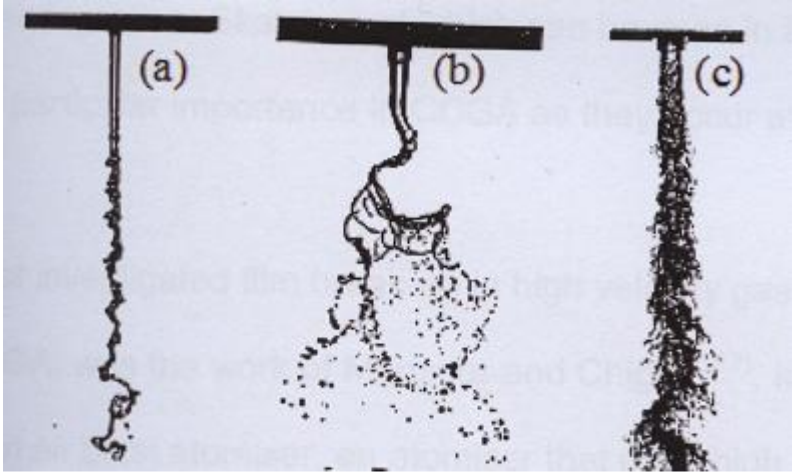

Figure 8. A sketch of the primary break- up for liquid column (a) Rayleigh break-up (b) Membrane break-up (c) Fiber type break-up [31].

2.1.1.3 Liquid film break-up

Film break-up occurs for nearly the whole of the CCGA process. Therefore, understanding this mechanism is particularly important while studying a CCGA. Although, this process is similar to the liquid column break-up, but instead of atomization of a liquid column to liquid droplets, it works throughout a pre-filming mechanism. In this mechanism, the liquid metal is forced to spread as a form of liquid thin film across the melt delivery nozzle tip by the direct impact of the high velocity gas jet. This mechanism makes an aerodynamic condition and causes the thin film to be atomized into the droplets [32]. Several parameters such as the physical properties of the gas, liquid and mechanical forces for interaction of gas with liquid affect the pre-filming break-up. Frazer et al. [32] reported a model of three steps for film break-up during gas atomization process at the air blast atomizer. These are (a) rim disintegration, (b) wave disintegration, and (c) perforated film break-up. Figure 9 shows a schematic view of this model. In addition, other researchers like Mansour and Chigier [33] observed this model. Also, Carvalho and Heitor (1998) [34] who had an experimental test with using of shadowgraph technique on film break-up of water with an air blast chamber reported the same mechanism. They described the relation between liquid film break-up and aerodynamic force of air stream close to the liquid nozzle edges, which can be affected by increasing the air velocity [34].

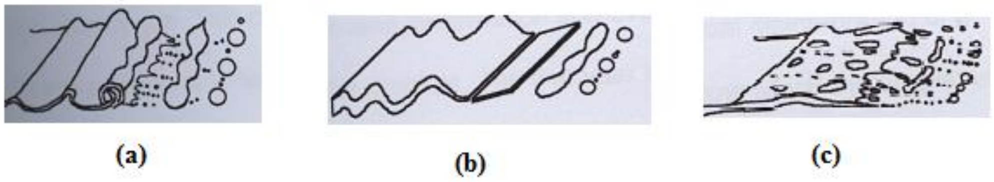

Figure 9. Sketches of liquid film break-up model (a) Rim disintegration (b) Wave disintegration (c) Perforated film break-up [33].

2.1.1.4 Liquid ligament break-up

The main mechanism for liquid ligament break-up is Rayleigh mode, which was proposed by Frazer et al. [32]. The liquid film break-up is followed by further disintegration in the form of liquid ligaments break-up; so, the thickness of ligaments can be a factor to determine the final droplets size. They reported some experimental results about the relation between mean particle droplet diameter and the melt film thickness during the CCGA process. They also observed a wide range of droplet sizes, which achieved in this mechanism and they conclude that more control on this mode must be applied.

2.1.2 Secondary break-up

Right after the primary break-up, the secondary break-up may occur. At this stage, the large droplets disintegrate into the smaller ones under the direct impact of the high velocity gas jet. The importance of this mechanism attracts much attention of some researchers such as Giffen &Muraszew (1953) [35] and Hinze (1955) [36]. The secondary break-up acts a crucial role on final particles size distribution especially at two-phase flow atomization similar to the CCGA. The studies by Hsiang and Faeth (1992) [37] revealed some similarities between this mechanism and liquid column break-up. They suggested three different stages for droplet disintegration based on the Weber number.

The Bag break-up starts at Weber number between 13 and 35. At this condition, the drop deflects to the thin disk and is then blown into open thick bubbles on their edges followed by centre thin disk deformation into the thin balloon. Further stretching of the thin balloon edges leads to perforation of the balloon and big droplets disintegrate into the small ones. The pulsed shadowgraph of this regime is depicted in figure 10 [37]. At Weber numbers between 35 to 80, the multimode break-up may happens. This type of break-up is a combination of two sub-divided regimes: bag-plume and plume-shear regime. The transition between bags to shear break-up makes a complex break-up process. Ranger & Nicholls (1969)

[38] and Dai et al. [39] had some pulsed shadowgraph studies on this type of liquid break-up. At 35 < *We* < 40, the dominant mechanism is the bag break-up and at 40 < *We* < 80, the dominant regime is the plume-shear regime [39]. At shear regime, the periphery disk is deflected downstream rather than the centre.

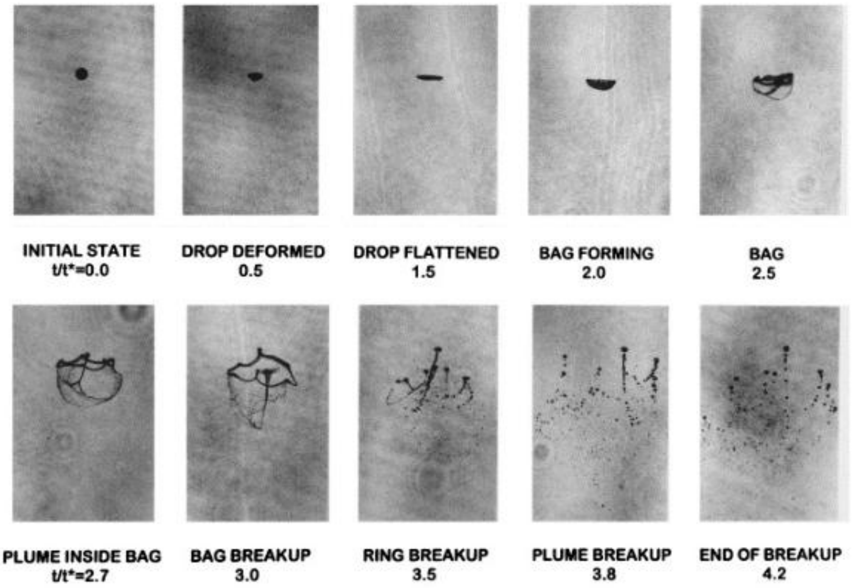

Figure 10. The pulsed shadowgraph of the bag break-up mechanism at Weber number of 20 and at different time sequence [37].

2.2 Close-Coupled Gas Atomization (CCGA)

The first investigation on the CCGA process was published by Thompson around 1948 [40]. It was followed by Massachusetts Institute of Technology (MIT), and leaded to the introduction a new Ultrasonic Gas Atomizer (USGA). In this technique, the ultrasonic waves are produced by resonance cavities at the gas die system, which help to disintegrate the melt stream. Further investigation by different research institutes such as Ames Laboratory, introduced the CCGA process with new improvements on both technique and process controlling. These series of improvements were more applied on the melt delivery nozzle and gas die design, along with gas flow investigation around melt delivery nozzle.

2.2.1 Just gas flow field investigation

One of the main important investigations on the gas atomization process is visualizing the gas flow pattern around the melt nozzle tip and studying its impact on the atomization efficiency. This investigation leads to more control over the atomization process. The gas flow visualization can usually be done by the several complementary methods such as optical visualizing methods of the Schlieren technique.

The Schlieren method uses special lenses or mirrors around the atomization gas chamber for visualizing the air density variation caused by the high velocity gas jet. The basic aspects of this technique are discussed in more details at chapter 3. The schematic view of the gas flow field , shock waves and gas boundary layers around the melt delivery nozzle for the CCGA process are shown on figure 11 [41].

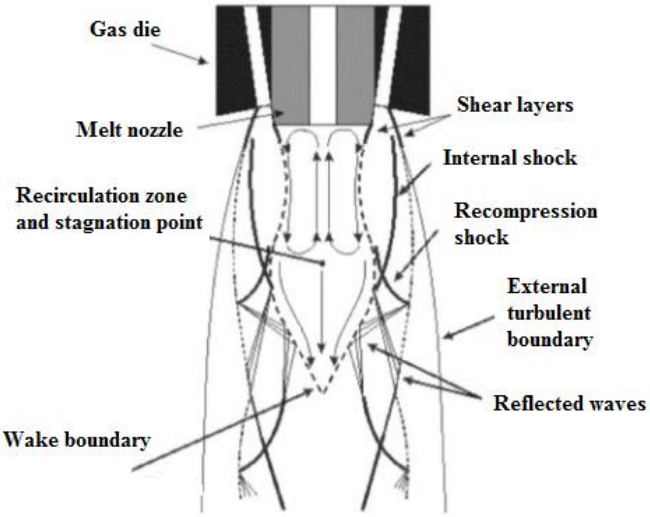

Figure 11. The schematic view of the gas flow field and its details around the melt delivery nozzle tip [41].

The gas flow pattern around the melt delivery nozzle plays an important role during gas atomization process and may affect the particle size distribution and atomization efficiency [41, 42, 43, 44]. Studying the gas flow behaviour around the melt delivery nozzle is divided into two important parts of : close field and far field areas. The close field area is an area about 3 to 4D (D is the melt nozzle diameter) downstream from the melt nozzle tip and beyond this distance is referred to the far field area [42]. These two areas are the most important zones of primary and secondary melt break-up in the gas atomization. The Schlieren studies of the gas flow field in the close field area have shown that the liquid disintegration mechanism is not just a simple shearing mechanism [42]. One of the gas flow field areas in close field area is the recirculation zone [42]. This area is shown in figure 12.

The melt stream spreads to the recirculation zone through the melt delivery nozzle and forces itself upward into a thin film around the melt nozzle tip [43]. However, due to the chaotic interaction between gas and melt around the melt nozzle tip, this phenomenon has not been very well understood. Thus, some hypotheses have been proposed by different researchers on liquid break-up at gas atomization [43, 44, 45].

The main well-known reason of recirculation zone creation proposed in literatures is aspiration pressure. The aspiration pressure is the melt nozzle orifice pressure or a time/average mass balance of the gas entering and exiting the control volume, and highly depends on ambient pressure of gas atomization pressure [46, 47]. The melt nozzle tip edges turn the high-speed gas jet flow into itself, compress it, and make some oblique shocks around the melt nozzle tip. In addition, some recompression shocks with an internal sonic boundary region known as ‘wake boundary’ occur due to the gas flow deceleration to the subsonic speeds in this region [48]. These shock waves are shown in figure 13. The recirculation zone is located inside the wake boundary where the primary break-up occurs. The simple sketch of the wake boundary region is depicted in figure 12.

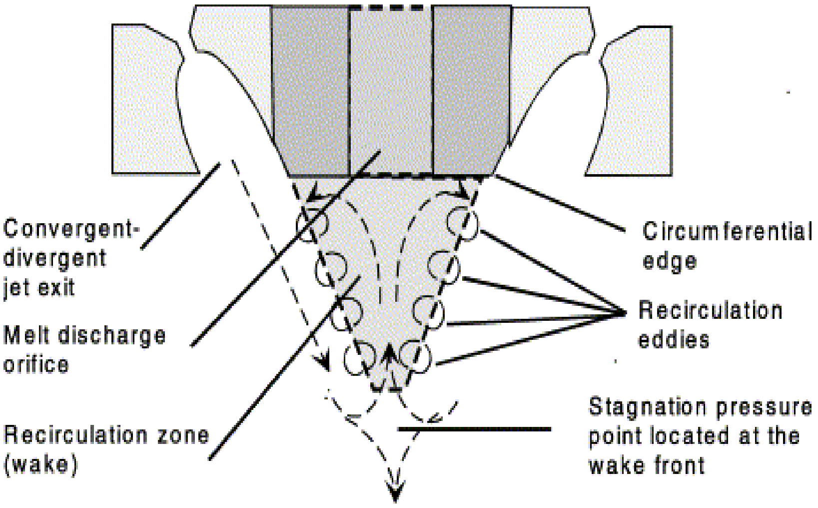

Figure 12. The wake boundary and recirculation zone at front of the melt delivery nozzle tip [47].

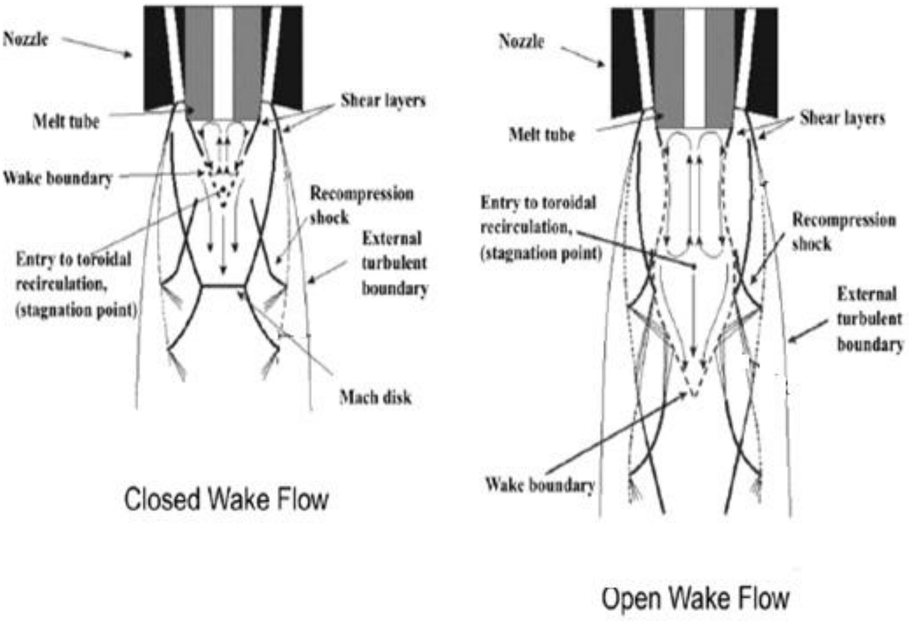

Closed Wake Flow

Open Wake Flow

Figure 13. The schematic view of gas only flow of closed and open-wake condition [48].

The gas wake region can take two forms of open and closed-wake condition. Figure 13 shows a sketch of these two wake configurations in a gas-only flow study. The closed-wake condition occurs at the high atomization gas pressures (normally at more than 4.5 MPa) when the internal shocks cross at front of the melt nozzle tip and forms the Mach disk [47]. Conversely, at the low atomization gas pressure, no Mach disk occurs at front of the melt tip and no internal shocks cross in the wake region. This condition is known as open-wake condition [47, 48]. Moreover, in both f these conditions, there is a stagnation point (Figure 12) with zero gas velocity and high gas pressure, which located at the far end of the wake region, at front of the recirculation zone. As the position of stagnation point moves away from the nozzle tip, the amount of the gas entering the recirculation zone becomes larger. Srivastava and Ojha [49] showed that either the gas can enter the wake region in two ways of vortices and turbulent eddies or recirculation eddies around the sonic boundary of the recirculation zone.

Some hypotheses have been proposed about melt disintegration in the recirculation zone. Settles and Mates [46] have reported their investigations on primary break-up by visualizing some Schlieren images. An example of primary break-up tested by Settles for visualizing this phenomenon is the formation of a molten tin sheet at front of the melt delivery nozzle tip. The melt sheet forms as the radial gas pressure gradient forces the liquid sheet out to the nozzle edges and then into the supersonic cross-flow [46]. Consequently, they proposed that the metal liquid is stretched-out into a thin sheet and atomized vigorously into the fine droplets (Figure14). They found that the thickness of the liquid film at this stage could determine the particles size.

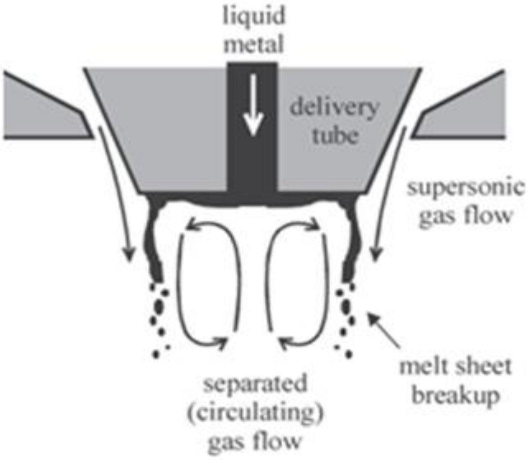

Figure 14. The primary break-up of the liquid tin sheet proposed by Settles [46].

Many parameters may influence the recirculation zone such as atomization gas pressure, melt nozzle tip internal design, and melt nozzle protrusion length and gas die geometry. Ting et al. [48] proposed a model on liquid formation at the front of the melt nozzle tip at open and closed-wake condition. They explained at atomization gas pressure lower than 4.95 MPa, the melt spreads-up to the wake region by a shallow aspiration pressure (Figure 15). At the open-wake condition, as the wake region becomes larger, more gas enters this region, and aspiration pressure increases significantly. This may cause some melt disruption and melt retardation. When melt flow rate decreases at the melt delivery nozzle tip, the wake shape returns to the previous form. This phenomenon reoccurs momentarily at frequencies, which are typically 10-50 HZ during gas atomization. Because of such gas and melt behaviour, the recirculation zone can control the gas atomization process, especially primary break-up [47, 48].

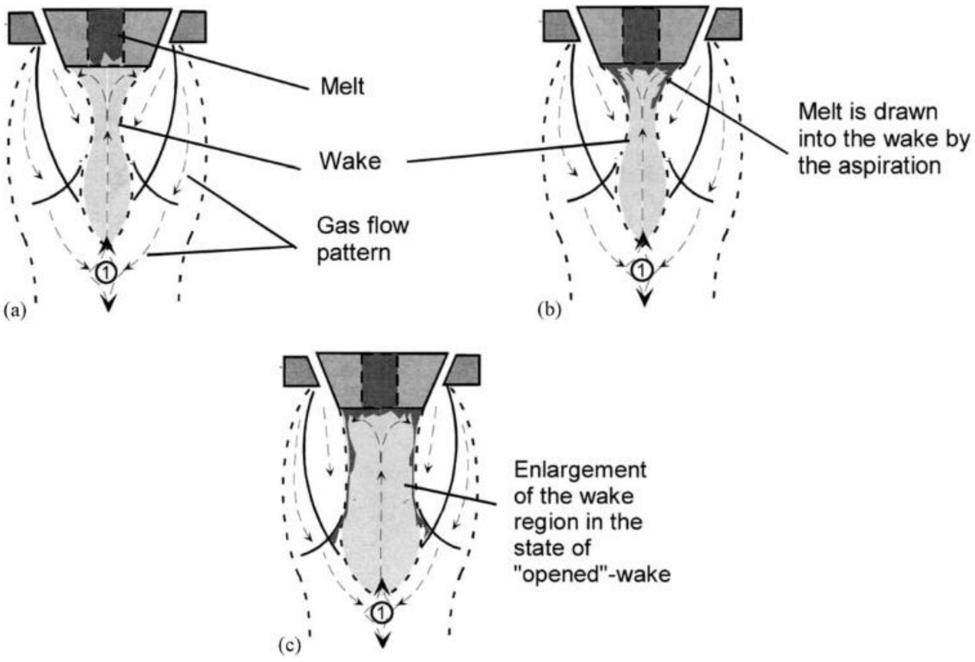

Figure 15. The liquid break-up model at the low atomization gas pressure and open-wake condition proposed by Ting [48].

The same process can happen generally at a high atomization gas pressure (higher than 4.5 MPa) and closed-wake condition. With the presence of the melt flow in the gas wake zone, the closed-wake changes to the open-wake condition and the Mach disk disappears and this causes the high-pressure gas at the stagnation pressure rapidly enters to the open-wake condition [48]. This situation can be seen in figure 16c. The sudden entrance of the high-pressure gas into the open-wake condition may temporarily disrupt the melt flow into the gas wake region. With the absence of physical melt forces; again the force of gas jet closes the gas wake region and re-establishes the closed-wake condition (Figure 16e). The gas wake condition between open to closed-wake is known as pulsation phenomena, which can be seen as a flickering during the CCGA process [48].

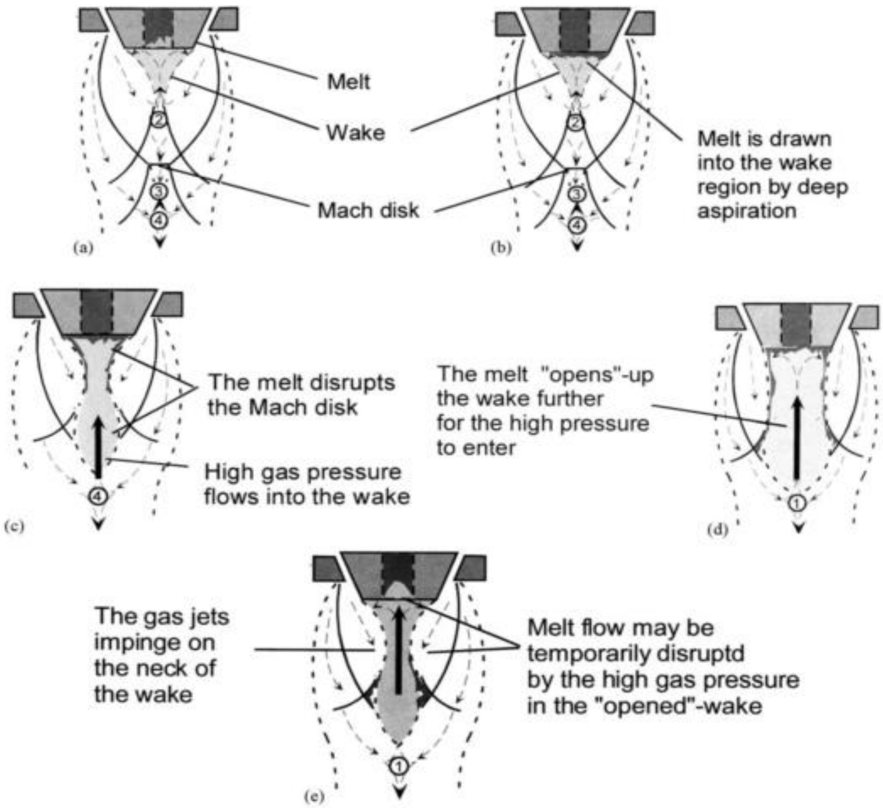

Figure 16. Break-up phenomena at high gas pressure and Mach disk creation at close wake condition around melt nozzle tip [48**].**

2.2.2 Wake Closure Pressure (WCP)

As discussed above, the open and closed-wake condition may be formed at the low and high atomization gas pressures, respectively. The atomization gas pressure above of which the wake region at the front of melt delivery nozzle is in closed-wake condition, and below of which, the wake is on open-wake condition is called Wake Closure Pressure (WCP). The WCP depends on some parameters such as gas inlet pressure, gas jet die apex angle and external or internal geometry of the melt delivery nozzle. Wake closure has been an area of interest of many researchers. This is because they believed that atomizing at the pressure just above the WCP might be beneficial for producing better powders [50, 51].

Ting et al. [50] have investigated the impact of the WCP on the particle size of Ni-base alloy. The particles size of this alloy atomized just above the WCP was 42% finer than the particles obtained at the open-wake condition. In addition, they reported operating the system at WCP, decreases the melt flow rate from the tundish to the melt delivery nozzle [51, 52]. On the other hand, Mates and Settles [46] who proposed the wake closure could not affect the atomization process disputed their results, and proposed the closed-wake condition is not preserved at the CCGA process [46].

2.2.3 CCGA melt nozzle and gas die design

As mentioned in the introduction section, in the CCGA process, the molten metal stream comes into contact with the high pressure gas jet via melt delivery nozzle. Thus, the design and improvement of the melt delivery nozzle and the gas die system may increase process efficiency and control the final product size distribution. This part discusses briefly the gas die and melts nozzle design improvements which are the promise for the improvement of this process.

2.2.3.1 Gas die system design

During evolution of CCGA process, some researchers have focused on increasing the efficiency of the CCGA process [51, 52, 53]. Following the increase in demand for the high quality fine spherical particles, many developments have taken place for improving the gas atomization system. One of these developments involves the gas delivery system or gas die in the atomization process. The profile design of the gas die system such as gas jet exit area and gas jet apex angle, whether annular slit or discrete jet type are the key factors for controlling the gas to metal interaction at CCGA. For conventional CCGA process, an annular slit confined feed gas jet (AS-CF) was favoured (Figure 17). This type of gas die set-up consists of a circular opening fed gas die around the geometrical centre of the melt delivery nozzle where the outer surface of the melt nozzle wall acts as inner gas die surface.

However, this method was not efficient enough due to non-uniformity of gas rate and high gas-consumption [53, 54]. Due to this type of gas die configuration at the gas outlet, the gas flow rate is larger than discrete jet gas die system. Therefore, this kind of gas die typically operates at the gas pressures of 3 to 4 MPa [53, 54]. In addition, use of annular slit gas die set-up has some difficulties in the gas set-up alignment with respect to the focal point of gas flow, asymmetric flow field, and melt delivery nozzle axis. Due to the above-mentioned problems and low productivity rate of this method, the new generation of gas die system was developed [54].

Creation of gas die system with discrete jet of confined feed gas jet known as (DJ-CF) was one of the most effective methods for producing finer and more spherical powders compared to annular slit gas die system. As noted above, on annular slit gas die system, the melt delivery nozzle is not separated from the gas die, but in DJ-CF, the gas die and melt delivery nozzle are totally separated from each other. One of the advantages of discrete jet gas die system is low gas consumption compared to that of annular slit gas die while operating at the same inlet pressure. This is related to the low exit jet area of this type of gas die design. Therefore, it is possible to elevate the gas inlet pressure on discrete gas die system, which may lead to particle size refinement [54]. Due to the special design of the discrete jet gas die system, many studies have been applied to improve the efficiency of this method, so this type of gas die system, is still not widely applied by large commercial atomizers [54].

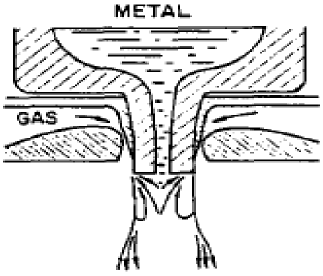

Figure 17. A sketch of an annular slit gas die system and the melt nozzle (AS-CF) [53].

There are two best-known discrete jet gas die designs in the literature: the Ultrasonic Gas Atomiser known as USGA and the High Pressure Gas Atomizer (HPGA) which designed by Ames Laboratory [54].

O.F. Nilsson patented the earliest model of the USGA gas die system in 1961 [55]. Further research by Ting et al. [54] revealed that using this kind of gas die decreases particle size distribution by increasing the gas pressure. In this type of the gas die, 18 cylindrical gas jets with an apex angle of 45 degrees are arranged around the melt delivery nozzle (Figure 18). This gas die system has specially designed cavities that the gas passing through them produces ultrasonic high frequency sound waves, which have enough kinetic energy for disintegrating the melt stream.

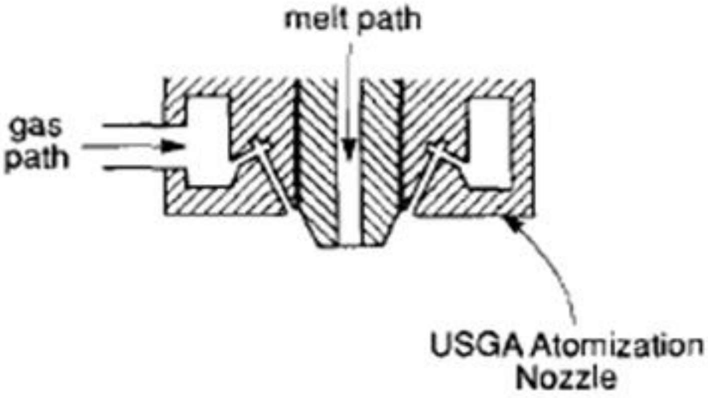

Figure 18. A schematic of USGA gas jet nozzle and the melt delivery nozzle with manifold design [54].

Creating ultrasonic sound waves is a complex mechanism, which is not still fully understood. However, there is a model explains that the ultrasonic gas waves may occur due to the gas boundary layers expansion within the gas jet [54, 55].

The other version of the DJ-CA gas die was the HPGA die system developed by Ting and Anderson in Ames laboratory [54]. This type of gas die has twenty cylindrical gas jets with a 45-degree apex angle around the melt delivery nozzle. The main purpose of designing HPGA was producing high-pressure gas jet without increasing gas consumption. Therefore, it was an effective technique to solve the main problem of annular slit gas system with high gas consumption [54]. Figure 19 shows the HPGA gas die system set-up designed by Ames laboratory.

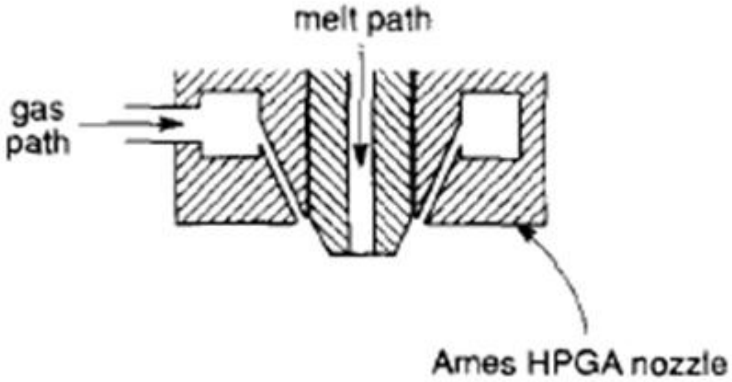

Figure 19. A schematic view of Ames nozzle jet and the melt delivery nozzle [54].

In order to enhance the efficiency of this type of gas die, Ames laboratory studied on the HPGA gas die by testing different physical and mathematical models [54]. One of the significant changes in the design of this gas jet profile was the replacement of the cylindrical gas die profile with a Convergent-Divergent (C-D) design [54].

To understand the new concept of HPGA gas die system with new C-D jet profile, it is required to be familiar with the physical features of the C-D die design.

The primary HPGA gas die had a cylindrical choked gas jet profile that is limited to the subsonic gas jet. The aim of replacing the cylindrical choked profile with the C-D type was to produce a super-sonic gas flow. In the adiabatic condition, immediately upon the gas exits the choked die; the gas will expand rapidly outside the jet, but in an uncontrolled manner the gas accelerates to Mach 1. The exiting gas is not collimated and as a consequence, the kinetic energy of the gas for melt stream break-up decreases [54]. Figure 20 shows the schematic view of a C-D or de Laval die profile. The jet engines of rockets and fighter jets have the same profile of figure 20. The gas flows from left side, which is the convergent chamber of the C-D die to the throat area. In this section, the gas becomes concentrated and pressurized up to its maximum level. Then the compressed gas flows with collimated shape beyond the throat in the divergent region and accelerates to the supersonic velocity after the exit area (Figure 20). The ratio of throat to the exit area controls the ideal operation pressure of the gas die on the isentropic flow condition. Therefore, each C-D gas die is designed for one specific working pressure and this kind of gas die just produces a particular Mach number [53, 54].

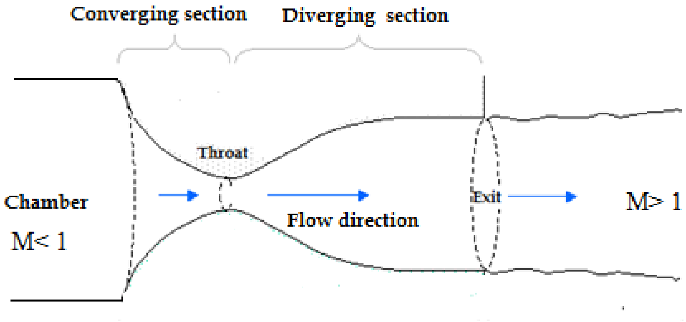

Figure 20. A schematic view of C-D gas jet profile.

The relation between Mach number and throat area is defined by the following equation for isentropic conditions:

$$\frac{\mathrm{A}}{\mathrm{A}_t} = \left(\frac{1+\Upsilon}{\Upsilon}\right) \quad -\mathrm{k}\,\frac{\left(1+ \quad \left(\frac{\Upsilon-1}{2}\right) \quad \mathrm{M}^2 \quad \right)^{\mathrm{k}}}{\mathrm{M}} \qquad (2)$$

Where k is defined as: $\mathrm{k} = \frac{\Upsilon+1}{2(\Upsilon-1)}$

In Eq. (2), $\frac{\mathrm{A}}{\mathrm{A}_\mathrm{t}}$ is the ratio of the exit area to throat area , Υ is the ratio of specific heat capacities, and M is Mach number. The outlet Mach number also determines the design criterion of the ratio of the inlet pressure (p) and the ambient pressure (p_0):

$$\frac{p}{p_0} = \left(1 + \left(\frac{\Upsilon-1}{2}\right) M^2 \right)^{-\frac{\Upsilon}{\Upsilon-1}} \qquad (3)$$

The Mach number is defined as: $$M= \frac{u}{u_{sound}} \qquad (4)$$

Where u is is the velocity of the source relative to the medium and u_{sound} is speed of sound. The C-D gas dies are designed to collimate the gas jet and produce a supersonic gas jet. The collimated gas causes the gas to reach the ambient pressure, which is an ideal expansion; this means that no shock waves may be formed in this situation [56]. Lack of shock waves during gas atomization process is desirable due to more energy available for breaking-up the melt stream. Operating the C-D die below the designed ambient pressure results in overexpansion flow, and forms subsonic shock waves and boundary layers at the exit area of the die (Figure 21). Conversely, running the C-D gas die above the ambient pressure leads to underexpansion behavior [54]. In this case, the gas is not fully expanded by the time it reaches the nozzle exit area, while the gas velocity is supersonic (Figure 22) [54, 56]. Furthermore, such difference between gas jet pressure and gas chamber pressure also results in some shock waves at the die exit area and causes expanded and contracted crossing shock waves inside the boundary layers in the front of die exit area generally known as Prandtl-Meyer waves [54, 58]. An underexpanded flow is more similar to the ideal gas operation, since the gas collimates a long distance downstream of the die exit area [58].

Measuring the real ideal operation pressure for this kind of gas die may provide values notably different from theoretical results due to the machining tolerance [57, 58]. For instance, some series of the HPGA gas dies designed by Ames laboratory [54], known as HPGA-II generation, was developed to operate at an ideal gas pressure of 3.6 MPa, but this gas die was operated at ideal operating pressure of 2.4 MPa at working condition due to machining tolerance.

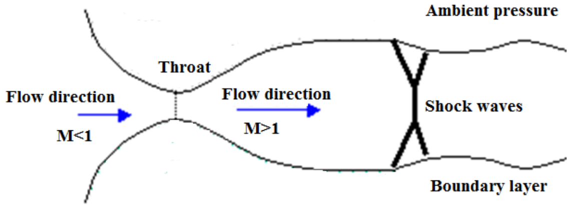

Figure 21. A diagram of a single gas jet for the overexpanded flow field.

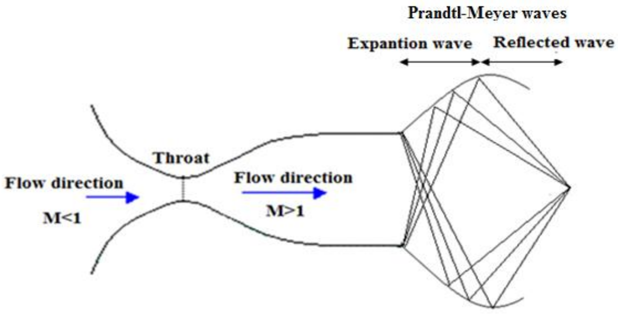

Figure 22. A diagram of a single gas jet for the underexpanded flow field.

Based on research results of the CCGA process, using the C-D profile die design may increase more control on both mean particle size and standard deviation of the final product [56, 57]. The first report of using the C-D die for CCGA process was published by Unal [52]. The new improvements on the C-D die were followed by Ames laboratory [54]. The first series of HPGA die was designed by Ames Laboratory and known as HPGA-I. This type of the gas die produced a subsonic gas jet, but in order to reach supersonic gas jet velocity, the second series of high pressure gas die was designed. This type of gas die is known as HPGA-II and was improved version of HPGA-I [54].

The HPGA-II was an attempt to enhance the efficiency and performance of the CCGA discrete jet gas system. The apex angles of both of these gas dies were 45 degree [54]. The research group of Ames laboratory deployed many studies using Schlieren technique; high-speed imaging, powder size data, and mathematical modelling to develop the HPGA gas die performance [54]. These studies more focused on the gas jet angles and gas die geometry to enhance the gas efficiency and process control.

The third generation of the C-D gas die design was HPGA–III with an apex angle of 22.5 degrees and 18 discrete C-D jets holes. This type of gas die had the ability to produce supersonic gas jet slightly above Mach 3 and operate at the gas pressure above of 7 MPa [54]. In addition, the geometry of each gas jet profile was redesigned and improved to modify the boundary layers formation at the jet exit area in order to alleviate the problems of HPGA-II.

Comparison of powders production of two HPGA designs under the same operating condition showed that the average particles diameter of d_{50} was 35µm for HPGA–III and 41 µm for HPGA–II [54]. Furthermore, this result showed that decreasing the apex angle of the gas jet with the melt delivery nozzle on HPGA-III could increase the efficiency of the new HPGA-III generation over the previous HPGA-II

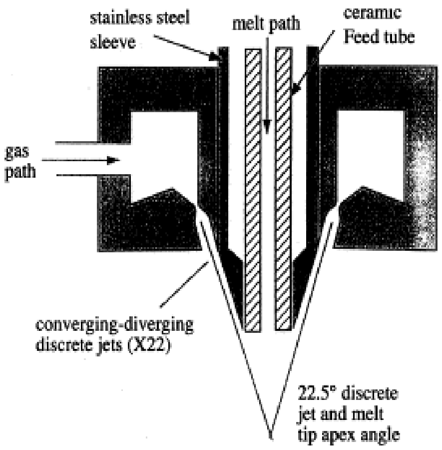

Figure 23. A scheme view of HPGA-III gas jet nozzle [54].

2.2.3.2 Design of melt delivery nozzle

Similar to the gas die design, the melt delivery nozzle geometry and profile plays a crucial role in the CCGA process [53]. The size and the shape of the melt delivery nozzle affect the gas flow field around the nozzle tip and primary atomization stage. On the other hand, correct design and selection of the melt delivery nozzle can improve the atomization performance [53, 54]. In addition, in some cases the melt nozzle design can be an essential factor for failure or good running of stable atomizer system. The optical visualising technique like Schlieren technique revealed that any changes on internal or external design of the melt nozzle affect the gas flow field and influence the CCGA gas flow pattern parameters such as gas recirculation zone or gas aspiration pressure [53, 54].

2.2.3.2.1 Melt nozzle external length design

At CCGA process, the protrusion nozzle tip length of the melt nozzle controls some gas atomization parameters which are important to operate a stable atomization [53, 54]. Moreover, the incorrect design of the nozzle tip length causes some atomization problems such as melt freeze-off inside the melt nozzle orifice [53]. This problem occurs when the high-pressure gas jet cools down the melt stream rapidly inside the nozzle orifice. In addition, too much gas and too little melt at the melt nozzle results in the melt being solidified as a plug in the nozzle orifice, preventing further melt flow, and cloging the melt delivery nozzle [53]. Under such condition, the melt nozzle design can lessen the freeze-off problem, if the gas jet die is designed for sub-ambient (suction) pressure. Moreover, sub-ambient pressure accelerates the gas jet stream around melt nozzle tip and provides stable gas operation [53, 54, 57].

For better understanding of the effect of the nozzle tip length design on the performance of gas atomization, Anderson et al. [53] performed some series of investigations with Schlieren technique. In all of their studies, the melt delivery nozzles were made of identical materials and only the shape and length of nozzles varied. The schematic sketch of these four melt delivery nozzles is depicted in figure 24.

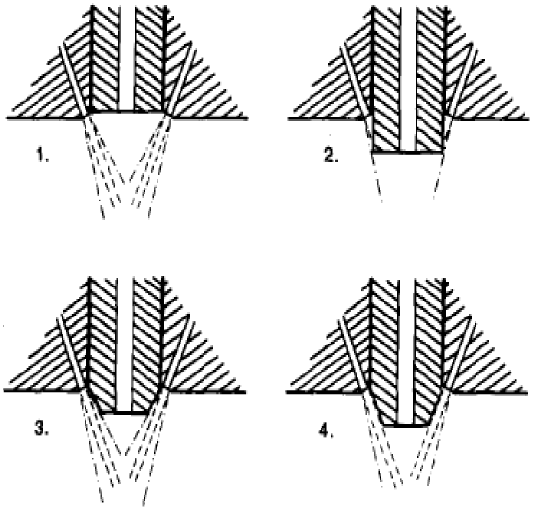

Figure 24. Different nozzle tip designs, 1. Retracted tip, 2. Extended square nozzle tip, 3. Tapered extended tip with 63-degree apex angle, 4. Tapered extended tip with 45-degree apex angle [53].

They found that the nozzle design 1 provided a logical design to control the gas atomization process and compared to alternative geometries; this type of melt delivery nozzle involved no direct contact between the melt nozzle tip and the gas die [53]. In the 2nd melt nozzle design, the nozzle tip extended to a square-edged and in this case, the melt stream was closer to the gas jet focal point. In this design, the extended melt nozzle tip essentially diverts the gas from projected cores. Consequently, this type of nozzle provides a strong interaction between the melt tip and the gas die. In nozzle design 3 and 4, a taper melt delivery nozzle tip has been used. The main cause for designing the melt nozzle 4 was to align the melt nozzle taper with the gas jet angle for better flow expansion at the high atomization gas pressure [53].

According to these experimental results, Anderson and his colleagues reported that the melt nozzle tip profile has a significant effect on the gas flow pattern in front of nozzle tip. In addition, for optimum performance of the gas atomization, it is required to carefully align the external wall of the melt delivery nozzle with the gas exit jet array of the gas die.

2.2.3.2.2 Internal melt nozzle design

The internal design of the melt nozzle is another factor that controls the melt stream disruption during primary gas atomization of CCGA. There are different internal shapes and profiles for different applications at CCGA process [53]. The most common shape is the flat tip end melt nozzle [53, 54]. This shape is popular among commercial atomizers [53]. However, during recent years the use of melt nozzle similar to that seen in figure 25 has been popular among commercial atomizers [53, 54]. Miller [56] first patented this type of melt delivery nozzle, and then Anderson et al. [53] had made some studies on this type of melt nozzle with expanded tip into concave profile. The concave shape deflects the gas recirculation zone in front of the melt nozzle tip and develops more interaction between the gas and melt [53].

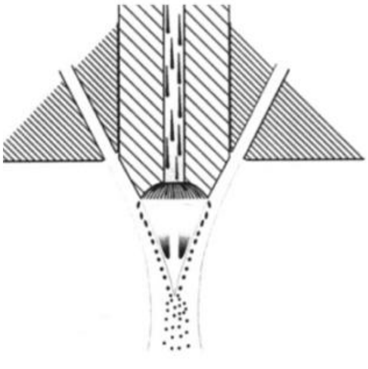

Figure 25. The melt delivery nozzle design with concave tip profile [53].

Anderson et al. [53] did more investigations on melt nozzle internal design. They found that to decrease the particles size, it is required to disintegrate the melt stream at the primary zone where the gas jet has the highest kinetic energy and the melt stream is exposed to a strong temperature gradient at the recirculation zone. If the melt stream moves further downstream beyond the primary atomization zone, the gas energy decreases and coarser particles with border particle size distribution will achieve [53]. Therefore, they decided to design a melt nozzle with expanded melt orifice diameter similar to what is shown in figure 26.

Simple changes on the melt nozzle central bore diameter cause more melt film spreads across the base of melt tip orifice, which is more exposed to the high velocity gas at the primary atomization zone. Further studies on the melt nozzle internal design have been performed to maximize the initial liquid disintegration and increase the melt flow stability [59].

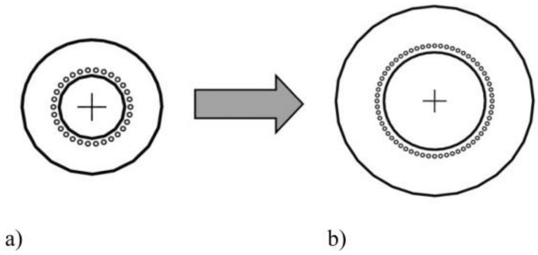

Figure 26. The bottom view of two different melt delivery nozzles with discrete jet gas die system, a: a melt nozzle with 10.4 mm central bore diameter, b: a melt nozzle with 19.5 mm central bore diameter [53].

To improve the efficiency and stability of the melt stream flow, some changes were applied on the melt nozzle internal tip profile to transform the chaotic melt stream flow to the stable condition [53]. This was done by providing slots or channels inside the internal face of concave melt nozzle tip, which guides more melt flow from centre to the edges of the nozzle tip to impose high velocity gas jet [53]. The other version of this type of melt nozzle was known as ‘Bessel horn’ or ‘Trumpet bell’ shape (Figure 27), which had more extended slots. Thus, use of this melt nozzle increases the atomization efficiency by providing all energetic gas to disintegrate the melt ligaments. The design and alignment of the slots with the individual discrete jets are another challenge for researcher to increase the powders uniformity and atomization efficiency [53].

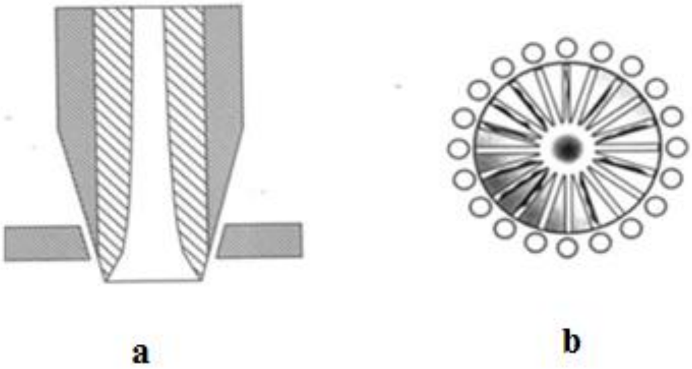

Figure 27. A schematic view of a: Trumpet bell melt delivery nozzle b: bottom view of slotted melt delivery nozzle and discrete jet gas die system [53].

McCarthy et al. [57, 58] also used optical methods such as high-speed imaging, PIV and PLI techniques with an analogue water atomizer, which was a replicate of a real closed coupled gas atomizer. They investigated the complex melt plume movement by changing the internal and external protrusion length of different melt delivery nozzles. Their results showed that changing the internal and external nozzle profile had a substantial impact on the melt plume movement behaviour and proposed a new model to explain this behaviour relating it to different nozzle internal profiles [57, 58].

2.2.4 Visual technique for investigation of CCGA process

Using a combination of the optical visualisation technique and high-speed cinematography are natural progressions for investigating the single-phase flow of just- gas flow at CCGA [61]. There are some other optical methods like Particle Image Velocimetry (PIV) and Pulse Laser Imaging (PLI) techniques, which are more useful for two-phase flow investigation when the liquid/gas interaction is more focused to investigate at CCGA. The PIV uses tracking method of seeding particles movement as tracer within the flow by pair of consecutive image frames. In this method, the motion of particles inside the flow is used to calculate the velocity and direction of the flow [58]. In addition, the PLI is an imaging technique, which operates by producing a double pulse laser beam can be used to create two consecutive images split by a very short time delay. Due to a short exposure time (around 15 μs) between each laser pulse, and the use of a high resolution imaging technique, the liquid/gas interaction is captured at a very short period [58].

Ünal did the early study of the high speed imaging technique with use of high exposure flash for investigation of aluminium atomization at 1980 [60]. Then in 1989, he combined an optical visualizing Schlieren technique and high speed imaging system to study the flow separation and back stream melt problem at CCGA. Figure 28 shows the back stream problem of solidified nickel-aluminium around melt delivery nozzle [58].

Combination of the optical Schlieren imaging system with the high speed imaging technique of Ünal [60] showed that the back-stream flow problem occurred as the result of flow separation of gas from external wall of melt nozzle incurred by negative pressure gradient associated with shockwaves [60]. Mates and Settles [61, 62] extended the early studies of Ünal with using Schlieren and CCD camera capable of imaging 1/30th of a second and strobe flash light source with duration of 1.2μs. They used Schlieren technique to study the single-phase flow of different gas die system set-up and combination of Schlieren and high-speed imaging technique for visualizing the break-up of tin melt in the two-phase flow. The amount of molten metal variation and break-up can be seen in each frame in figure 29 [61]. They stated that a different gas die system affects the gas flow pattern around melt delivery nozzle at the single-phase study. In addition, they showed the chaotic nature of gas and melt interaction in the CCGA process at the two-phase flow study [61].

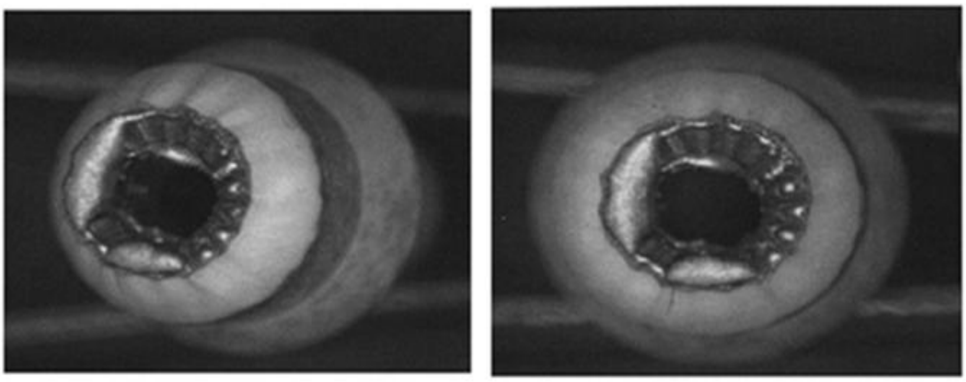

Figure 28. A ceramic melt delivery nozzle tip incurred by back-streaming phenomena during gas atomization of Ni-Al [58].

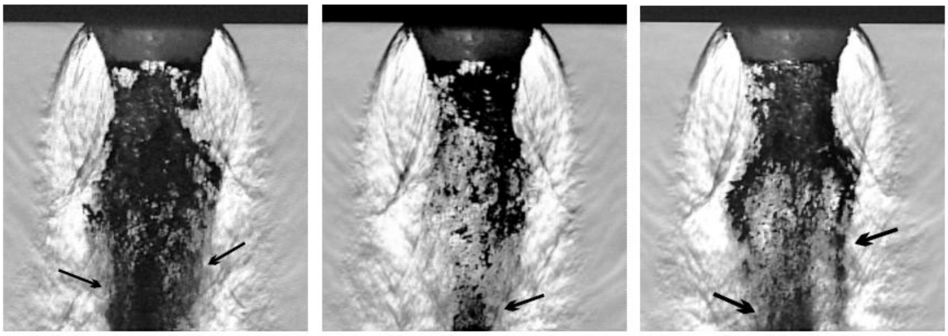

Figure 29. Random still images of break-up phenomena at the gas atomization of Tin with HPGA gas die system. (Arrows show the fine droplets) [61].

The history using of Schlieren technique returns to 17th century by Robert Hooker in 1665 [62]. Then, different researchers developed this technique over the past centuries. Early in the 20th century, Albert Töpler developed this technique in 1906 [62]. Also, different physicist like Robert Wood [62] (1868-

1955) used this method for visualising the shock wave formation in the supersonic air tunnel during the World War Two in Germany. This method became a key tool in fluid dynamic labs for designing the military aircraft and missiles.

The theory of Schlieren technique is based on refractive index gradients in transparent media, which cause light rays to bend (refract) in the direction of increasing refractive index. This is due to light velocity reduction in a higher-refractive-index material. The basic Schlieren system set-up is as simple as possible through using two convex lenses or geometric optics and a point of light source. There are different ways for optically arranging the appearance of the Schlieren in an image of the field of interest. In Töpler Schlieren method, there is a source of light, two convex lenses with specific focal length and a knife-edge commonly a razor blade blocking the straight light, but passing the distorted light to the screen or camera lens, which is needed for capturing the Schlieren images. The source of light is different and depends on the test or objects to be viewed can be LASER, tungsten-halogen or LED light. A schematic Töpler Schlieren arrangement for the gas atomization process is shown in figure 30. However, the light beams may be refracted when encountering an area with different temperature and density within the same material. A variation in the index of light reflection in air causes different light distortion around the object [62]. The relation between density gradient and refractive index variations is given by the Gladstone-Dale equation:

$$G\ (\lambda) = \frac{\mathrm{n}-1}{\rho_A} \qquad (6)$$

Where G (λ) is defined as :

$$G\ (\lambda) = 2.2244 \times 10^{-4} \times \left[1 + \left(\frac{6.7132\mathrm{x}\ 10^{-8}}{\lambda}\right)^{2}\right] \qquad (7)$$

Where λ is the light wavelength (m), n is the light reflective index and G (λ) is the Gladstone-Dale number [62].

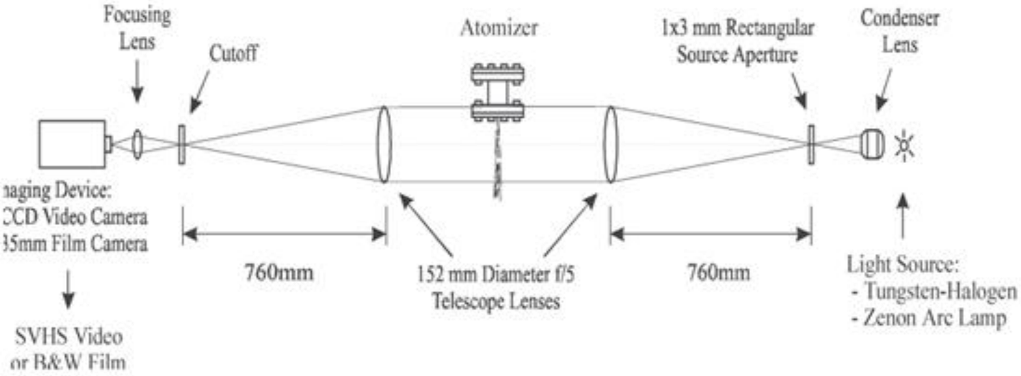

Figure 30. Schematic arrangement of Töpler Schlieren equipment for the gas atomization process [61].

The production of Schlieren image requires using perfectly parallel beam of the light [56]. By positioning the light source at the focal point of a large convex lens, the diverging rays striking the lens and refracted to form wide parallel beams. These beams pass through the air and as incident to the second converging lens. Some of the light becomes remain parallel as they pass through the air between the spaces of these two lenses and bring to the focus at the focal point of the second lens [62]. These beams continue and form an inverted image on the screen. However, for making the Schlierem image on the screen, an obstacle or a knife-edge, which is commonly a razorblade must be placed at the focal point of the second lens, which blocks the straight lights coming from the second lens at the focal point and allow the refracted light to pass to the screen [62].

The same phenomena may occur with two parabolic mirrors with special arrangement known as Z-type arrangement (Figure 31) [61, 62]. Choosing the right Schlieren arrangement between Töpler and Z-type depends on different factors such as: set-up location and cost of mirrors, which generally mirrors are more expensive than lenses with the same diameter.

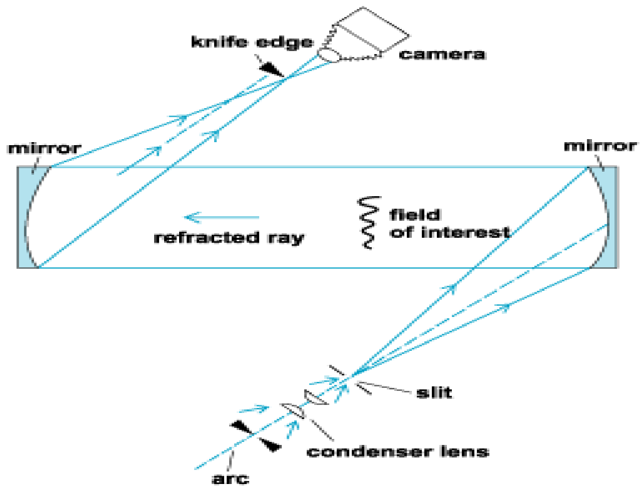

Figure 31. The Z- type mirror arrangement [60].

In the study of the gas flow behaviour in the gas atomization process, using both Schlieren techniques is one of the best ways to understand the gas flow field around the melt delivery nozzle. For instance, Settles et al. [62] used Töpler arrangement for studying the gas flow pattern with two gas dies or Ünal [60] used Z-type mirror arrangement for investigating the back-stream flow problem during CCGA.

2.2.5 Gas to metal ratio (GMR)

One of the important terms in the gas atomization process is gas-metal mass ratio (GMR or GM). This term is defined as "amount of gas used in amount of melt to be atomised [63, 64]. Wigg [65] did the first empirical studies on the gas atomization parameters on 1964. He proposed some relationships between the mass median diameter (d_{50}) and process parameters that collected from free-fall gas atomization [65]. The equation (4) shows the empirical Wigg's correlation.

$$d_{50} = 0.004\upsilon_L\ 0.5\ M^{0.1}\ \sigma^{0.2}\ \rho_A\ U^{-1}\ \sqrt{\left(1+\frac{M}{A}\right)} \qquad (8)$$

Where υ_L is the liquid kinematic viscosity (m^2 s^{-1}), M is the liquid mass flow rate (kg s^{-1}) and A is the air mass flow rate (kg s^{-1}). Moreover, Lubanska [66] has done more research about influence of different atomization parameters on particle size and modified the Wigg's correlation. Her studies were more focused on the free-fall gas atomization of Iron, copper and tin with an annular slit gas die set-up. She used sieving powders into the different meshes to obtain the powders size data [66]. She also proposed an empirical equation for the relation between the (d_{50}) and the GMR as follow:

$$\frac{d_{50}}{d} = b\sqrt{\left[\left(\frac{\upsilon_L}{\upsilon_g\ We}\right)\left(1+\frac{M}{A}\right)\right]} \qquad (9)$$

Where d is diameter of the nozzle (m), υ_g is kinematic viscosity of gas (m^2 s^{-1}), b is constant which depends on atomization situation and We is Weber number. This relation has been tested by other researchers and showed acceptable results for some gas atomization process [64]. In addition, the other format of the relation between GMR and mass median particle size, which reported by some researchers can be written in the general form of:

$$D = b/\sqrt{\frac{A}{M}} \qquad (10)$$

Where D is the mean particle diameter. Strauss and Miller [67] suggested an extra term of energy input to the system for improving the GMR. The ratio of power input of atomization gas to the output power leads to a new atomized powders surface area in relation to GMR as follows:

$$\frac{P_s}{P_m} = \frac{0.5\,Mu_g^2}{N_m S_m\,\sigma} = \frac{1}{6}\left(\frac{M}{A}\right)\left(\frac{u_g^2\,r\rho_A}{\sigma}\right) \qquad (11)$$

Where $\frac{P_s}{P_m}$ is the ratio of input and output power to the system for making the new powders surface area, u_g is the gas velocity (m s^{-1}), r is average powders radius (m).

2.3 Literature review on Computational Fluid Dynamics (CFD) at CCGA

Computational Fluid Dynamics (CFD) is one of the branches of fluid mechanics that uses numerical methods for solving the fluid governing equations. With using of CFD, it is possible to predict and simulate the gas and liquid interactions. Generally, CFD uses descretization methods for solving the fluid governing equations for specific geometry and boundary conditions. This method were developed and refined by many efforts and validations over the years [68, 69]. In 1973, a CFD group at Imperial College University reported an ambitious numerical program for predicting gas flow behaviour at low Reynolds number for simple shear flows, free and confined gas jet flow. These results were presented for two and three dimensional flow configurations [70]. In 1974, Launder and Spalding developed this model to consider high Reynolds number and turbulent flow [71]. Their efforts presented the new averaging method on fluid flow governing equations, which is commonly known today as the two-equation turbulent model. Furthermore, during 1977 to 1986, many people like Gosman, Khalil, Whitelaw and Spalding published articles on CFD methods [70]. CFD is now widely used in many applications for designing and developing different applications such as medical purposes, aviation and automobile industries, and more recently in the gas atomization process. CFD has become a fundamental tool for analysis of the gas flow fields around the melt delivery nozzle in the single-phase gas flow studies and to a limited extend of two-phase flow.

As mentioned in section 2-2, due to the multifactor and complicated interaction of gas and melt during the melt break-up in the gas atomization process, the study of two-phase flow with CFD techniques is very complicated. The early study of melt-gas interaction by Rayleigh (1878) [72], Bradley (1973) [73], and Markus et al. (2002) [74], showed many assumptions and simplifications applied to the analytical method. This method used to investigate the gas-metal interaction on the free-fall atomization; therefore, these results were difficult to fit with the real atomization process.

Due to the rapid development of computer hardware and software, more numerical methods were developed for simulating multi-fluid flow at atomization process. Zaleski (1999) [75], Thomas et al. (2004) [76], and Li et al. (2007) [77] have used numerical methods along with commercial CFD packages to investigate the ligament and droplet formation during gas atomization. Tong et al. (2008) [78] used direct numerical methods for predicting the melt-gas hydrodynamic interaction near the melt delivery nozzle at the beginning of CCGA process. This method solves the flow governing equation by numerical methods without including turbulence models [78]. However, the unsteady dynamic interaction of melt and gas in the real gas atomization process is very challenging for simulating this behaviour. Moreover, meaningful validated predictions from two-phase study simulations have been very limited to data. Thus, many researchers prefer to work on the single-phase gas flow without the liquid phase being considered [78].

Use of numerical and experimental methods of the single-phase gas flow helps better understanding of the gas atomization process. Most of the numerical investigations on the gas atomization process were focused on the nozzle and gas die design and effect of that on the gas flow behaviour, wake closure phenomena and aspiration pressure.

2.3.1 CFD study of gas flow behaviour and melt nozzle design at CCGA

In 1996, Mi et al. [79] compared the numerical simulation results for a single-gas flow around the melt nozzle with the experimental data. The parametric variation of atomization gas pressure on the recirculation zone, mixing gas shear layer, oblique shocks, and Mach disk formation were investigated and proved in a good agreement with the experimental data. They demonstrated the gas flow behaviour around melt nozzle is changed at different atomization gas pressures [79].

Mi et al. [80], used CFD methods of gas-only flow to observe the effect of melt nozzle geometry variation on aspiration pressure at high pressure gas atomization. In this investigation different melt tip extension length and melt tip taper angle were numerically compared (Figure 32). Their numerical results indicated that, the aspiration pressure is fully affected by changing the melt nozzle tip length. The fully retracted melt nozzle developed overambient gas pressure along the melt tip base, so caused a problem for stable atomization; however, a fully extended melt tip increased the melt flow rate from the tundish into the nozzle tube and developed subambient pressure over a wide range of atomization pressure. The numerical results also showed that a small nozzle tip taper angle encouraged aspiration pressure while a larger nozzle tip taper angle developed the melt suction from tundish into the melt nozzle tube [80].

XinMing et al. [81] reported a numerical investigation on the gas flow behaviour around the melt nozzle at different atomization gas pressures. They investigated the aspiration effect and position of the Mach disk with an annular slit HPGA gas die (Figure33). They found that the aspiration pressure decreased and then increased by increasing atomization gas pressure. Figure 34 shows the effect of atomization gas pressure on aspiration pressure in both numerical and experimental test, which indicates the WCP at this condition [81]. Furthermore, they observed the position of the Mach disk could be changed by increasing the gas pressure and moved away from melt tip.

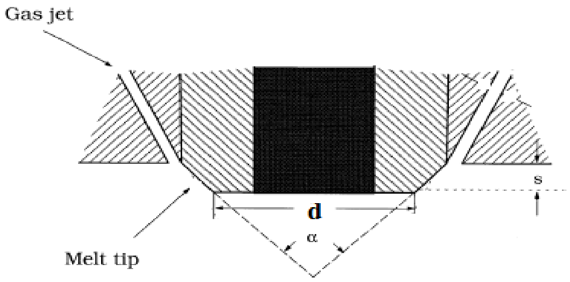

Nozzle type	1	2	3	4
Tip length s (mm)	0	1.93	2.34	3.86
Tip taper angle α (degree)	0	30	45	63
Tip base diameter d (mm)	10	8.43	8.09	6.83

Figure 32. The cross section view of melt nozzle design used by J Mi [80].

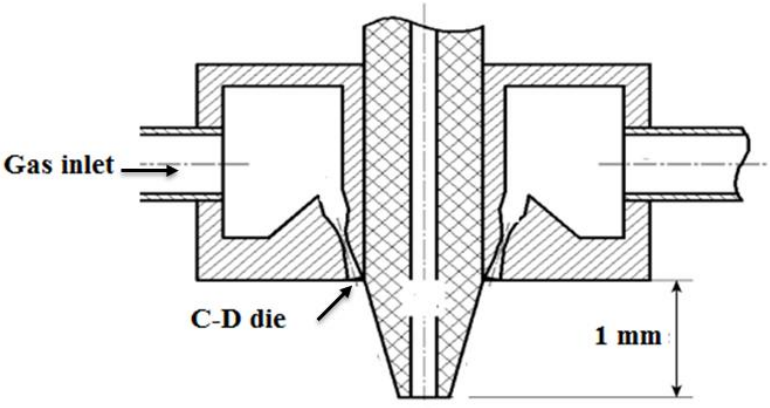

Figure 33. The cross section view of melt nozzle and HPGA gas die system used by XinMing [81].

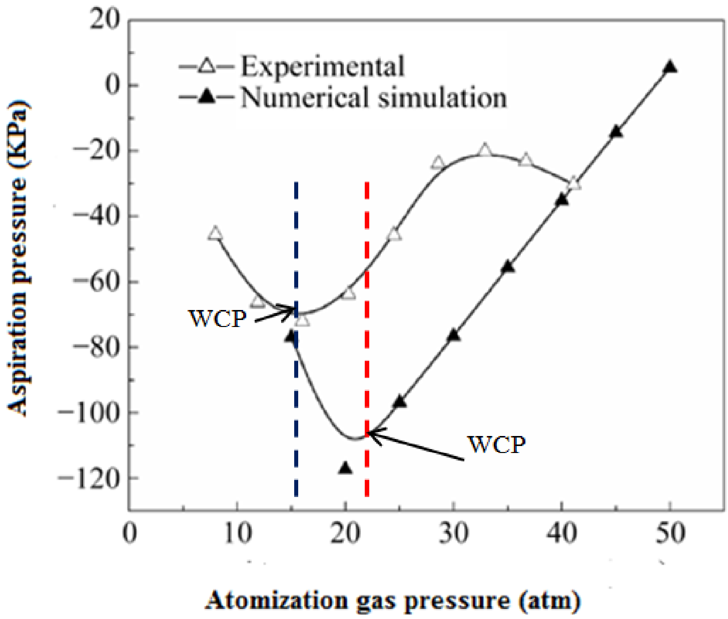

Figure 34. The comparison of aspiration pressure in terms of atomization gas pressure at experimental and numerical test [81].

Ting and Anderson [82] also reported the CFD results of open and closed-wake condition for CCGA process. They numerically modelled a single-phase gas flow of an annular slit gas die at different inlet gas pressures. These investigations were more focused on WCP, shock waves around the melt nozzle and creation of Mach disk at front of melt nozzle tip. Their results also showed the deep subambient aspiration pressure at closed-wake condition is highly affected by the low stagnation pressure at the recirculation zone. In addition, they showed two separated zones of primary and secondary recirculation zone and Mach disk at closed-wake condition. Figure 35 illustrates the numerical velocity field at the closed-wake condition proposed by Ting and Anderson [82]. The Mach disk, primary and secondary recirculation zone are also shown in this figure.

Espina et al. [69] reported the numerical results of the wake closure phenomena in a single-phase gas flow study. They found the same results of Ting on Mach disk formation at closed-wake condition and two recirculation zones at closed-wake condition [69].

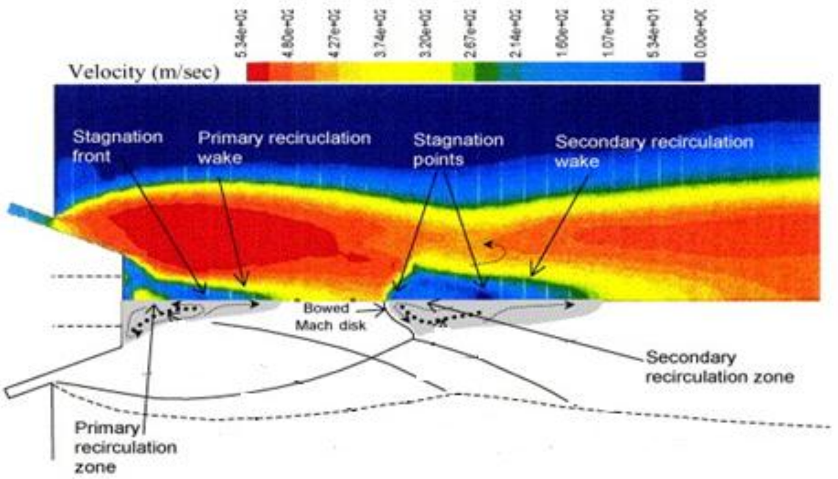

Figure 35. CFD result showing velocity profile $(\mathrm{m}\,\mathbf{s}^{-1})$ for the closed-wake condition with Mach disk, primary and secondary recirculation zone at front of melt delivery nozzle at atomization gas pressure of 4.8 MPa [82].

Moreover, Zeoli et al. [83,84] used the CFD methods to simulate the single-phase compressible gas flow in a HPGA gas die with two different nozzle tip length size known as Isentropic plug nozzle and a nozzle with shorter tip length in order to reduce the internal shocks and maximising the gas kinetic energy. The velocity field of these nozzles are depicted in figure 36 [83, 84]. This figure shows the oblique shocks, which decrease the gas jet kinetic energy. By improving the melt nozzle geometry, in figure 35b, less shock waves from around the melt nozzle tip.

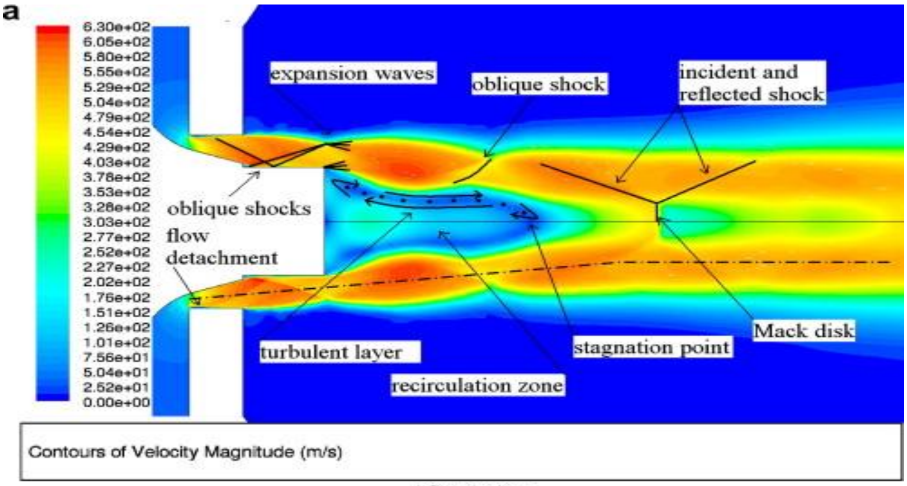

ASN design

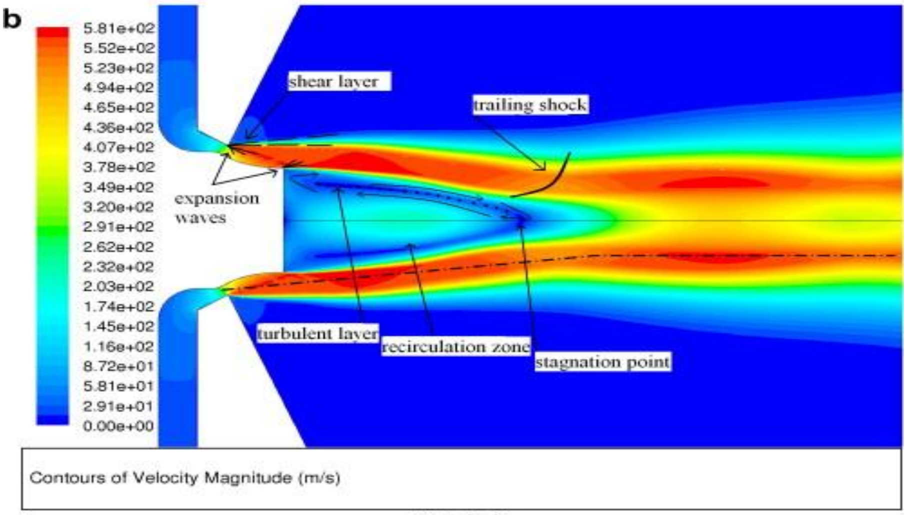

IPN design

Figure 36. CFD results of velocity profile (m $\mathbf{s}^{-1}$) of two different melt delivery nozzles of a: annular slit gas die with conventional melt nozzle b: Isentropic plug melt feed nozzle [83].

2.3.2 Flow separation problem at CCGA

As noted in section 2.2.4, one of the problems during the gas atomization process is gas flow separation and nozzle deformation. The boundary layer separation of the gas jet from outer wall surface of the melt nozzle was a major cause of the melt nozzle deformation in the gas atomization process [86, 87]. There are few numerical investigations on this problem. Aydin et al. [88] used a CFD commercial package to investigate the flow separation problem in a single-phase gas flow with an annular slit gas die. Their results showed the flow separation alongside a fixed melt nozzle length is strongly influenced by a high atomization gas pressure [88]. Figure 37 shows the total pressure contour and the effect of atomization gas pressure on flow separation around melt delivery nozzle. It shows that, with increasing the gas pressure, the flow separation increases [88].

To sum up, use of single-phase numerical methods at the gas atomization process help to optimize the atomization parameters, which influence the production efficiency at the real atomization system. Moreover, the numerical methods decrease the production cost and help to improve the gas die and the melt nozzle design, which may difficult to investigate experimentally [87, 88].

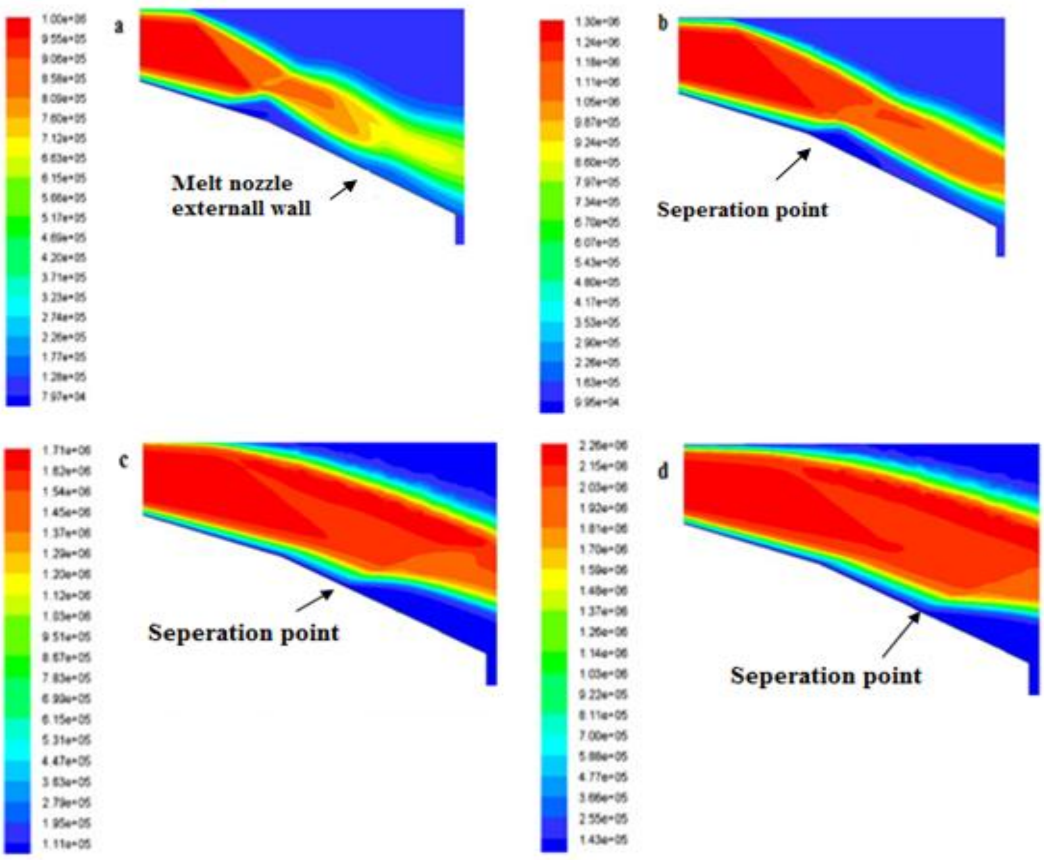

Figure 37. CFD result of total pressure contour (Pa) of flow separation around melt nozzle at different gas pressure of a: 1MPa, b: 1.3 MPa, c: 1.7 MPa and d: 2.2 MPa [88].

3 Experimental procedure

3-1-Experimental equipment of analogue atomizer

This section explains the experimental equipment and optical Schlieren technique used in this study for visualizing the gas flow pattern around the melt delivery nozzle in the CCGA process.

3.1.1 CCGA analogue atomizer

To visualise the gas flow pattern around the melt delivery nozzle, an analogue atomizer has been constructed with the features seen in the real atomizer by the previous researcher [58, 59, 60, 61]. The analogue atomizer is a replica of a full-scale metal atomizer of Phoenix Scientific Industries (PSI) close-coupled gas atomizer at the CERAM Research Centre; and is designed to atomize water. For this particular study, the system was set-up for single-phase gas flow. Air was used in the system as the gas flow and was supplied with four 0.08 m^3 air bottles with maximum air pressurised to 20 MPa. The air bottles are connected to the inlet high-pressure regulator to supply a steady gas flow to the gas die at the gas pressures up to 5 MPa. The gas die and melt delivery nozzle are mounted on the mounting plate on analogue atomizer similar to PSI system set-up. The atomizing chamber is designed in a perspex cube shape for a safe operation at high velocity gas jet. The schematic view of the analogue atomizer is shown in figure 38.

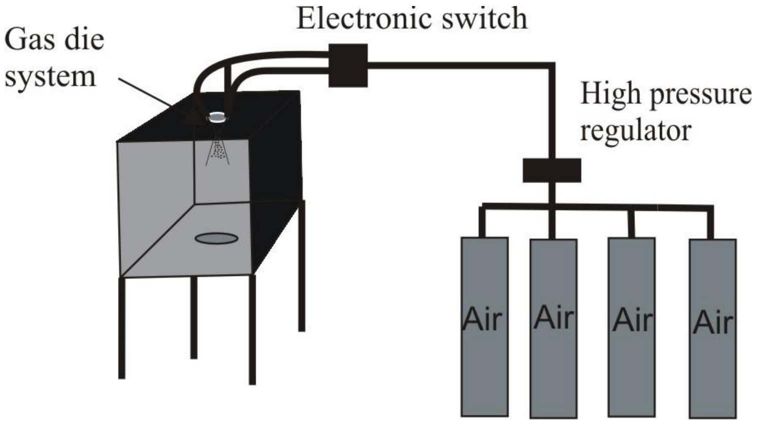

Figure 38. The schematic view of the analogue atomizer.

3.1.2 Melt delivery nozzle and gas die system for analogue atomizer

Seven-prototype melt nozzles were used in this study. These nozzles were previously designed and made by McCarthy [58]. The nozzles had different internal and external profile geometry and were made from brass. Four of these melt nozzles had the same external geometry, but different internal profile, which they are categorized as the nozzle set 1. These sets are known as nozzles type 1 to 4.The nozzle set 2 is comprised of three nozzles; two of them or nozzles type 5 and 6 had the shortest melt nozzle tip length with flat head for nozzle type 5 and grooved shape for nozzle type 6. The last nozzle in this group had the longest melt tip protrusion length among these sets and is known as nozzle type 7.

3.1.2.1 Melt delivery nozzle set 1

In nozzles set 1, the nozzle type 1 (Flat head) is the basic and most industrial design used in most commercial atomizers. The external geometry can be varied and for this test, nozzle tip is 4.9 mm diameter central bore. Nozzle type 2 is a simple design of trumpet bell design presented by Anderson et al. [53] with 5 mm diameter central bore and flare tip. Nozzle type 3 is similar to nozzle type 2, but without the lip at the tip of melt. The hemispherical profile is provided in nozzle type 4 and is more similar to concave melt nozzle proposed by Anderson [53]. All of melt nozzles in this set have the melt nozzle orifice of 2 mm in diameter and total length of 36.5 mm with 8 mm protrusion length below the gas die. Figure 39 shows the geometry details of these four nozzles.

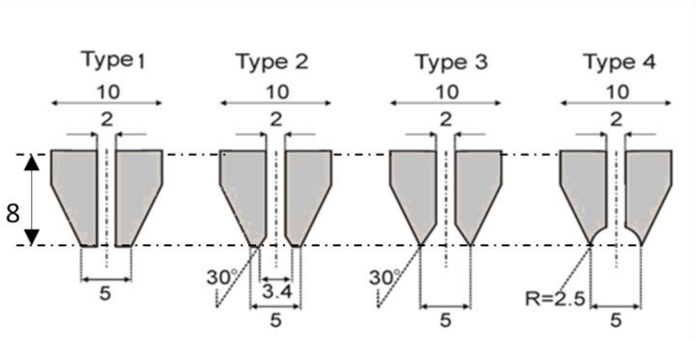

Figure 39. The schematic view of the melt nozzles set 1 and internal/external geometry. (Dimensions are in mm).

3.1.2.2 Melt delivery nozzle set 2

This nozzle set is designed with different melt tip length and internal profile. Nozzles type 5 and 6 have the overall length of 36 mm and protrusion tip length of 5 mm. The nozzle tip length reduction causes wider flat melt tip up to 2.5 mm for nozzles type 5 and 6 compared to nozzles in set 1. The nozzle type 7 with the longest protrusion tip of 12.5 mm has no lip around nozzle tip and is designed to inject the melt stream directly to the focal point of the gas jet. The details of these nozzles are shown in figure 40.

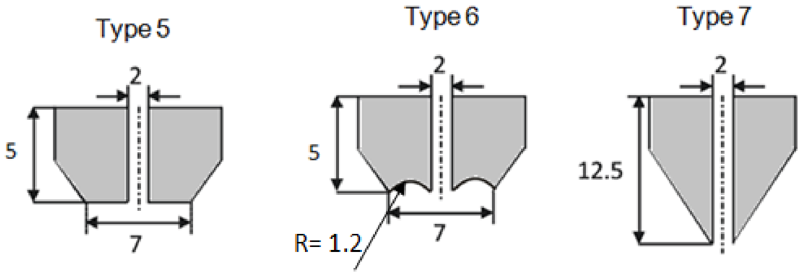

Figure 40. The schematic view of the external geometry of nozzle set 2. (Dimensions are in mm).

3.1.2.3 Gas die system design

Two different gas dies systems are used in this study: The cylindrical choked and the C-D gas die design. Both gas dies have 18 discrete holes. The dies are constructed on two parts. The top section of die is compressed of the external wall of plenum; the lower part of the die which can be either cylindrical or C-D is screwed directly to the upper part; and the 'O' ring at the top and bottom of the plenum sealed the gas die. Once the gas die parts are tightly screwed to each other the gas die parts are fitted with four bolts to the mounted plate inside the analogue atomizer. The melt nozzle, gas die and melt nozzle position on the analogue atomizer is shown in figure 41. Figure 42 shows the cylindrical choked and the C-D gas die profile. The apex angle of both gas dies are 45 degree. The C-D gas die is designed for exit gas jet velocity of Mach 2.6 at an ideal operation pressure of 3±0.5 MPa.

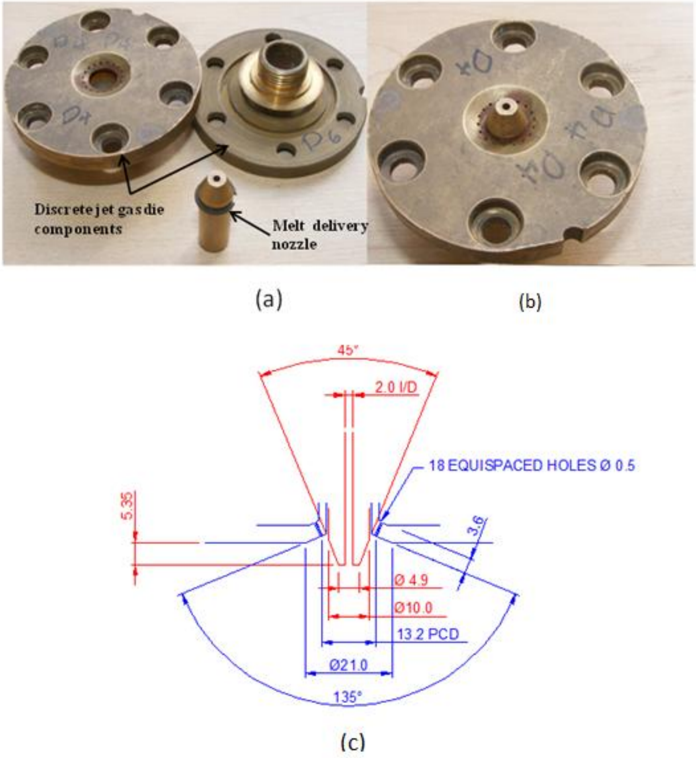

(a) (b)

(c)

Figure 41. (a) The discrete gas jet dies components and melt delivery nozzle, (b) Melt and discrete gas die set-up, (c) Gas die and nozzle design dimentions. (All dimensions in mm)

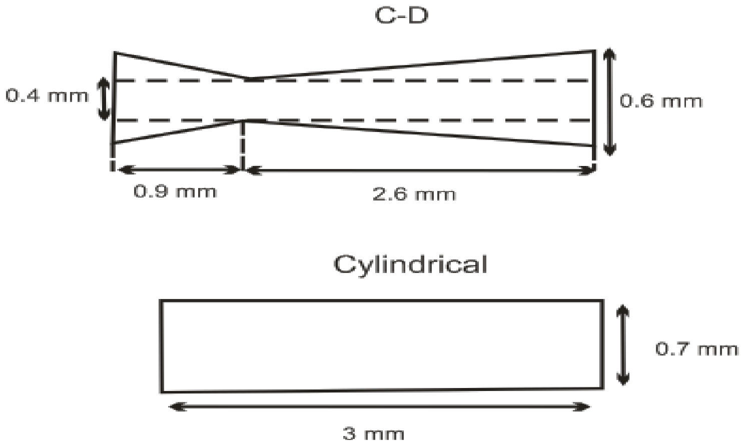

Figure 42. The C-D and cylindrical choked gas die internal profile dimensions.

3.2 The Schlieren set-up

As mentioned in section 2-2-4 on Töpler Schlieren technique, this type of lens arrangement has been chosen for visualizing the gas flow pattern. According to the position of analogue atomizer and the lab space for this particular work the Töpler Schlieren lens arrangement has been chosen. Two convex lenses with 15.24 cm in diameter and 70 cm focal length were used. The diameters of lenses and focal length have been chosen based on the working space and how far it is needed to visualize the gas flow pattern around the melt nozzle tip. The lenses were made from Barium Crown known as BaK for decreasing the chromatic aberration as much as possible for achieving sharp Schlieren image. For the source of light in this Schlieren arrangement, a halogen lamp also has been used.

The Schlieren images were recorded with a Photron ‘FASTCAM SA 5’ high-speed digital motion analyzer (Figure 43) fitted with a high magnification lens and operating at a frame rate of 15000 f/s and resolution of 750×750 pixels and the images were play backed by commercial software. The duration of gas running to the system for each test was about 3.5 seconds. This running time was chosen due to maximum recording time of high-speed camera at the particular image resolution. Due to steady gas flow field around the melt delivery nozzle, just one still image of high-speed camera recording was selected for further investigations. Moreover, the images of gas flow pattern were investigated from 4D from melt delivery nozzle tip (which D is diameter of the melt delivery nozzle tip).

Figure 43. The high-speed camera used in this study.

4 Numerical procedure

4.1 CFD theory and methodology

In this chapter, the CFD theory and models implemented will be presented and the methods for the numerical modelling at CCGA will be outlined.

In order to undertake a CFD study, there are procedures that can be followed for solving a range of different kinds of fluid dynamics problems. An overview of the process will be summarised. Firstly, the physical bounds or geometry of the problem must be defined. This is a relatively complex (and often iterative) process as it involves determining what boundary condition data will be available for a given domain, the likely complexity associated of solving for a given domain and making simplifications that will not lose the essential physics of the problem. Second, the volume occupied by the geometry of the fluid is divided into discrete cells known as the mesh (over which the numerical governing equations will be solved). Third, the boundary conditions are defined. The boundary conditions determine the flow behaviour in the model domain. In transient problems, the initial conditions also need to be defined. Fourth, the governing equations can be solved iteratively either to a steady state or transiently including appropriate turbulence models where appropriate. Finally, the results can be visualized with a postprocessor for further analysis at which point the results can be validated. These steps provide a process to run a CFD simulation, but equally importantly is to ensure that the assumptions of the problem being modelled are appropriate and that the complexity of the physical process being considered has been reliably captured in the selection of the domain, mesh, boundary conditions and governing equations.

There are numbers of CFD codes available commercially such as OpenFOAM, Comsol, ANSYS Fluent and ANSYS CFX etc, which can be used for implementing CFD and for solving a wide range of numerical problems.

Among them, ANSYS Fluent is a powerful code that can be used for a wide range of numerical investigations and is well used for gas atomization process studies. The numerical results obtained with this code generally show a good prediction of the gas flow behaviour for single-phase gas flow in studies of the gas atomization process [82, 83]. In addition, experimental results like Schlieren images are mostly shown to be in a good agreement by numerical results observed from this package; therefore, this solver will be used in this study.

4.2 Navier-Stokes equations

The Navier-Stokes equations are time dependent continuum equations for conservation of mass, momentum, and energy. They describe the relation between pressure, temperature and density of moving fluids. These equations are obtained by applying on Newton's second law of motion fluid [91, 93]. These types of equations were firstly introduced by Claude-Louis Navier and George Gabriel Stokes [91]. The Navier-Stokes equations are generally nonlinear partial differential equations, but for simplicity can be considered as linear equations. The Navier-Stokes equations for compressible flow are referred to these equations:

Mass equation:

$$\frac{\partial \rho}{\partial t} + \nabla(\rho u) = 0 \tag{12}$$

Momentum equation:

$$\rho\left(\frac{\partial u}{\partial t} + u.\nabla u\right) = -\nabla p + \nabla \upsilon \tag{13}$$

Energy equation:

$$\frac{\partial E}{\partial t} + \nabla[(E + p)u] = \nabla(\upsilon.u) + \nabla(\nabla\, \mathrm{T}.\lambda) \tag{14}$$

In addition, momentum equations in cylindrical polar coordinates are:

In r component:

$$\rho\left(\frac{\partial u_{\mathrm{r}}}{\partial t}+u_{\mathrm{r}}\,\frac{\partial u_{\mathrm{r}}}{\partial \mathrm{r}}\;+\;\frac{\partial u_{\theta}}{\mathrm{r}}\,\frac{\partial u_{\mathrm{r}}}{\partial \theta}-\;\frac{u_{\mathrm{r}}^{2}}{\mathrm{r}}+u_{z}\,\frac{\partial u_{z}}{\partial \mathrm{z}}\right)=-\;\frac{\partial \rho}{\partial \mathrm{r}}+\rho g_{\mathrm{r}}+$$

$$\mu\left[\frac{1}{\mathrm{r}}\;\frac{\partial}{\partial \mathrm{r}}\left(\mathrm{r}\frac{\partial u_{\mathrm{r}}}{\partial \mathrm{r}}\right)-\;\frac{u_{\mathrm{r}}}{\mathrm{r}^{2}}+\frac{1}{\mathrm{r}^{2}}\,\frac{\partial^{2} u_{\mathrm{r}}}{\partial \theta^{2}}-\;\frac{2}{\mathrm{r}^{2}}\,\frac{\partial u_{\theta}}{\partial \theta}+\frac{\partial^{2} u_{\mathrm{r}}}{\partial z^{2}}\right] \qquad (15)$$

In θ components:

$$\rho\left(\frac{\partial u_{\theta}}{\partial t}+u_{\mathrm{r}}\,\frac{\partial u_{\theta}}{\partial \mathrm{r}}\;+\;\frac{\partial u_{\theta}}{\mathrm{r}}\,\frac{\partial u_{\theta}}{\partial \theta}-\;\frac{u_{\theta}u_{\mathrm{r}}}{\mathrm{r}}+u_{z}\,\frac{\partial u_{\theta}}{\partial \mathrm{z}}\right)=-\frac{1}{r}\,\frac{\partial \rho}{\partial \mathrm{r}}+\rho g_{\theta}+$$

$$\mu\left[\frac{1}{\mathrm{r}}\;\frac{\partial}{\partial \mathrm{r}}\left(\mathrm{r}\frac{\partial u_{\theta}}{\partial \mathrm{r}}\right)-\;\frac{u_{\theta}}{\mathrm{r}^{2}}+\frac{1}{\mathrm{r}^{2}}\,\frac{\partial^{2} u_{\theta}}{\partial \theta^{2}}+\;\frac{2}{\mathrm{r}^{2}}\,\frac{\partial u_{\mathrm{r}}}{\partial \theta}+\frac{\partial^{2} u_{\theta}}{\partial z^{2}}\right] \qquad (16)$$

In z components:

$$\rho\left(\frac{\partial u_{z}}{\partial t}+u_{\mathrm{r}}\,\frac{\partial u_{z}}{\partial \mathrm{r}}\;+\;\frac{u_{\theta}}{\mathrm{r}}\,\frac{\partial u_{z}}{\partial \theta}+\;u_{z}\,\frac{\partial u_{z}}{\partial \mathrm{z}}\right)=-\frac{\partial \rho}{\partial \mathrm{z}}+\rho g_{\mathrm{z}}+$$

$$\mu\left[\frac{1}{\mathrm{r}}\;\frac{\partial}{\partial \mathrm{r}}\left(\mathrm{r}\frac{\partial u_{z}}{\partial \mathrm{r}}\right)+\;\frac{1}{\mathrm{r}^{2}}\,\frac{\partial^{2} u_{z}}{\partial \theta^{2}}+\frac{\partial^{2} u_{z}}{\partial z^{2}}\right] \qquad (17)$$

Where ρ is defined as the fluid density (kg m^{-3})' u is fluid velocity (m s^{-1}), p pressure (Pa), T temperature of the flow, λ is thermal conductivity (kg m s^{-2}), E is energy and υ is viscous stress tensor (kg s^{-1}m^{-1}).

4.3 Modelling domain

For defining the domain geometry different tools such as Computer Aid Design (CAD) can be used. The geometry may be in 2 or 3 dimensions based on the solution approach [89]. The domain geometry needs to be selected carefully in the context of what boundary conditions are known.

4.4 Mesh generation

After establishing suitable domain geometry, prior to running the simulation analysis, the domain volume is split into small discrete parts known as elements or mesh (Figure 44). Then the governing equations are discretized and solved inside each of these elements. The combination of all the elements makes the whole mesh of the domain geometry. This process for obtaining the appropriate mesh is known as mesh generation or grid generation stage [89, 90].

Due to different approaches used to solve the problems in 2D or 3D dimensions, the shape of these elements can be vary from being triangular in shape or quadrilateral (quad) for 2D to tetrahedral (tet) for 3D. It's very important to have a large mesh to capture the important flow and heat transfer gradients in the numerical domain. However, it must be considered that the more elements in the domain, the more computer calculation time is needed [90]. The adequate number of elements inside the numerical domain is typically determined by a mesh independence study which is discussed on section 4-6. Furthermore, the mesh quality inside the domain is a factor that affects the CFD solutions.

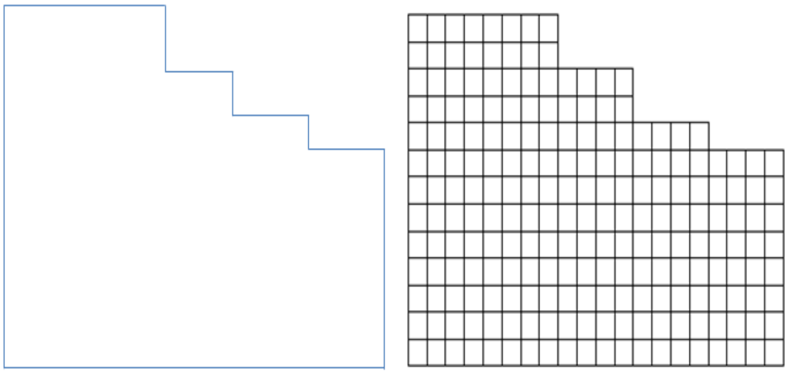

Figure 44. A schematic view of a 2D quad mesh with a modeling domain.

4.5 Discretization scheme

Generally, in mathematics, discretisation is concerned with the process of converting continuous models and equations into discrete counterparts. In fluid dynamics, there are a number of approaches to numerically solve the equations such as Navier-Stokes equations [91, 92]. Some of the major approaches are summarised below.

4.5.1 Finite Volume Method (FVM)

One of the most versatile discretization methods in CFD is the Finite Volume Method (FVM). The governing equations particularly Navier-Stokes equations, solve in this method over discrete control volumes where the variable of interest is located at the centroid of the control volume [91]. Then the differential forms of governing equations are integrated over each control volume and called discretized or discretization equations. Many CFD software packages such as ANSYS Fluent used of this method for solving the governing equation.

4.5.2 Finite Element Method (FEM)

The Finite Element Method (FEM) or Finite Element Analysis (FEA) is a numerical technique generally for structural analysis of solids, but has been adapted for using in fluids. This method is used for finding the approximate solutions to partial differential equations such as the Navier-Stokes equations. In other words, FEM divides complicated problems or equations into small elements that can be solved in relation to each other. Solving the problems with FEM method typically needs more computer memory compared to that of FVM [91, 93].

4.5.3 Finite Difference Method (FDM)

As a simple explanation, the Finite Difference Method (FDM) uses the approximate solution for the simple difference equations [91]. This method is mostly used in few special fluid mechanics codes, which handle simple geometry.

4.5.4 Turbulence models

Most of the fluid flow in reality contains turbulence and vortexes. The fluid motion is characterized by apparently random and chaotic three-dimensional vortices. Solving the full Navier-Stokes equations in turbulent fluid flow is a complicated process as a very fine mesh would be required to capture the small-scale vortices There are some numerical approaches suggested for solving flows that include turbulence. The main CFD approaches are Direct Numerical Simulation (DNS), Large Eddy Simulation (LES), and Reynolds Averaged Navier–Stokes equations (RANS).

DNS involves solving Navier-Stokes equations directly and does not require an additional turbulence model. DNS needs very fine mesh throughout the numerical domain in order to resolve all spatial and temporal scales in the flow. Therefore, the computational cost of DNS method is very high and mostly used for low Reynolds number flows, as it is not possible to use this approach for fluids with a high Reynolds number, due to computational cost [91, 92].

LES is another CFD approach for solving the turbulence in the flow and is appropriate for solving transient flows. When compared with DNS, LES reduces the computational cost and calculations by eliminating the resolving of the small-scale eddy directly with the Navier-Stokes equations and therefore can be used to solve fully turbulent flows [91, 92].

The RANS approach is used where small scale turbulent fluctuations are averaged out. This provides a good approach for predicting the steady state flow field and avoiding the high computational cost of LES. However, a turbulence model is required to model the additional Reynolds stress terms that appear in the RANS equations. This method is widely used in industry and has become the general standard approach in solving most of engineering problems including those associated with the gas atomization process. The Schlieren images for gas only flow during the gas atomization process, revels that gas flow field around the melt delivery nozzle is almost steady-state and as such the use of RANS models for steady-state flow is more practical than the previous methods and discussed as well by many researchers. A RANS approach is taken in this study.

4.5.5 Reynolds Averaged Navier–Stokes (RANS) method

The general form of the RANS momentum equation can be written for a constant density and as a Cartesian tensor for average fluid motion as:

$$\rho\left[\frac{\partial \hat{u}_i}{\partial t}+\hat{u}_j\frac{\partial \hat{u}_i}{\partial x_j}\right]=-\frac{\partial \hat{p}}{\partial x_i}+\frac{\partial \hat{v}_{ij}}{\partial x_j} \tag{18}$$

Where $\hat{u}_i$ and $\hat{u}_j$ are the average fluid velocity components at the points of x_i and x_j at time; t. $\hat{p}$ is the average static pressure and $\hat{v}_{ij}$ is the average viscous stress. The average components also can be defined as:

$$\hat{u}_i = U_i + u_i \tag{19}$$

$$\hat{p} = p + p_v \tag{20}$$

$$\hat{v}_{ij} = v + \tau_{ij} \tag{21}$$

When U_i $,p$ and υ are known as the mean motion parameters for velocity, pressure and viscous stress, respectively. u_i, p_v and τ_{ij} are the fluctuating components of those mentioned parameters [95]. This equation can be extended and written for instantaneous fluid motion and incompressible Newtonian fluid with constant viscosity as below:

$$\rho\left[\frac{\partial u\hat{}_{\mathrm{i}}}{\partial t}+u\hat{}_{j}\frac{\partial u\hat{}i}{\partial x_j}\right]=-\frac{\partial p\hat{}}{\partial x_{\mathrm{i}}}+\frac{\partial v\hat{}_{ij}}{\partial x_j}-\rho\left[u\hat{}_{j}\ \frac{\partial U_{\mathrm{i}}}{\partial x_j}\right]\text{-}\rho\left[u\hat{}_{j}\ \frac{\partial u\hat{}_{\mathrm{i}}}{\partial x_j}-\left(u\hat{}_{j}\frac{\partial u\hat{}_{\mathrm{i}}}{\partial x_j}\right)\right]\ (22)$$

The two terms at the left hand side of this equation are the derivative of the fluctuating velocity; the first two terms on the right hand side of the equation represent the fluctuating pressure gradient; the fluctuating viscous stresses; and the third term is called production term (which is related to the fluctuation of fluid and turbulence) [91, 92]. The last term is known as the Reynolds stress. This is very important in relation to turbulence in the fluid. The most common way to resolve this extra term is use of linear eddy viscosity model [91].

Linear eddy viscosity models are divided into three models known as algebraic models, one-equation models and two equation models. Among them the algebraic and one equation models are relatively limited for complicated geometry and flows, but the two equation models are the most common models used for RANS. The two models are known as *k*-ε and *k*-ω turbulence models.

The two equation models represent two extra transport equations (convection and diffusion) of turbulent energy for solving the turbulence model [92]. The first variable of *k* is determined as the energy in the turbulence fluid; the second term epsilon (ε) variable is known as turbulent dissipation; and the variable of Omega (ω) is the specific dissipation [91].

- ***k*-ε model**

This model can be used widely in CFD method and can solve most of the single-phase fluid with free-shear layer flows and relatively small pressure gradients [91, 92]. The experimental results show that the accuracy of this model for solving the numerical models reduces for a system in which the flow contains large adverse pressure gradient. This model has some sub models and one of those is known as RNG *k*-ε model. The Re-Normalization Group (RNG) was first represented by Yakhot [92] and is a re-normalized format of Navier-Stokes equations. This model is used to enhance the accuracy and more control over the numerical calculation by damping or eliminating the small eddies effect on the fluid with replacing the mean effect of small eddies with large ones.

- ***k*-ω model**

The standard *k*-ω turbulence model is the second type of the most practical two-equations model which was presented first by Kolmogorov at 1942 [93]. A Different modification has been applied to this model over time by different researchers such as Saiy (1974) [94], Spalding (1979) [95], Wilcox (1988) [96], Speziale et al. (1990) [97] and Menter (1993) [98]. Similar to the *k*-ε model the first variable of *k* is energy of turbulence and ω is the variable that determines the scale of turbulence known as specific dissipation.

This model is more accurate than *k*-ε model for near wall treatment and low-Reynolds number; also, can be used as very accurate turbulence model for prediction of the flow separation conditions under adverse pressure gradients; and is a great improvement for predicting some gas jet flow separation condition such as gas flow separation around melt delivery nozzle at CCGA process [88]. Similar to the previous turbulence model, the *k*-ω model is divided into different sub-models and the most popular of them is the Shear-Stress-Transport (SST) *k*-ω turbulence model. Menter [98] first introduced this model in 1993. This model is useful for the flow separation study or stagnation region. This model increases the accurate prediction of flow separation phenomenon from a smooth surface, which other turbulence models such as standard k-ω model may fail to give such an accurate result of flow separation amount under adverse pressure gradient.

4.6 Boundary conditions

After determining the geometry of the numerical domain, it is necessary to specify the appropriate boundary and initial conditions for the flow and thermal variables of the numerical domain as well as all surfaces of any objects that lie within the domain [90, 91]. Each variable needs meaningful values at the boundary of the solution domain. For modelling fluid flow problems in a numerical domain wide range of boundary conditions (such as inlet and outlet pressure, mass or velocity to the numerical domain) can be specified. A variety of boundary conditions types are available including:

-General flow condition: inlet pressure and outlet pressure.
-Incompressible flow: inlet and outlet velocity.
-Compressible flow: Inlet and outlet mass flow plus inlet and outlet pressure.
-Boundary condition for walls of a numerical domain:
-Stationary wall
-Moving wall
-Slip and non-slip wall
-Smooth and rough wall
-Generally, selecting the boundary condition on the solution domain depends on the physical mode.

4.7 Convergence and domain independence study

As discussed in section 4-4, to solve the numerical equations inside the numerical domain, a good quality mesh with appropriate size is required to obtain a valid result. The accuracy of numerical results is highly related to meshing and boundary conditions applied to the numerical domain and the more accurate the mesh and boundary condition, the more accurate or converged the numerical solution. Insuring a fully converged solution for the CFD modelling is just one of the ways that we can ensure a valid calculation. Furthermore, it is important that the numerical solution is independent of the mesh resolution [92, 93].

- **Convergence solution**

Generally, in CFD modelling, the convergence of the solution relates to the residual error values or RMS error, which in steady state conditions can be satisfied under following conditions:
- The residual error values should be reduced to the acceptable low values during calculation. These values typically are suggested around 10^{-6} [91]. Also, For an iterative solver, the values for points in the flow (e.g. velocity, pressure, temperature, or mass flow etc) have reached a steady solution with respect to the iterations. This can be checked via use of point monitors to observe at key locations in the domain [91, 92].

- **Mesh independence study**

When increasing the primary mesh size inside the numerical domain and running the calculation for increasing mesh size, the result must be independence of the mesh size. To insure the solution is independent of mesh refinement, the solution is run using a primary mesh to obtain a converged solution (value point monitors becomes steady). This process is repeated by increasing the mesh refinement (generally would be around 1.5 times of the previous mesh) at each stage and the result can be compared. Once the result is independent of mesh refinement, the mesh at this stage is considered accurate enough to provide a mesh independent solution [90, 91, 92]. Therefore, to evaluate the mesh independence study, plotting different values of velocity or pressure against the different mesh sizes is a good approach [90, 91]. Comparing these variations (value points) at different mesh, shows in which mesh the result is constant and did not change by mesh refinement.

4.8 Numerical domain design

To numerically simulate the gas flow pattern around the melt delivery nozzle in this study, commercial CFD modelling package ANSYS Fluent was used. Based on the theoretical explanations in section 4-2 on the basic aspects of numerical modelling; first, the internal and external geometry of each nozzle set and gas die were drawn based on prototype nozzles that were used in the experimental tests. The melt nozzle dimensions are given in section 3-1-2-1. In addition, the model domain was solved in the r-z components of a cylindrical system (a 2D axis-symmetric domain is considered which approximates the 3D flow). This means an annular slit gas jet is used to approximate the ring of individual jets used in the experimental arrangement. The assumption is considered valid because in the first instance as when observing the Schlieren images of the gas flow field from the gas-only phase of the analogue atomiser (whether with cylindrical choked or C-D discrete jet die set-up at section 5) the result of the combination of jets forms an approximately uniform radial profile. Moreover, due to this assumption the annular slit gas die set-up was considered for the CFD simulations. Figure 45 shows the numerical domain of a 2D plane of the melt nozzle type 1 with a cylindrical choked gas die. This domain was used for the CFD simulation and is known as the normal domain.

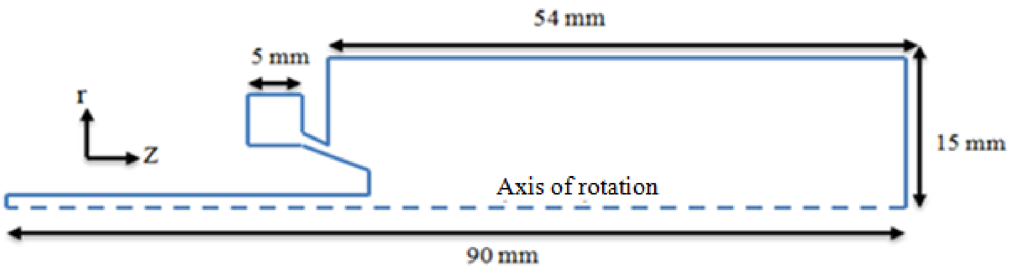

Figure 45. The normal numerical domain dimensions used in this study.

4.8.1 Numerical model assumptions

A CFD study was conducted into the high-speed gas flow around each of the nozzles set. As the flow is supersonic, the gas is required to be modelled as a compressible fluid and as such conservation equations for continuity, momentum and energy were all solved. For each study, a single-phase steady-state flow field was simulated based on solving the RANS equations. Since the flow is in the turbulent regime, the k-ω-SST model has been applied to solve the Reynolds stress terms in RANS equations [88, 89].

The k-ω-SST model has been validated for high-speed internal flows and has been shown to give good predictions for the associated shocks [87, 88]. Furthermore, both k-ε-RNG and k-ω-SST turbulence models were applied during the investigation and the sensitivity of the results to different turbulence models was evaluated as a part of study and the results are presented in section 6.1.2. Moreover, due to flow separation study around the melt delivery nozzle external wall, the near wall treatment was also applied to the numerical model. To do this avery fine mesh with y plus of close to 20 was applied around melt nozzle external wall. The y plus value is a dimensionless distance and is defined as the distance (based on local cell fluid velocity) from the wall to the first mesh node. This number for k-ω-SST model should be between 10.8 and 30[87]. The SIMPLE algorithm with an implicit 2nd order upwind scheme is used to solve the RANS equations in the computational domain [87, 88].

In order to establish the numerical simulation of the gas flow and to simplify the numerical calculations, the following assumptions also have been made:

1- Flow is considered to be steady state.

2- Flow is considered 2D axis-symmetric.

3-The fluid is considered as air and modelled as a compressible ideal gas.

4-The impact of the molten metal is not considered.

5- For presentation purpose; the model is rotated 90 degree anticlockwise.

The ideal gas law for compressible flow is defines as:

$$p = \rho_A RT \qquad (23)$$

Where $$R = \frac{R_u}{\vartheta_{\mathrm{m}}} \qquad (24)$$

Where R_u is universal gas constant and ϑ_{m} is Molecular mass of air.

4.8.2 Boundary conditions

Figure 46 shows different boundary conditions on the numerical domain. Different atomization gas pressures are applied on the gas entrance (pressure inlet) of the numerical domain (for cylindrical choked and C-D gas die) ranging from 1 to 5 MPa (Unless stated otherwise pressure was increased in 0. 5 MPa increment in all numerical tests). It is expected for a C-D gas die, to produce overexpanded flow (at pressures below of 3 MPa) to underexpanded flow (at pressures above of 3 MPa). The downstream outlet was taken as a pressure condition at atmospheric pressure. The outer boundary of the chamber, melt nozzle, and gas die wall were taken as walls with a non-slip velocity condition. The non-slip boundary condition is defined when the moving fluid as the contact with a wall or any non-moving body has no velocity at the contact area [85, 86]. Furthermore, the boundary labelled ‘Upper domain boundary’ in figure 46 was also modelled as a wall with a non-slip condition and open-boundary condition as the outlet with atmospheric pressure and the results compared. For this boundary, calculations have been undertaken treating it as both an atmospheric pressure condition and as a non-slip wall condition (when treated as a pressure condition it was found that there was minimal flow across this boundary). Furthermore, for the energy boundary conditions, the gas temperature for the upper boundary flow inlet and exit were set at a constant temperature of 300 K.

Table 1 and 2 show an overview of the numerical boundary and turbulence boundary condition for two different boundary conditions. For observing the results of different boundary conditions at the domain, it is needed to define some extended numerical domain in both dimensions of r and Z direction. Also the numerical domain with and without gas chamber were designed for comparing the results of different boundary conditions at the gas inlet.

Table 1- An overview of the boundary conditions.

Boundary Type	Boundary condition test 1 (Momentum)	Boundary condition test 2 (Momentum)	Boundary condition (Energy)
Inlet to nozzle chamber	Pressure Inlet (determined from experimental test pressures)	Pressure Inlet (determined from experimental test pressures)	300 K
Downstream outlet	Pressure outlet (atmospheric)	Pressure outlet (atmospheric)	300 K
Chamber, melt nozzle and gas die wall	No-slip wall	No-slip wall	Insulating condition
Upper domain boundary	No-slip wall	Open boundary (atmospheric pressure)	300 K

Table 2- An overview of the turbulence boundary conditions.

Boundary Type	Turbulence Intensity (%)	Hydraulic diameter (mm)
Inlet to nozzle chamber	5	0.5
Downstream outlet	5	15

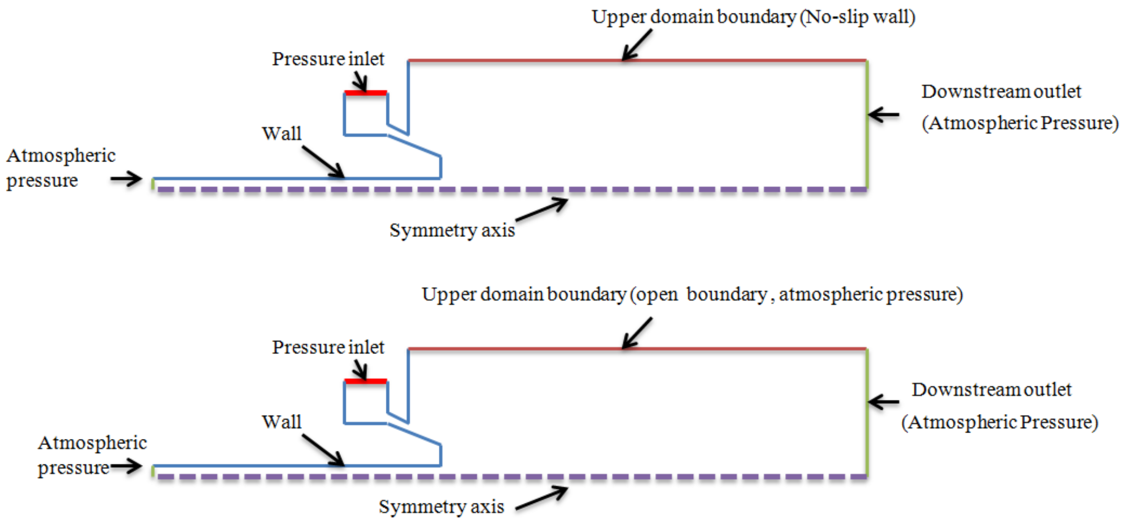

Figure 46. Boundary conditions applied on a numerical domain.

4.8.2.1 Domain independence studies

To understand how large the computational domain needed to be and to confirm the flow field predictions are not impacted by domain size and shape, two different sizes of numerical domain in the r and Z direction were designed. Figure 47 shows the normal and extended domain in the Z direction. The extension applied at front of melt nozzle tip. The normal domain has an extension (Figure 47a) about 10 D (D is melt nozzle tip diameter) from melt delivery nozzle tip. This distance is a normal distance in the numerical investigations and proposed in literatures [85, 86, 87]. The second extension (Figure 47b) is about 14 D from melt nozzle tip in the Z direction. This distance has been chosen to increase the far field area in front of melt delivery nozzle to ensure the boundary location is not affecting the flow. It also allows visualizing of the gas flow pattern at larger distance from the melt nozzle tip.

Furthermore, figure 48 shows the extended domain at r, which is about 5 D (25 mm). This extension was also applied to check that the boundary was not impact on the flow and allowed observing of the gas flow around the melt nozzle at increased distance in the r direction.

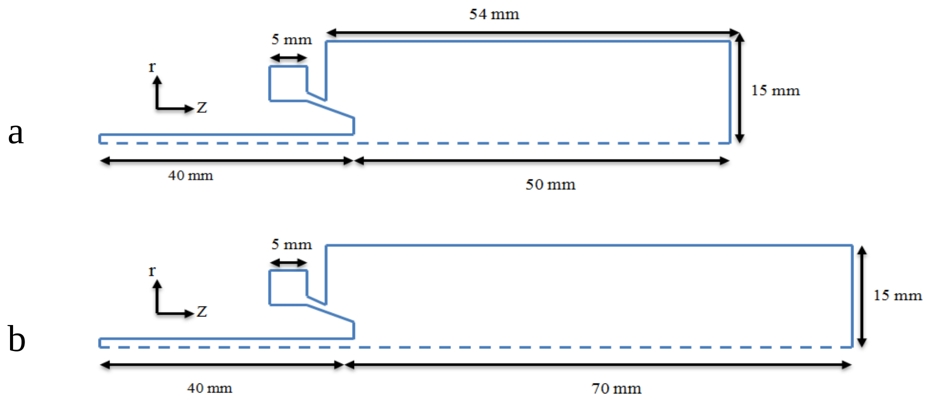

Figure. 47a: Normal numerical domain, b: Extended domain on Z direction.

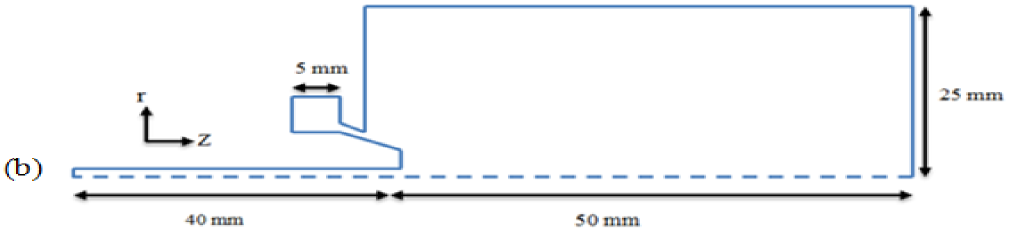

Figure 48. Extended domain on r direction.

4.8.2.2 Numerical domain with and without full gas chamber

Ensuring that inlet flow condition was implemented correctly and as close to the real experiment as possible was paramount. As such, a study on the implementation of the pressure inlet condition was undertaken.

Two numerical domains with and without gas chamber for different pressure input boundary conditions were tested. The chamber's dimensions were selected based on the experimental gas die set-up. Figure 49 shows the numerical domain of the gas die with and without gas chamber. The gas chamber dimension was also based on real gas atomization chamber used for analogue atomization. The same assumption also was used for a C-D gas die.

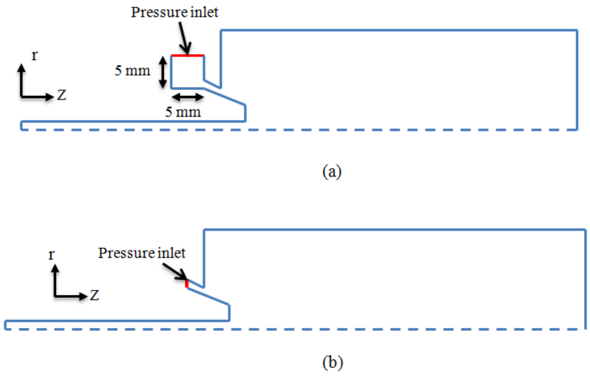

Figure 49. a: Numerical domain with gas chamber, b: Numerical domain without gas chamber.

4.8.3 Meshing process

After determining the numerical domains, it is required to apply the mesh to each domain. In this study, the ANSYS meshing tool workbench was used to apply mesh. For each mesh generation process, the numerical domain was considered in seven parts. Figure 50 shows different compartment inside the numerical domain. The same process was also applied to different domains for different melt nozzle set with a cylindrical choked or C-D gas die set-up. These compartments help provide more control over the mesh elements distribution throughout the numerical domain.

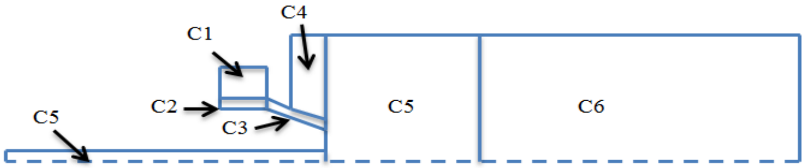

Figure 50. Different compartments and finer mesh area around melt nozzle.

Moreover, in different compartments were different mesh refinements were implemented due to gas flow behaviour being at different within the domain area. For example around the melt delivery nozzle in compartment C3, which is likely to have flow separation, a finer mesh is applied in comparison with the far the field area of C6 at front of melt nozzle tip (Figure 51).

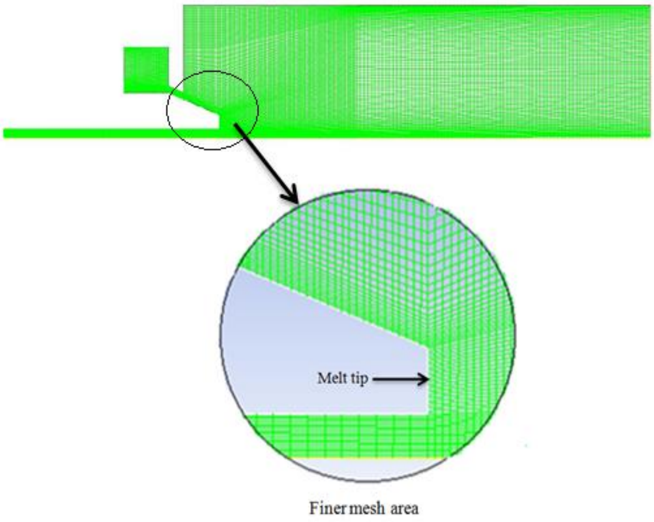

Figure 51. The normal domain mesh with exploded view of mesh quality around the melt nozzle.

4.8.3.1 Mesh independence study

As discussed, to ensure that the numerical results are independent of meshing resolution, it is necessary to apply different mesh refinements to the numerical domain with different mesh size cells.

Three different meshes are used: mesh 1 with 9000 elements; mesh 2 with 11000 elements; and mesh 3 with 18000 elements. These were applied to the numerical domains and the models were run until fully converged (with residual error values below 10^{-8}) To determine the influence of mesh refinement on the CFD solution and to ensure mesh independence, before proceeding to the numerical simulations, the gas velocity variation was monitored along the vertical lines AB and CD. The positions of these lines are shown in figure 52.The results of the mesh independence study are given in section 6-1-1.

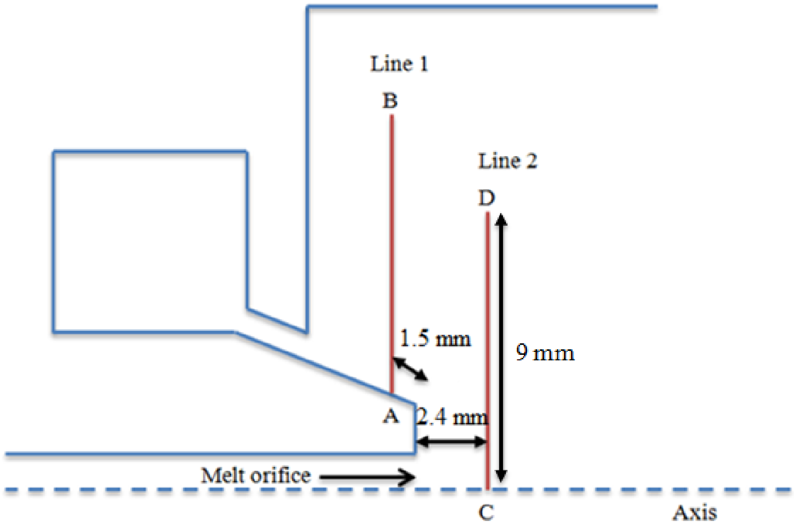

Figure 52. Position of two lines at front of melt tip and external wall of melt nozzle used for mesh independence study.

4.8.3.2 Assessing convergence solution

The first indication of a converging solution in a CFD model is that the residual errors reduce during the solution. After a number of iterations, these errors should become constant. In this study, the residual errors reduce for each solution reaching below 10^{-8} . In addition, the velocity was monitored at set locations in the geometry at each iteration until it reached to the steady solution and signifying that the velocity field was not changing with further iterations (and helping to signify the solution was converged).

5 Experimental results

In this section, the experimental results of Schlieren technique with two different gases die system of the discrete jet cylindrical choked flow and the C-D gas die with analogue atomizer was conducted. The effect of internal and external melt nozzle geometry on gas flow behaviour was also investigated.

5.1 Schlieren images of gas flow for melt nozzle set 1 with cylindrical choked gas die

After setting the Schlieren equipment, the analogue atomizer was run at different atomization gas pressures between 1 to 5 MPa (unless stated otherwise pressure was increased in 0.5 MPa increment in all experiments) for each melt delivery nozzle set 1. Figure 53 shows a still image of gas flow pattern of nozzle type 1 at gas pressure of 1 MPa. Due to the steady gas flow field around melt delivery nozzle, just one still image between 52500 images of high-speed camera recording was selected for further investigations for each test.

At the gas pressure of 1 MPa in nozzle type 1 (Figure 53), the gas flow expands rapidly from the gas die to the ambient gas pressure and makes some oblique shocks around the melt nozzle tip. Theses shocks reduce the gas jet velocity. Then, the gas re-accelerates then decelerates to form a set of Prandtl-Meyer waves at front of melt tip. At this pressure, the nozzle is in open-wake condition. The same open-wake condition was also seen in the gas pressures below of 4.5 MPa. At the gas pressure to 4.5 MPa (Figure 54), the open-wake condition changed to closed-wake condition; and more oblique shocks and the Mach disk appeared around and front of melt nozzle tip. The Prandtl-Meyer waves also can be seen at front of the Mach disk (Figure 54).

At the gas pressures above of 4.5 MPa, the gas flow pattern was also in the closed-wake condition. The WCP for nozzle type 1 was measured around 4.5 MPa.

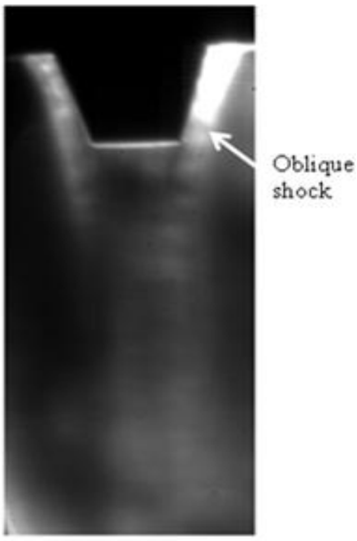

Figure 53. The Schlieren image and open-wake condition of gas flow for nozzle type 1 at atomization gas pressure of 1 MPa.

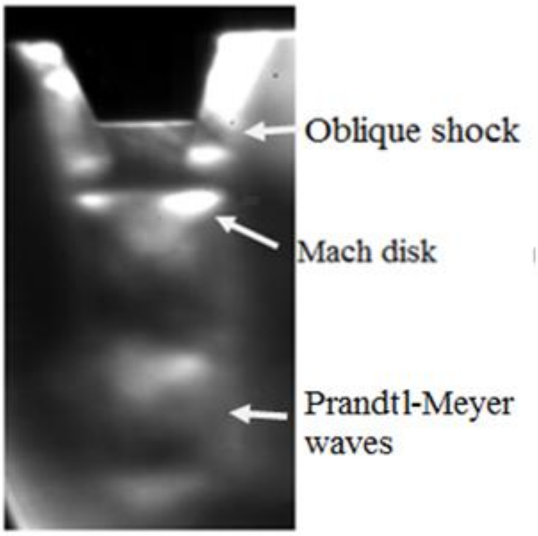

Figure 54. The Schlieren image of closed-wake condition of gas flow for nozzle type 1 at atomization gas pressure of 4.5 MPa.

In type 2, the open-wake condition was observed at the gas pressures below of 4.5 MPa (Figure 55a). The gas flow pattern and wake condition for this nozzle at different gas pressure are much similar to nozzle type 1. At the gas pressure of 4.5 MPa, the Mach disk appered at front of the melt nozzle tip and closed-wake condition was noticed (Figure 55b). The transition pressure for open to closed-wake condition (WCP) for nozzle type 2 was also measured approximately at 4.5 MPa.

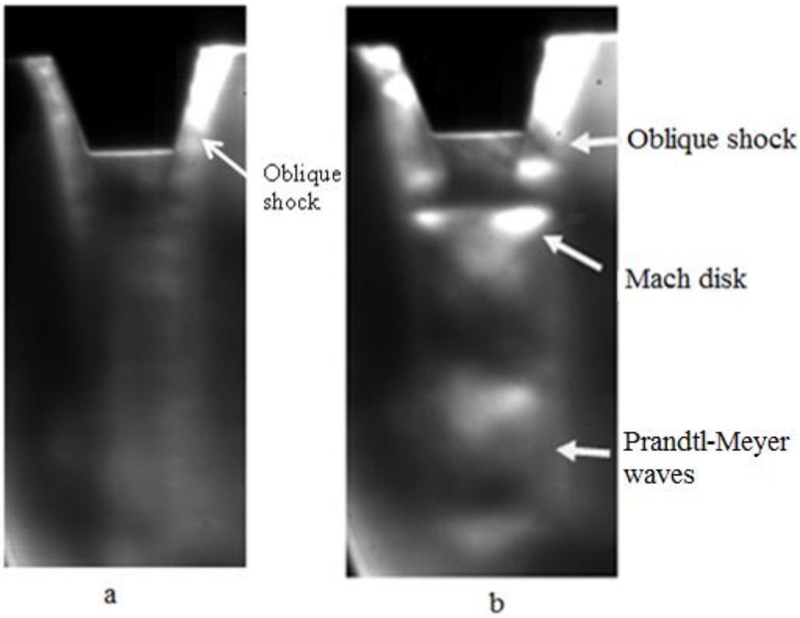

Figure 55. The Schlieren image of gas flow for nozzle type 2 at atomization gas pressure of a: open-wake condition at 1 MPa and b: closed-wake condition at 4.5 MPa.

The same test was applied to the nozzle type 3 with the same cylindrical choked flow gas die. In this nozzle, the open-wake condition was seen at the gas pressures below of 3.5 MPa (Figure 56a). At the gas pressure of 3.5 MPa, the Mach disk occurred and closed-wake condition was observed (Figure 56b). The WCP was measured around 3.5 MPa for nozzle type 3.

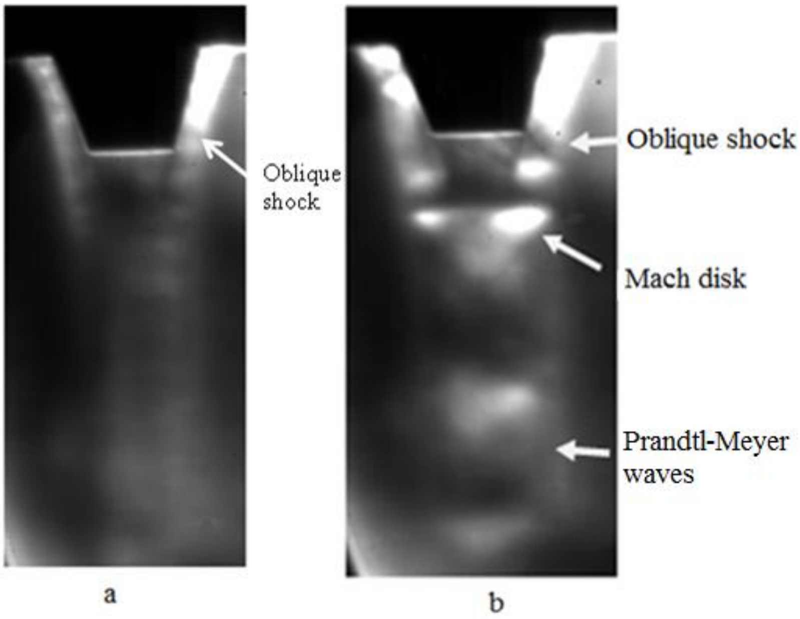

Figure 56. The Schlieren image of gas flow for nozzle type 3 at atomization gas pressure of a: open-wake condition at 1 MPa and b: closed-wake condition at 3.5 MPa.

In nozzle type 4 with a hemispherical tip design, the open-wake condition occurred at the gas pressures below of 3 MPa. The open-wake condition for this nozzle at gas pressure of 1 MPa is shown in figure 57a. The open-wake condition was transformed to the closed-wake at the gas pressure of 3 MPa (Figure 57b). Therefore, in type 4, the WCP was measured about 3 MPa. Nozzle type 4 had the lowest WCP among melt nozzles set 1. The summery of WCP transition pressure for nozzle set1 is given at table 3.

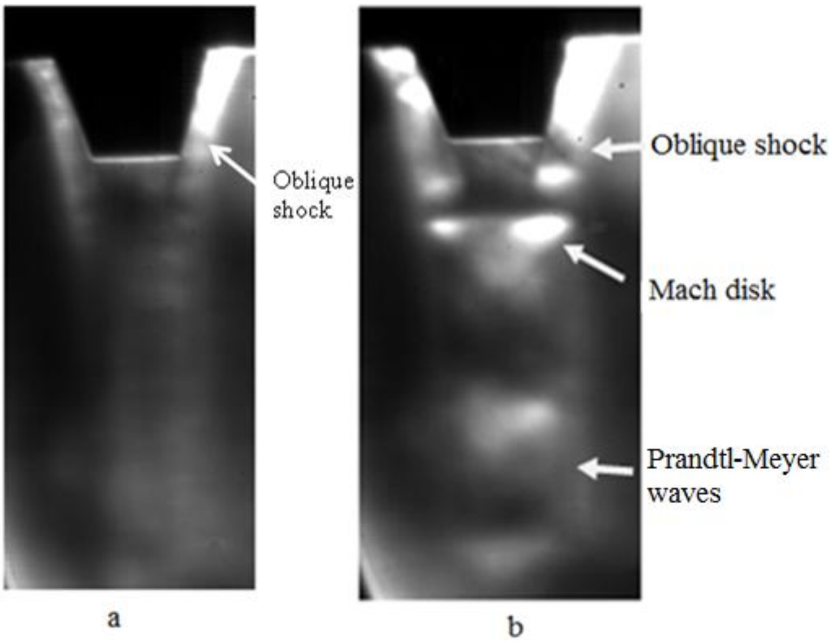

Figure 57. The Schlieren image of gas flow for nozzle type 4 at atomization gas pressure of a: open-wake condition at 1 MPa and b: closed-wake condition at 3 MPa.

Table 3. The WCP transition pressure for nozzle set 1 with a cylindrical choked gas die.

Nozzle type	WCP pressure (MPa)
Type 1	4.5±0.5
Type 2	4.5±0.5
Type 3	3.5±0.5
Type 4	3±0.5

5.2 Schlieren images of gas flow field for melt nozzle set 2 with a cylindrical choked gas die

The same series of tests also repeated for melt nozzle types 5, 6, and 7. The nozzles type 5 and 6 had the shortest melt nozzle tip protrusion length compared to nozzle set 1. According to Schlieren images of nozzle set 2, the gas wake condition in type 5 was seen under open-wake condition at the gas pressures below of 3.5 MPa (Figure 58a), but for type 6 with grooved tip design, this situation was observed at the gas pressures below of 2.5 MPa (Figure 58b). At the gas pressure of 3.5 MPa in type 5, the Mach disk and closed-wake condition began to form in front of the melt nozzle tip (Figure 59a). Figure 59b illustrates the Schlieren image of closed-wake condition for type 6. At higher gas pressures of 2.5 MPa, the closed-wake condition for this melt nozzle was also stable. Thus, The WCP for type 5 and 6 was measured around 3.5 and 2.5 MPa, respectively.

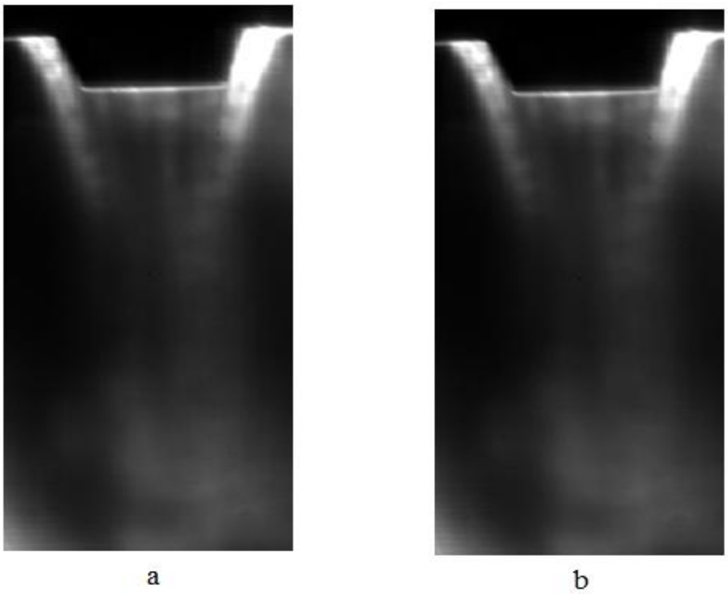

Figure 58. The Schlieren image and open-wake condition of gas flow for a: nozzle type 5 at the gas pressure of 3 MPa and b: nozzle type 6 at the gas pressure of 2 MPa.

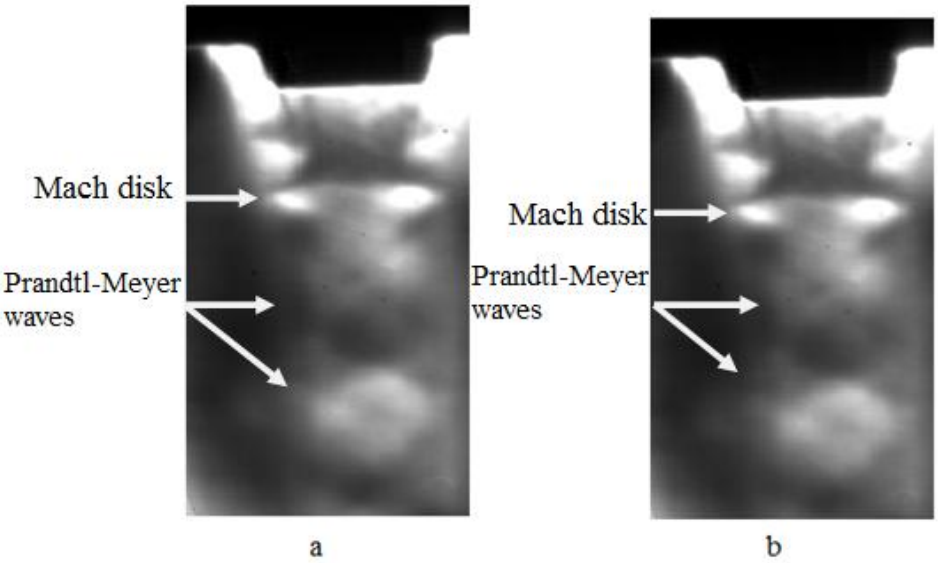

Figure 59. The Schlieren image and closed-wake condition of gas flow for a: nozzle type 5 at the gas pressure of 3.5 MPa and b: nozzle type 6 at the gas pressure of 2.5 MPa.

The last test was conducted on type 7 at the same operating gas pressures and same cylindrical choked flow gas die. This nozzle had no lip around the melt nozzle tip and had the longest protrusion tip length among previous melt delivery nozzles. At the gas pressures below of 2 MPa, the gas flow was on open-wake condition (Figure 60a). At the gas pressure of 2 MPa, the open-wake condition changed to the closed-wake condition and the Mach disk along with oblique shocks were appeared in front and around of the melt nozzle tip (Figure 60b).

The closed-wake condition was stable at the higher gas pressures of 2 MPa. The wake region in this nozzle was much smaller compared to that of other melt nozzles; moreover, the Mach disk was much closed to the melt tip. Table 4 shows the summery of WCP for nozzle set 2 with the choked gas die.

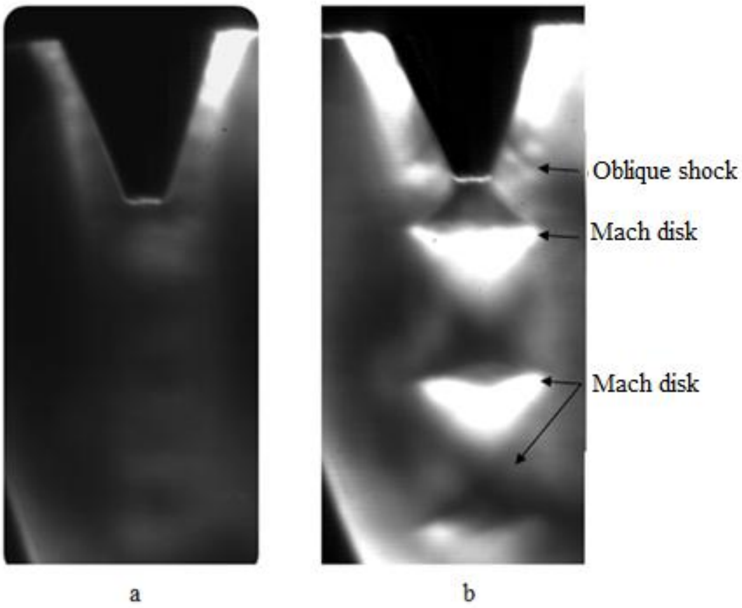

Figure 60. The Schlieren image of gas flow for nozzle type 7, a: open-wake condition at 1 MPa and b: closed-wake condition at 2 MPa.

Table 4. The WCP transition pressure for nozzle set 2 with a cylindrical choked gas die.

Nozzle type	WCP pressure (MPa)
Type5	3.5±0.5
Type 6	2.5±0.5
Type 7	2±0.5

5.3 The Schlieren images of gas flow for melt nozzle set 1 with C-D die

Similar experiments also were applied to the C-D gas die set-up with the melt nozzle set 1. The atomization gas pressure was also set between 1 to 5 MPa. Figure 61a shows the Schlieren image of type 1 at the gas pressure of 1 MPa. As can be seen in this situation, the gas jet exits the C-D gas die in the overexpanded form and some series of small diamond shocks appeared around the whole of circumference of the melt nozzle tip. These diamond shocks are also known as Mach diamonds or dancing diamonds and occur at overexpanded situation [82].

As stated in section 3-1-2-3, the ideal operating pressure for this C-D gas die is designed around 3 MPa; so, at the gas pressures above of 3±0.5 MPa; the gas flow pattern is expected to show underexpanded condition. Furthermore, about 2D downstream from the melt tip (D is the melt nozzle tip diameter) the Prandtl-Meyer waves can be seen at this atomization gas pressure. By increasing the gas pressures to 5 MPa (Figure 61b), the gas flow was still on underexpanded flow. Therefore, it seems that the gas wake at front of the melt nozzle tip showed the open-wake condition at over and underexpanded condition at gas pressures below of 5 MPa.

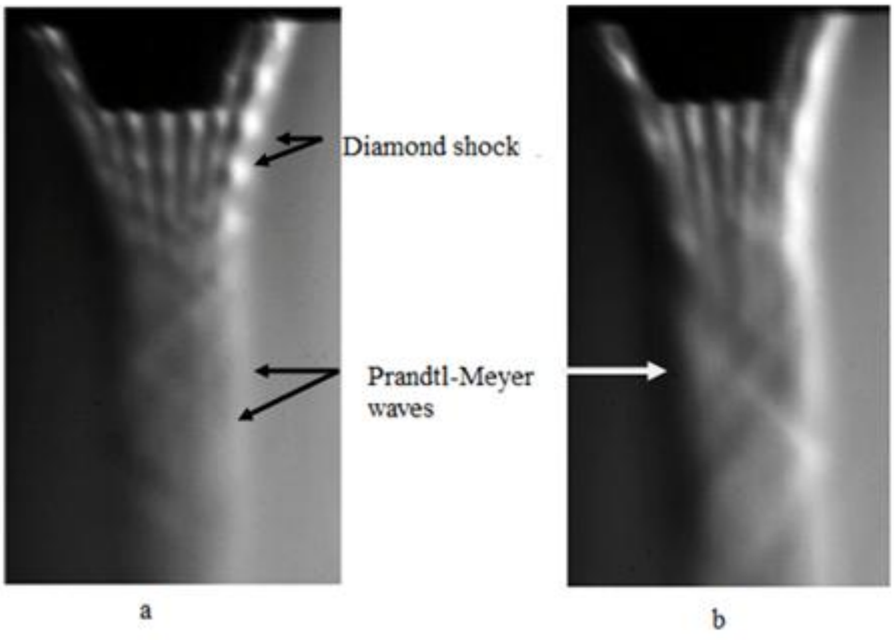

Figure 61. The Schlieren images of gas flow for nozzle type 1 at a: overexpanded condition and the gas pressure of 1 MPa and b: underexpanded condition and the gas pressure of 5 MPa.

Figure 62a shows the Schlieren image of gas flow field for nozzle type 2 at gas pressure of 1 MPa. Similar to the type 1, at overexpanded flow, the diamonds shocks emerged around the melt tip. In addition, the Prandtl-Meyer waves can be seen further downstream of melt tip. Increasing the inlet gas pressure to higher than 3 MPa, the flow showed underexpanded flow. This condition for type 2 is shown in figure 62b at the gas pressure of 5 MPa. It appears that the gas flow pattern for type 2 is similar to nozzle type 1 and showed the open-wake condition in gas pressures below of 5 MPa.

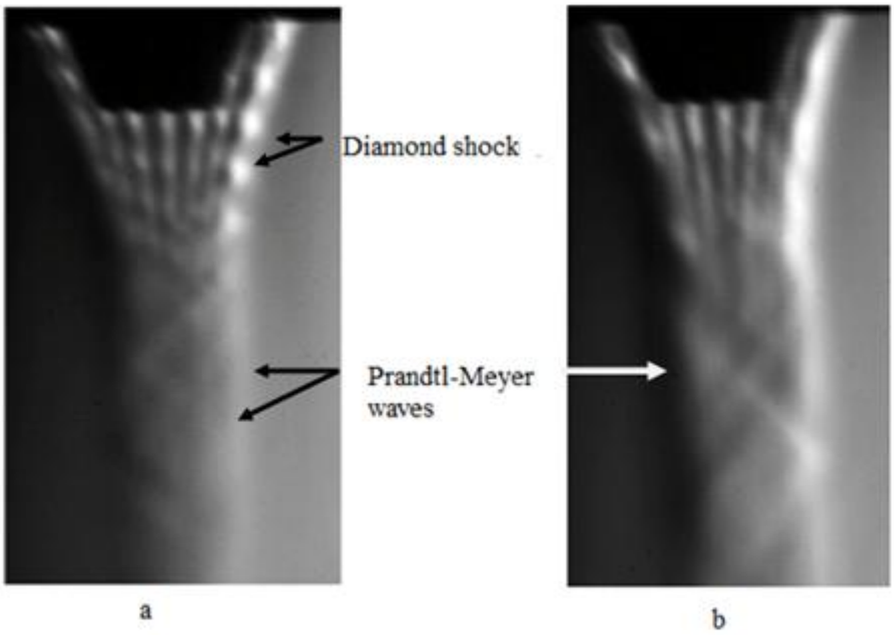

Figure 62. The Schlieren images of gas flow for nozzle type 2 at a: overexpanded condition and the gas pressure of 1 MPa and b: underexpanded condition and the gas pressure of 5 MPa.

For nozzles type 3 and 4, similar gas flow pattern of open-wake condition to type 1 and 2 were also observed at the gas pressures below of 5 MPa. The overexpanded to underexpanded gas flow and diamond shocks with Prandtl-Meyer waves in front of melt tip at two gas pressures of 1 and 5 MPa can be seen in figures 63 and 64.

Therefore, with the C-D gas die the gas wake condition was almost similar between nozzles at set 1.

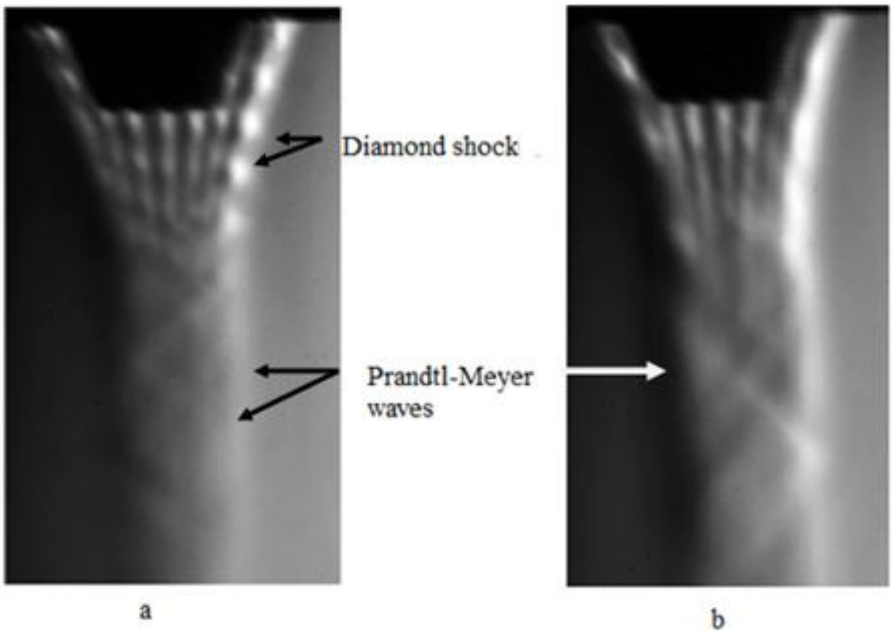

a b

Figure 63. The Schlieren images of gas flow for nozzle type 3 at a: overexpanded condition and the gas pressure of 1 MPa and b: underexpanded condition and the gas pressure of 5 MPa.

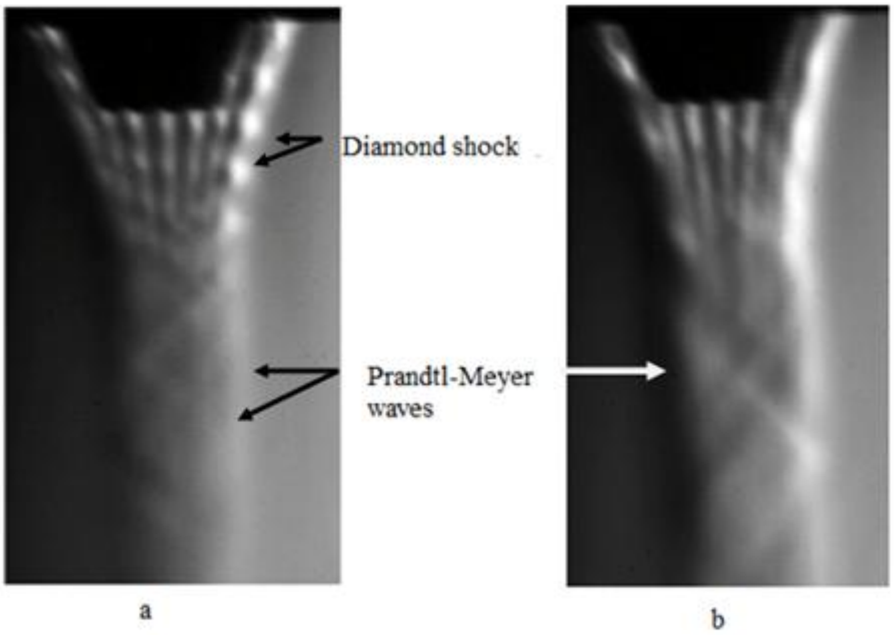

a b

Figure 64. The Schlieren images of gas flow for nozzle type 4 at a: overexpanded condition and the gas pressure of 1 MPa and b: underexpanded condition and the gas pressure of 5 MPa.

5.4 The Schlieren images of gas flow for melt nozzle set 2 with C-D gas die

Figure 65 shows the gas flow field in nozzle type 5 at the gas pressures of 1 and 5 MPa. In figure 65a, the diamond shocks and overexpanded gas flow with Pradntl-Meyer waves was observed around the melt nozzle tip. The underexpanded flow (Figure 65b) was also presented at the gas pressures above of 3 MPa. Similar to nozzle set 1 the gas wake condition showed the open-wake condition at atomization gas pressures below of 5 MPa.

Nozzle type 6 showed the similar gas flow pattern to type 5 (Figure 66 at the gas pressures of 1 and 5 MPa). Similar to previous nozzles, the overexpanded gas flow was seen at gas pressures below of 3 MPa (Figure 66a) and underexpanded flow was observed at the gas pressures above of 3 MPa (Figure 66b). Therefore, different internal nozzle tip design between type 5 and 6 had no significant influence on the gas wake condition.

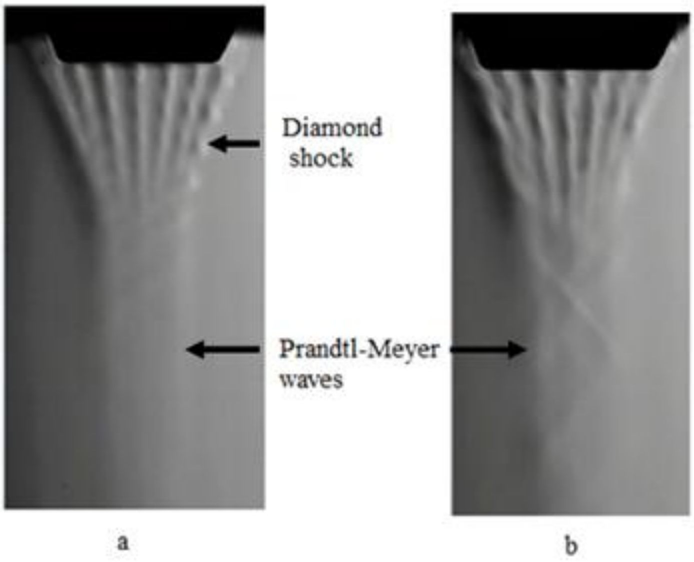

Figure 65. The Schlieren images of gas flow for nozzle type 5 at a: overexpanded condition and the gas pressure of 1 MPa and b: underexpanded condition and the gas pressure of 5 MPa.

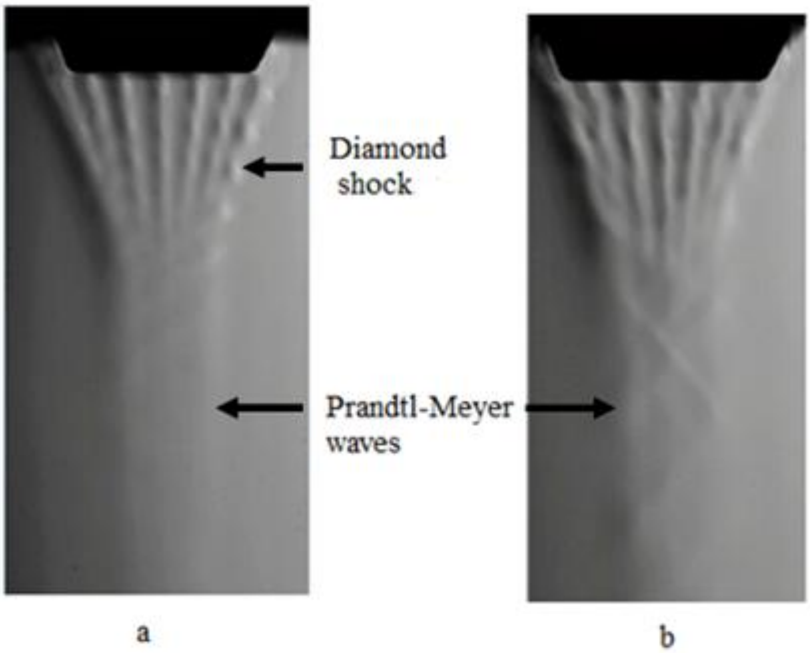

Figure 66. The Schlieren images of gas flow for nozzle type 6 at a: overexpanded condition and the gas pressure of 1 MPa and b: underexpanded condition and the gas pressure of 5 MP.

The same situation was also observed for the nozzle type 7 and the Schlieren images of overexpanded to underexpanded gas flow are shown in figure 67.

It can be found that changing the external or internal profile of the melt nozzle at the gas pressures below of 5 MPa had no major change in the gas wake condition and all melt nozzles showed the open-wake condition.

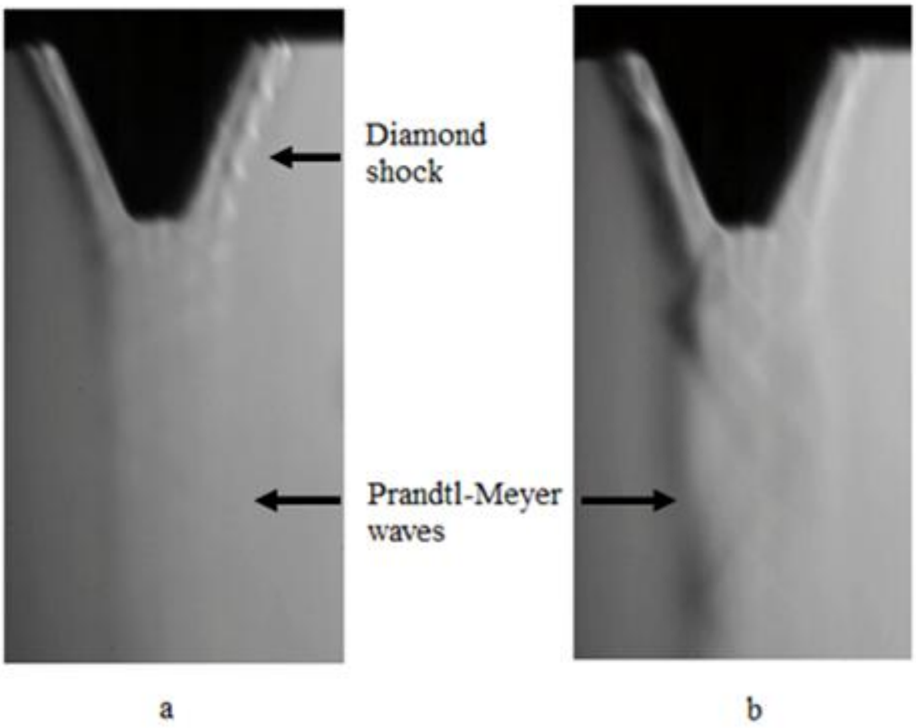

Figure 67. The Schlieren images of gas flow for nozzle type 7 at a: overexpanded condition and the gas pressure of 2 MPa and b: underexpanded condition and the gas pressure of 5 MP.

Based on these results, investigation of the Schlieren images of gas flow behaviour around the melt delivery nozzle could show different WCP and open to closed wake condition around the nozzle, but further understanding of how the melt delivery nozzle internal and external profile change the gas flow behaviour of open to closed-wake at different gas pressure needs another method of flow visualization technique. CFD modelling is a very useful technique to observe more details of the gas flow behaviour around the nozzle tip. Therefore, use of CFD methods to observer more detail of gas flow around the nozzle tip helps better understanding of why different WCP are obtained with changing melt tip and gas die profile

6 Numerical results

In this section, the preliminary numerical solutions are presented. This includes establishing results of the mesh independence study, domain independence study and study of sensitivity of the solution to different boundary conditions and different turbulence models. The numerical assumptions and boundary conditions were applied on nozzle type 1 with a cylindrical choked gas die at a fixed gas pressure of 1 MPa. The conclusions of this study were established and applied to the other melt nozzles with different gas die set–up in later work.

6.1 Primary CFD results

6.1.1 Mesh independence study

Figures 68 and 69 show the velocity magnitude of gas along the vertical lines AB and CD as outlined in figure 52. The velocity variation for mesh 2 (11000) was judged to be mesh independent as there was no change when the finer mesh (mesh 3) was used. Therefore, it was appropriate to use mesh 2 for numerical experiments.

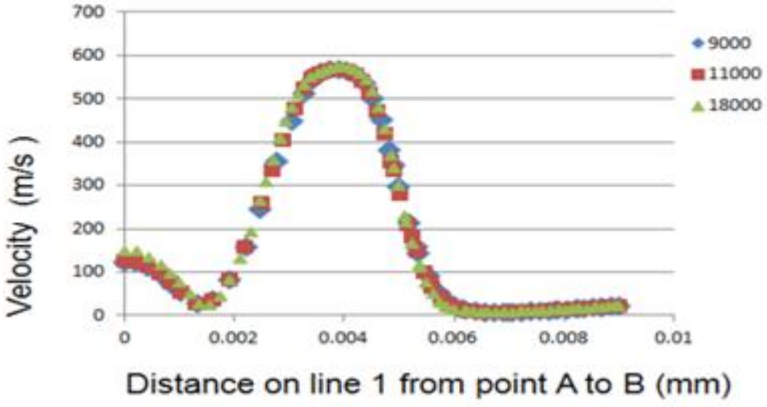

Figure 68. The velocity magnitude along line AB.

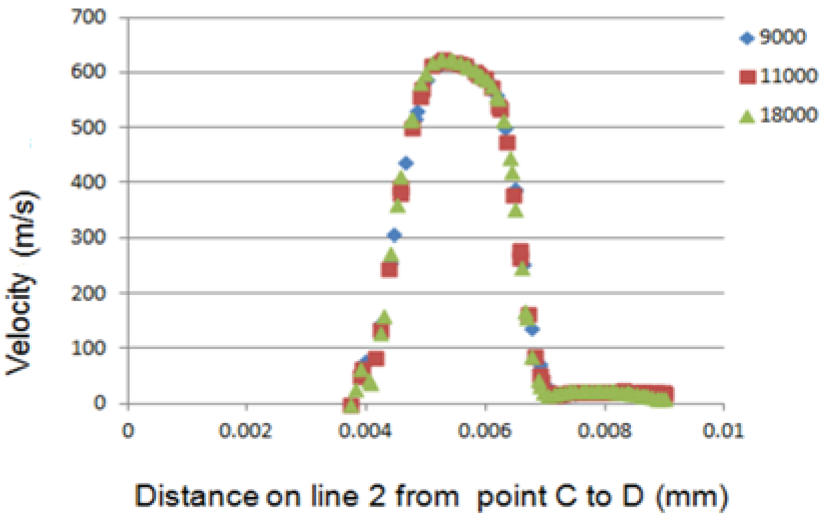

Figure 69. The velocity magnitude along line CD.

6.1.2 CFD sensitivity to turbulence model

Figure 70 and 71 illustrate the pressure and velocity contours of nozzle type 1 with cylindrical choked gas die at a gas pressure of 1 MPa. Two different turbulence models of *k*-ε-RNG and *k*-ω-SST were used at this condition. The solution was applied to the two models with the same boundary conditions and same mesh size.

According on these results, very little difference is observed between the two simulations with the gas flow field being very similar for both models. Similar results were seen in comparisons of when a range of other boundary conditions were applied. As such, in this case it was concluded that the results are shown to be relatively insensitive to the turbulence model applied. Therefore, the *k*-ω-SST model, which has been shown previously to be a reliable model for internal flows of this kind, has been chosen as turbulence model for the numerical solutions in all the studies.

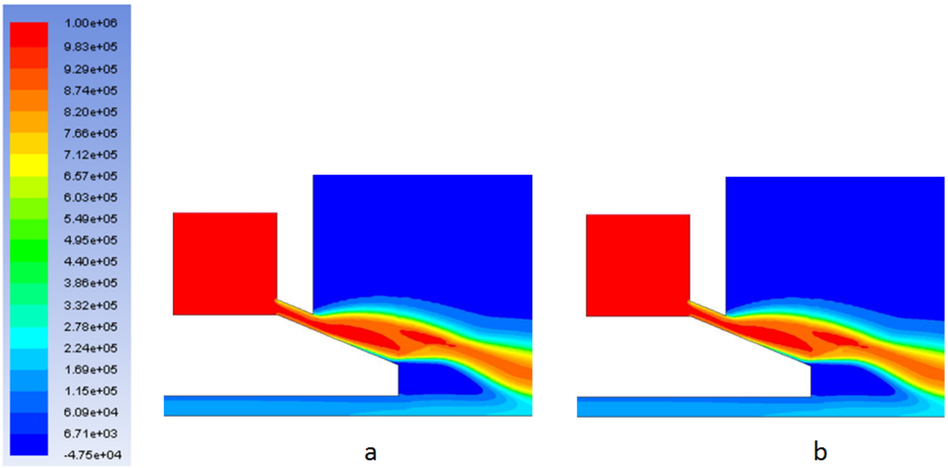

Figure 70. Pressure contour (Pa) of gas flow pattern around melt nozzle type 1 with a cylindrical choked gas jet at gas pressure of 1 MPa of gas flow pattern for a: *k*-ω-SST model and b: *k*-ε-RNG model.

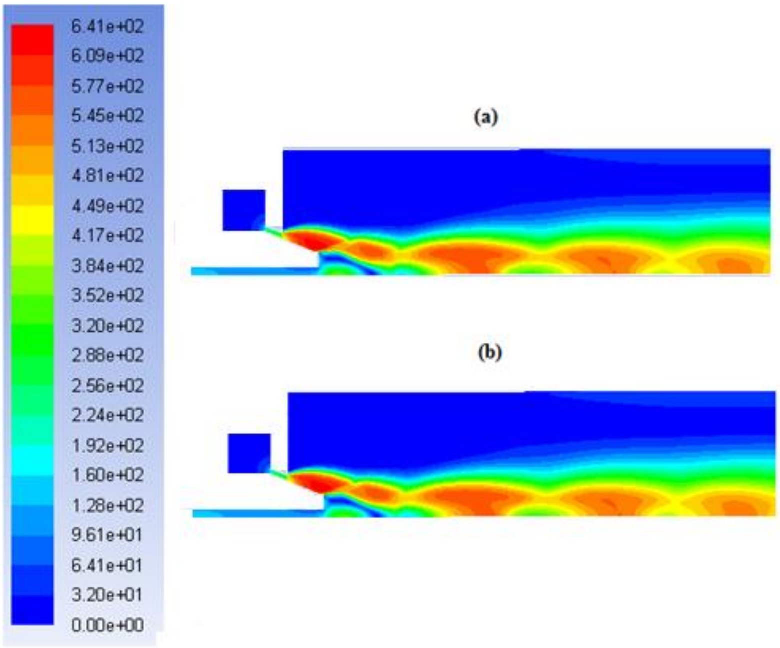

Figure 71. Velocity profile (m s^{-1}) of gas flow pattern for nozzle type 1 with a cylindrical choked gas jet at gas pressure of 1 MPa of gas flow pattern for a: *k*-ω-SST model and b: *k*-ε-RNG model.

6.1.3 CFD results for different boundary conditions on upper boundary condition

The velocity contour of nozzle type 1 for closed boundary or no-slip wall and atmospheric pressure condition at upper domain is shown in figure 72. The gas pressure was set at 1 MPa. In addition, the k-ω-SST turbulence model was used in both cases.

These results show that the gas velocity contours are similar in both cases. Based on these results and similar boundary conditions proposed in the literature [85, 86, 87], the closed boundary condition has been chosen for the rest of numerical tests.

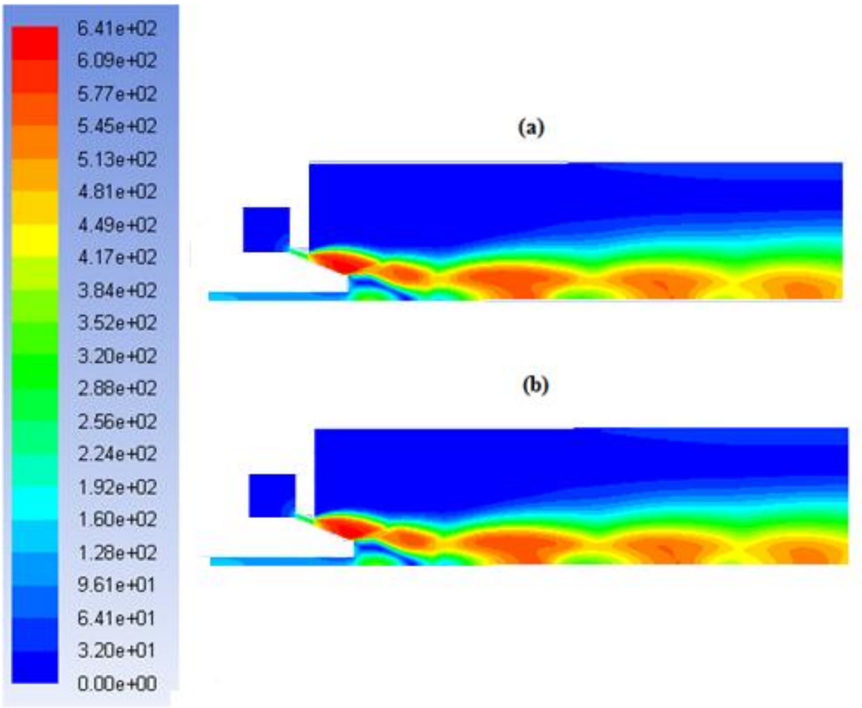

Figure 72. Velocity profile (m s^{-1}) of gas flow pattern for nozzle type 1 with a cylindrical choked gas jet at gas pressure of 1 MPa, a: closed boundary and b: open boundary condition.

6.1.4 CFD results of domain independence study at Z direction

The velocity contours of nozzle type 1 with the extended domain in the Z direction and normal domain are presented in figure 73. Increasing the numerical domain in the Z direction shows additional gas flow expansion downstream in front of melt nozzle tip, but no changes to the flow profile when comparing the same regions. This indicates the outlet boundary condition is not having an impact on the flow field. In this thesis, the investigation is focused on the gas flow behaviour closer to the melt tip where the primary break-up may occur so, the numerical domain with normal extension in Z direction has been selected for the rest of numerical tests.

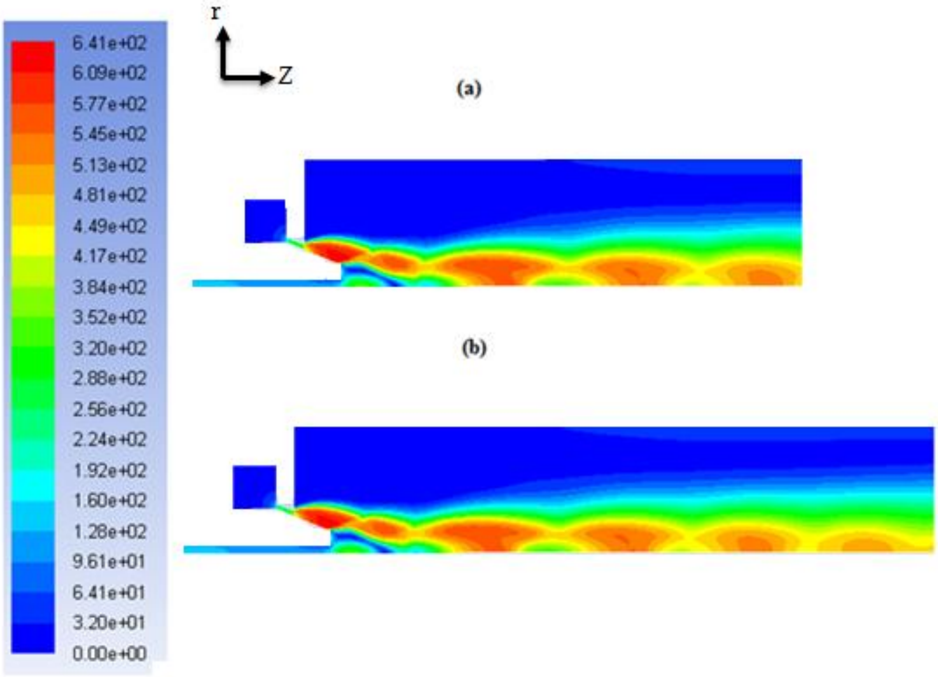

Figure 73. Velocity profile (m s^{-1}) of gas flow pattern for nozzle type 1 with a cylindrical choked gas jet at gas pressure of 1 MPa, a: normal domain and b: extended domain on Z direction.

6.1.5 CFD results of domain independence study in r direction

The velocity contour of nozzle type 1 with an extended domain in the r direction is shown in figure 74. As can be seen in this figure, the gas flow pattern is similar in both solutions with gas expanding after leaving the gas jet. The gas flows from the melt nozzle tip down the centre of the chamber (alongside the symmetry line) with the dark blue area at the top of the domain showing the zero velocity in this region. As can be seen, the extended domain in the r direction has no noticeable effect on the solution and the dark blue area. Thus, for this study the normal numerical domain has been selected.

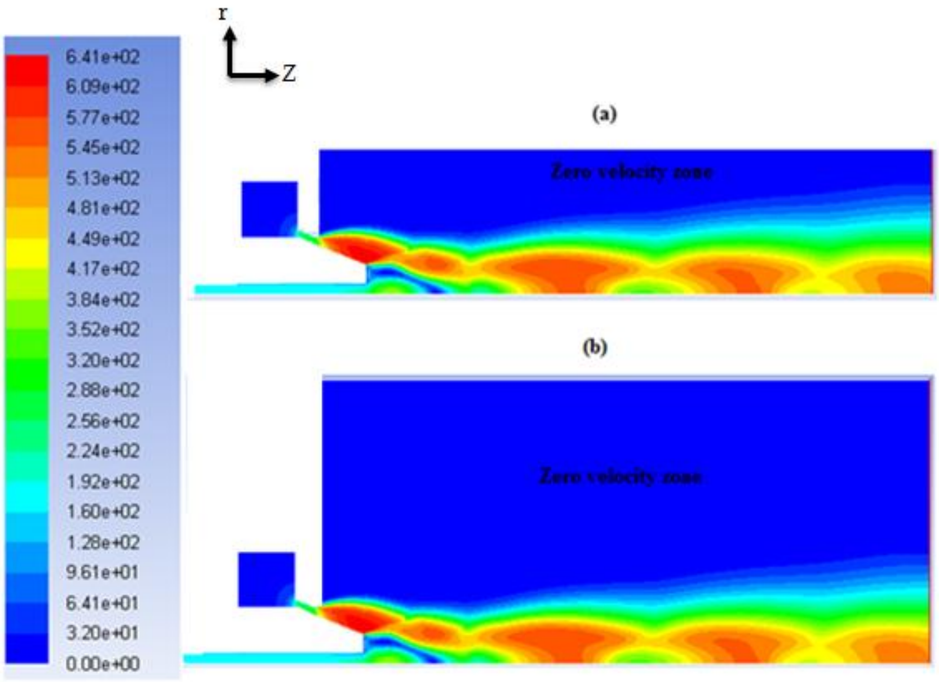

Figure 74. Velocity profile (m s^{-1}) of gas flow pattern for nozzle type 1 with a cylindrical choked gas jet at gas pressure of 1 MPa, a: normal domain and b: extended domain on r direction.

6.1.6 CFD results with different boundary condition with and without gas chamber

The velocity contours of the gas flow field for nozzle type 1 at a gas pressure of 1 MPa for a normal domain with and without gas chamber is presented in figure 75. The gas velocity contours for both domains are similar throughout the numerical domain. The total pressure graphs along the two lines of AB and CD at the gas die input boundary condition (Figures 76 and 77) show small differences in pressure change along these lines. It is believed that the results from the numerical domain with a gas chamber are more similar to the experimental gas die system where there is a gas chamber before the gas die entrance. Therefore, according to these results the model with a gas chamber was selected for rest of the tests.

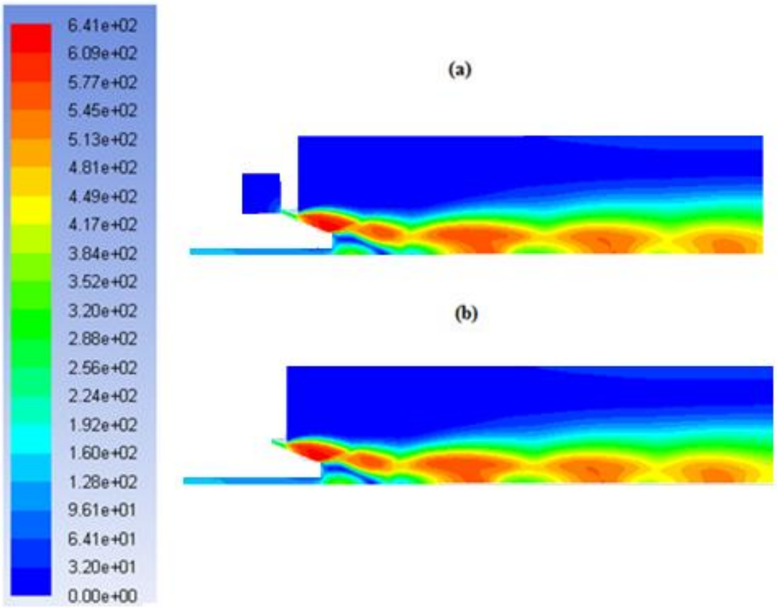

Figure 75. Velocity contour (m s^{-1}) of gas flow pattern for nozzle type 1 with cylindrical choked gas jet at gas pressure of 1 MPa, a: Normal domain with a gas chamber, b: Normal domain without chamber.

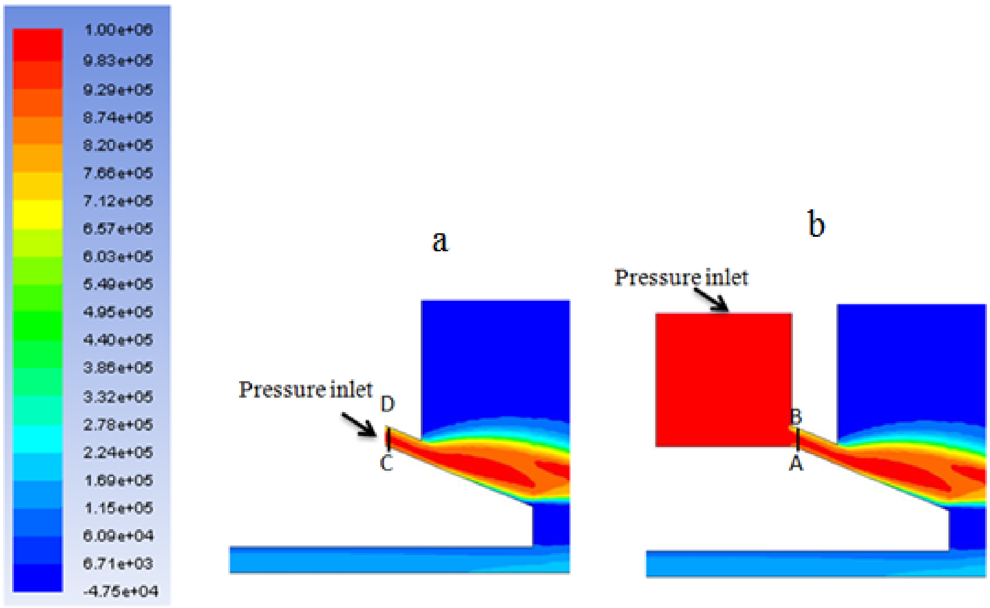

Figure 76: Figure 76. Pressure contour (Pa) of gas flow pattern for nozzle type 1 with a cylindrical choked gas jet at gas pressure of 1 MPa, a: Normal domain without gas chamber, b: Normal domain with chamber.

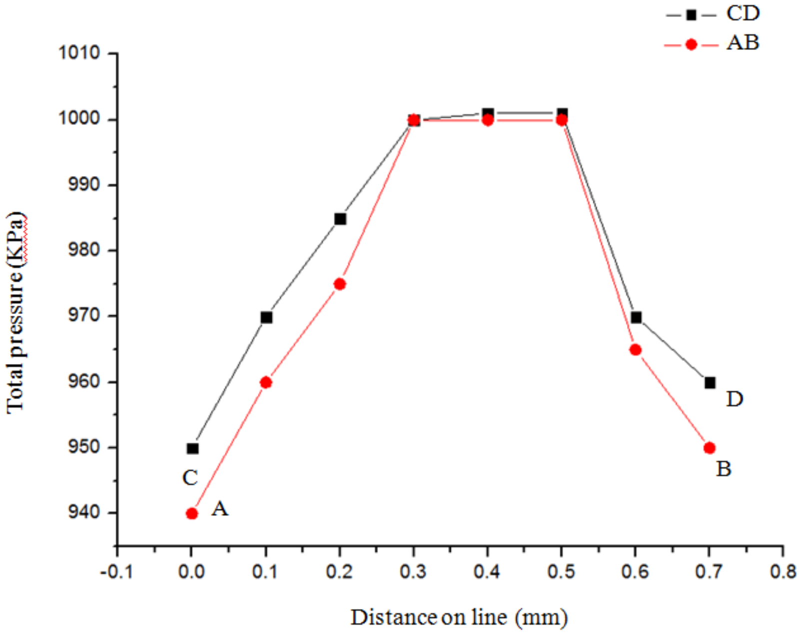

Figure 77. Pressure variation against distance on two lines of AB and CD.

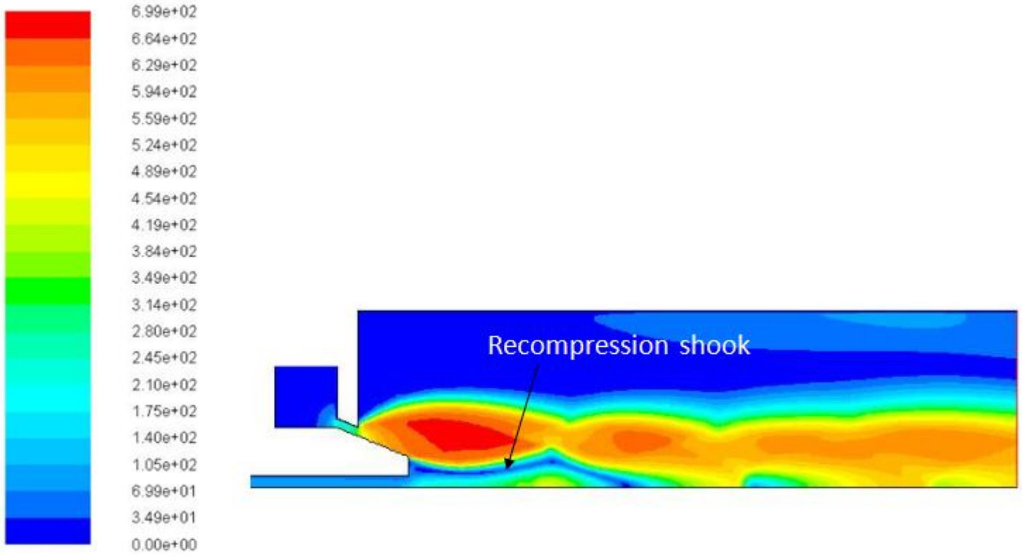

Figure 78. The gas flow velocity (m/s) of nozzle type 1 at gas pressure of 3 MPa.

In addition, The corresponding of the velocity, total temperature, total pressure, axial velocity and Mach number of nozzle type 1 with a gas chamber at gas pressure of 3 MPa show in figure 78 and 79. The results shown here demonstrate the fluctuations of velocity; temperature, pressure and the Mach number just after the gas die exit jet and front of melt delivery nozzle area. In addition, since the exited gas pressure decreases to a nearly atmospheric pressure, the computed velocity contour shows the recompression shocks around melt nozzle while the axial velocity shows the different velocity magnitude and its direction throughout the domain at Z direction. The fluctuation of total temperature is about 271 to 303 K throughout the domain.

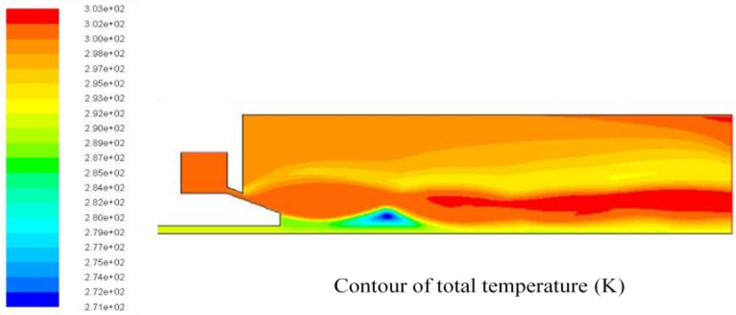

Contour of total temperature (K)

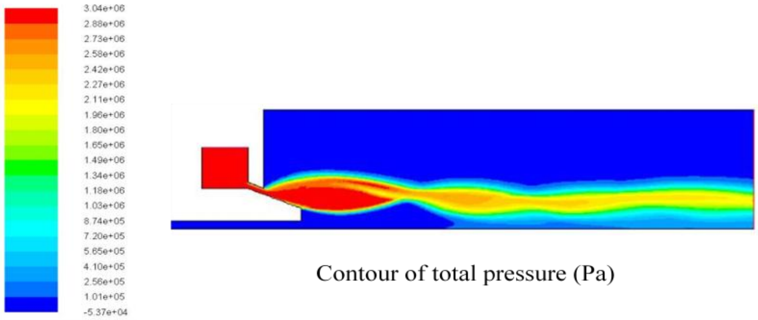

Contour of total pressure (Pa)

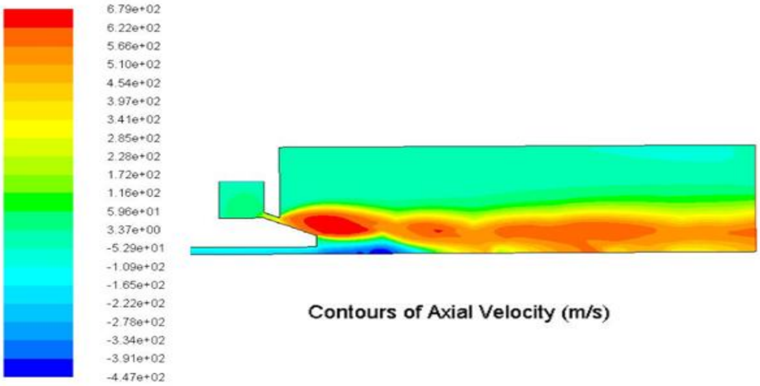

Contours of Axial Velocity (m/s)

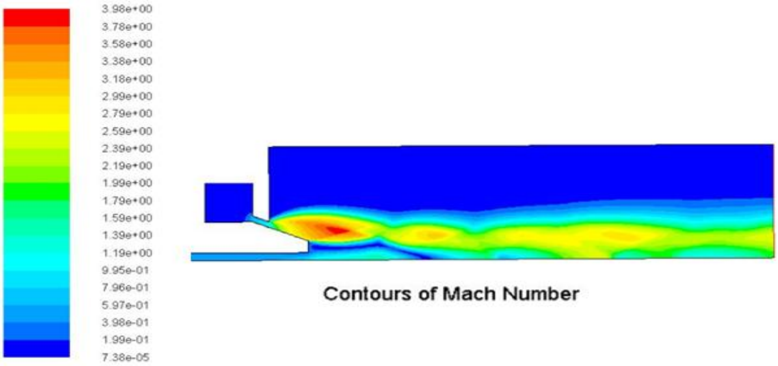

Contours of Mach Number

Figure 79. The total temperature, total pressure, Axial velocity and Mach number of nozzle type 1 at gas pressure of 3 MPa.

6.2 CFD results for gas flow investigation

6.2.1 CFD results of nozzle set 1 and cylindrical choked die

In these series of numerical tests, the effect of changing the internal profile of melt nozzle on the gas flow field is investigated.

The velocity contours for different melt nozzles in nozzle set 1 at an atomization gas pressure of 1 MPa with cylindrical choked gas die are given in figure 78. For nozzle type 1 with the flat head tip, the high velocity gas flow was expanded rapidly as soon as the gas left the cylindrical gas die. At this pressure, the gas is in the open-wake condition.

It should be noted that, the main distinguishing criterion of an open and closed-wake condition in the CFD results is appearance of Mach disk at the front of the melt nozzle tip. This creates two recirculation zones (Figures 80 and 81). One between melt tip and Mach disk and other at front of Mach disk. This condition was applied consistently for judgment between open to closed-wake condition for all of CFD results.

The same situation of open-wake condition was also seen for all of the type 2, 3 and 4 at the atomization gas pressure of 1 MPa. Furthermore, the recirculation zone was observed in front of all four nozzles. In addition, as the gas expanded rapidly while exiting the gas die, some oblique shocks were formed around the melt nozzle tip. The difference between the velocity of the supersonic gas jet flow and the subsonic flow inside the recirculation flow causes a rapid change in the flow direction and oblique shocks will form [86].

For nozzle type 1, the oblique shocks forms around the melt nozzle tip, which slows down the gas flow velocity in order to match the surrounding atmospheric pressure. Then, again the gas velocity accelerates and then decelerates to a subsonic situation, which produces the series of Prandtl-Meyer waves along the central axis-symmetry line. This flow field was also observed for nozzle type 2. Nozzles type 3 and 4 had almost the same situation at a gas pressure of 1 MPa and all of the three nozzles had almost the same gas flow pattern to the nozzle type 1.

In nozzle type 1 at a gas pressure of 2.75 MPa (Figure 80), the gas flow has expanded further downstream of the melt delivery tip. Throughout the series of expansion waves, the recirculation zone has expanded further in front of the melt nozzle tip. At this condition, the gas wake in front of the melt nozzle tip was still in open-wake condition. A similar situation was also observed for nozzle types 2 and 3 at this pressure. In nozzle type 4 the internal shocks made a Mach disk at the symmetry line; and a closed-wake condition was observed in this situation. In nozzle type 4, the transition pressure between open to closed-wake condition (WCP) was measured at 2.75 MPa.

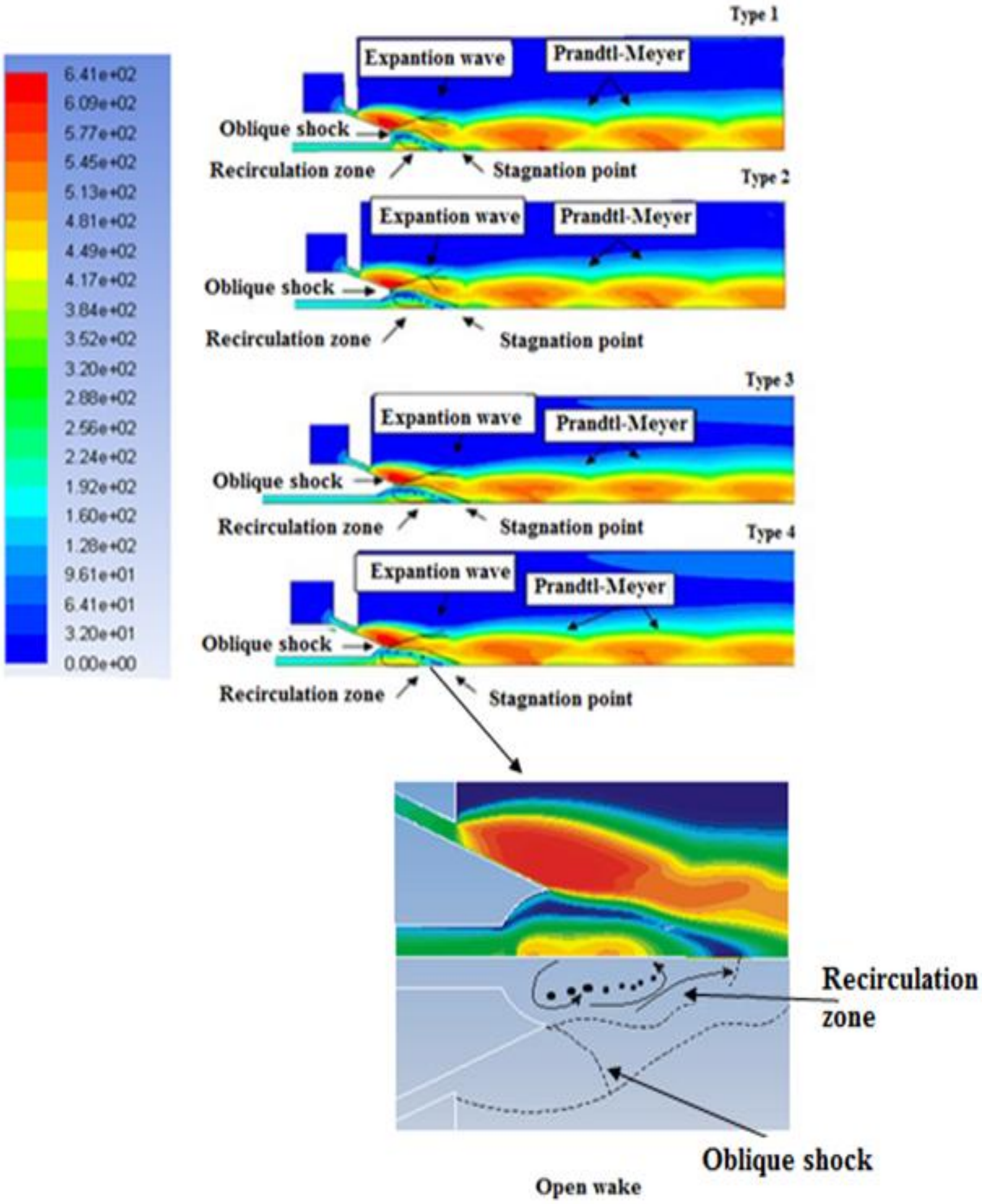

Figure 80. Velocity contour (m s^{-1}) for nozzle set 1 at atomization gas pressure of 1 MPa and open wake close-up.

Figure 81 shows the Mach disk in nozzle type 4 at the pressure of 2.75 MPa. In this pressure, the recirculation zone was also truncated and had the smallest recirculation zone length. The Mach disk was also reported by Anderson et al. [82] at CFD modelling of a single-phase gas flow with a cylindrical gas die at closed-wake condition [82]. The recirculation zone for nozzle type 4 was truncated and two recirculation zones have emerged in this region. One in front of the melt nozzle tip and the other is located at front of the Mach disk (Figure 81).

In addition, for validating the CFD results, the position of Mach disk in the Schlieren image of nozzles type 4 and 7 was compared to Mach disk position of this nozzle in CFD result at the same inlet gas pressure (Figure 82). This also can be a good sign for qualitatively validating the numerical results.

At an atomization gas pressure of 3.25 MPa, in nozzles type 1 and 2, the gas flow pattern was still in an open-wake condition. However, for nozzle type 3 the Mach disk was formed in this pressure and the gas wake was transformed from open to closed-wake. (The velocity contour is not presented). The WCP in nozzle type 3 was 3.25 MPa. This condition is similar to that observed in nozzle type 4 with two recirculation zones.

Figure 83 illustrates the velocity contours for these nozzles at a gas pressure of 4.75 MPa. Nozzles type 1 and 2 now show a closed-wake condition and the Mach disk appeared in front of melt nozzle tip for both of these nozzles. The WCP between the open and closed-wake condition for these two nozzles was measured at 4.75 MPa. A similar situation was also observed at the higher atomization gas pressure of 4.75 MPa for nozzles type1 and 2 at the closed-wake condition. The WCP for these two nozzles was observed at 4.75 MPa. The summary of WCP for nozzle set one is presented at table 5.

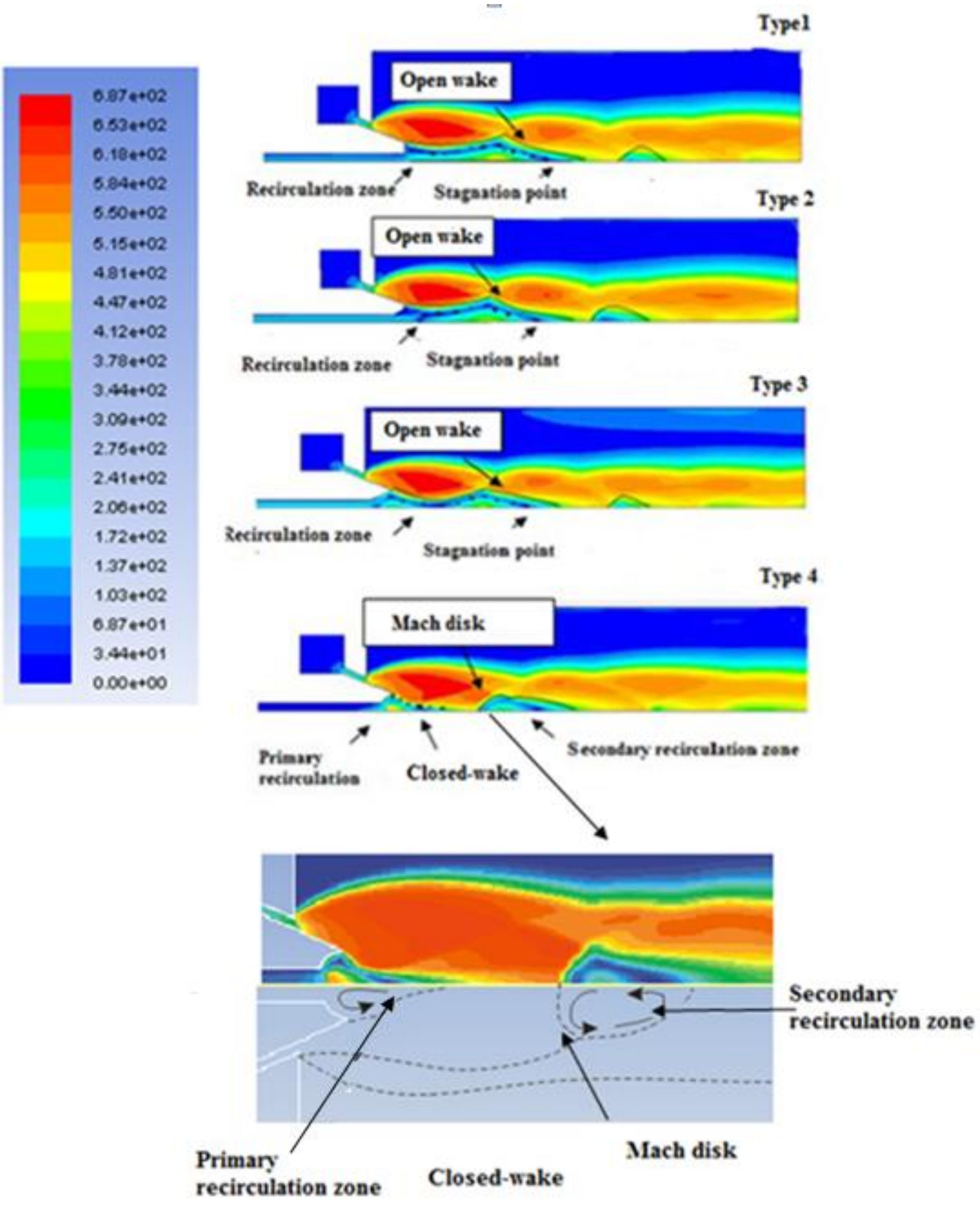

Figure 81. Velocity contour (m s^{-1}) for nozzle set 1 at atomization gas pressure of 2.75 MPa and the closed-wake close–up for nozzle type 4.

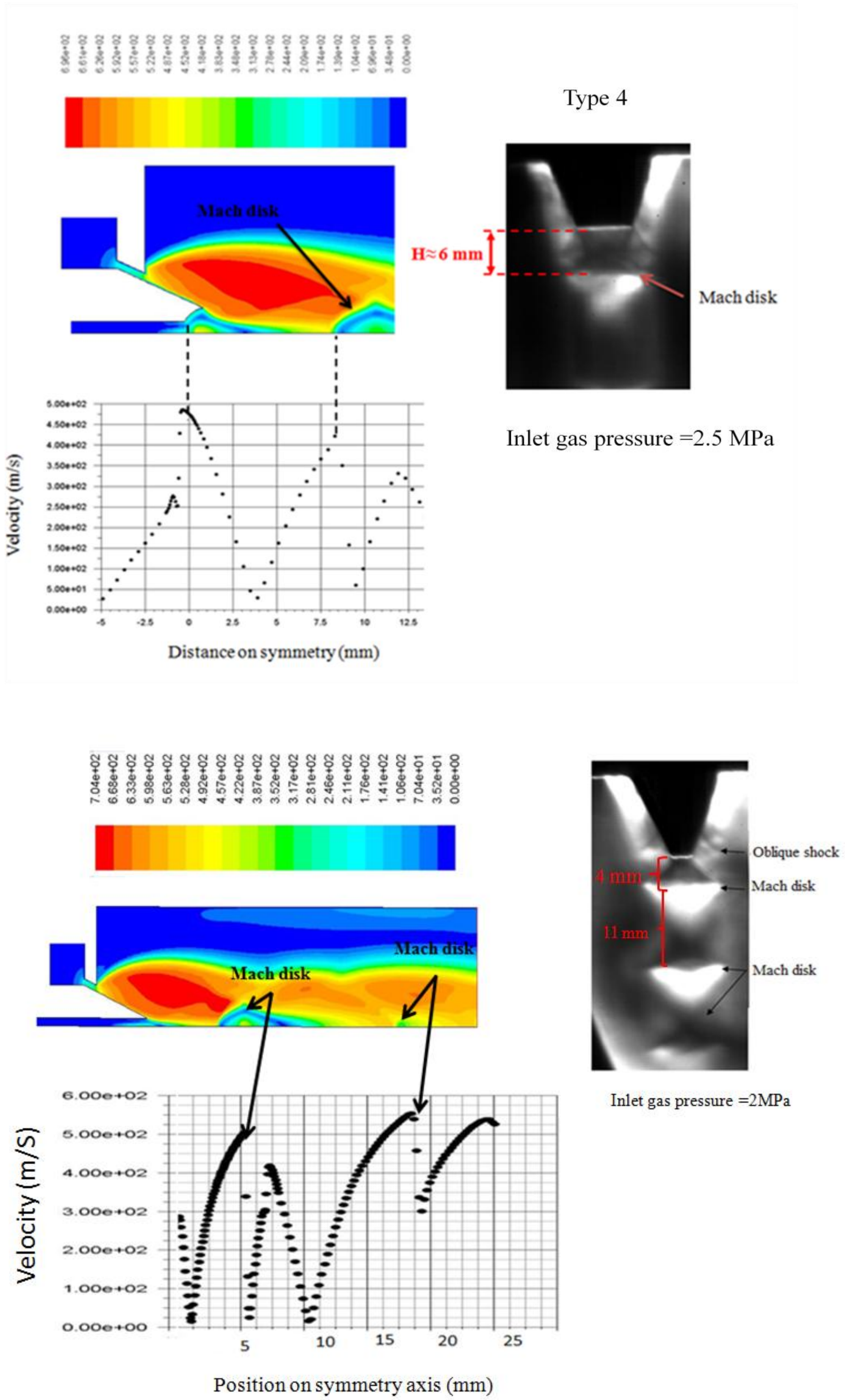

Figure 82. The velocity contour and Mach disk position comparison between CFD and Schlieren of nozzles type 4 and 7 at closed-wake condition.

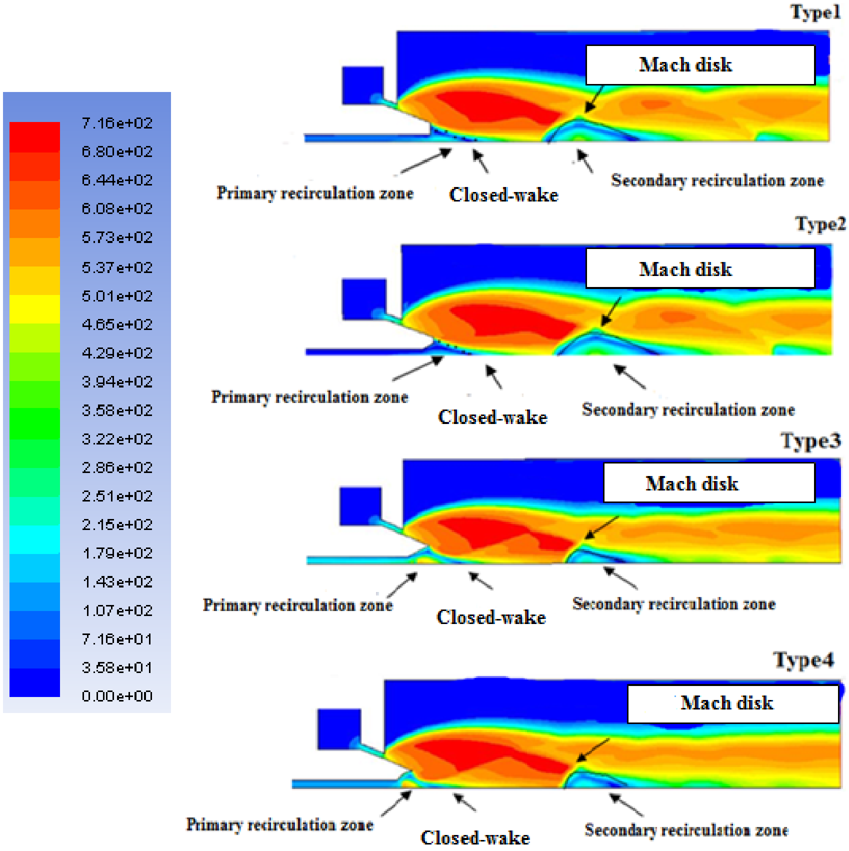

Figure 83. Velocity contour (m s^{-1}) for nozzle set 1 and close-wake condition at atomization gas pressure of 4.75 MPa.

Table 5. The WCP transition pressure at numerical and experimental tests for nozzle set 1 with a cylindrical choked gas die.

Nozzle type	WCP at numerical result (MPa)	WCP at experimental result (MPa)
Type 1	4.75	4.5±0.5
Type 2	4.75	4.5±0.5
Type 3	3.25	3.5±0.5
Type 4	2.75	3±0.5

6.2.2 CFD results for nozzle set 2 with the cylindrical choked gas die

Figure 84 shows the velocity contours for melt nozzle set 2 at a gas atomization of 1 MPa. Similar to the nozzle set 1, at this pressure, the gas jet expanded rapidly at the gas exit jet area. Again, the oblique shocks and recirculation zone can be seen around each melt nozzle tip. Further downstream of the melt tip, the subsonic gas jet made a series of Prandtl- Meyer waves in the front of each melt nozzle. In addition, at this pressure all of melt nozzles in set 2 are in open-wake condition.

Increasing the gas pressure to 2 MPa; the recirculation zone and internal shocks expand further at front of each of melt tip. At this pressure, the open-wake condition is still stable at front of the nozzle set 2.

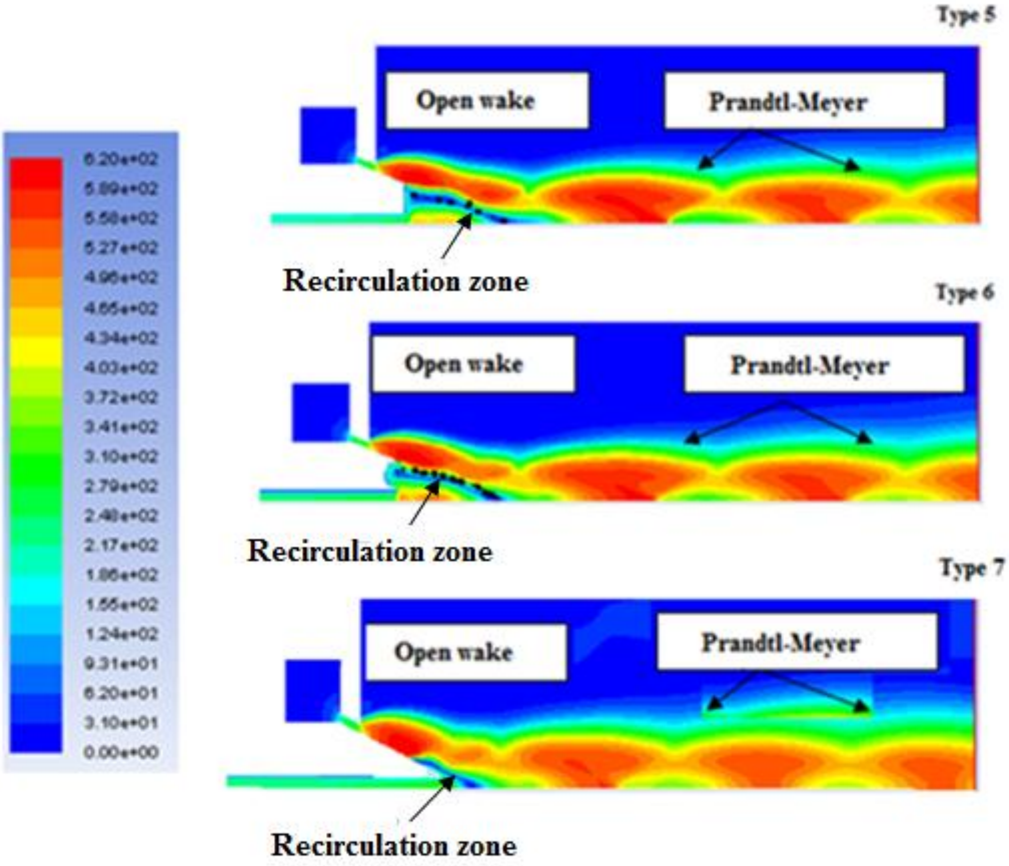

Figure 84. Velocity contour (m s^{-1}) for nozzle set 2 and choked die at atomization gas pressure of 1 MPa.

At a gas pressure of 2 MPa (Figure 85), the recirculation zone has expanded further and the open-wake condition still is observed in the melt nozzles type 5 and 6. In type 7 and the gas pressure of 2 MPa, a small secondary recirculation zone appears in front of the primary recirculation zone for this nozzle, which indicates the formation of Mach disk and the closed-wake condition.

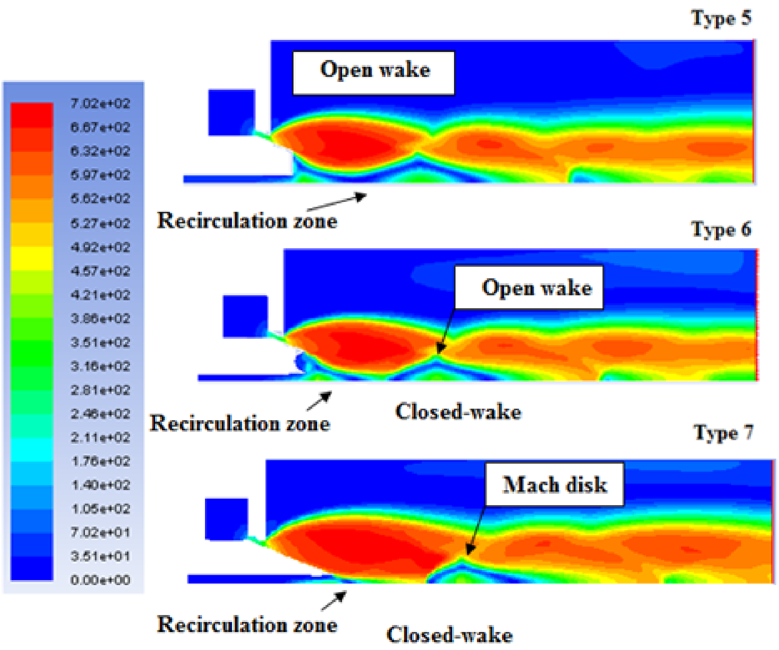

Figure 85. Velocity contour (m s^{-1}) for nozzle set 2 and choked die at atomization gas pressure of 2 MPa.

At the gas pressure of 2.5 MPa, type 6 showed the closed-wake condition, but type 5 was still in open-wake. (Figure is not presented).

Figure 86 illustrates the velocity contours of these three nozzles at a gas pressure of 3.45 MPa. At this pressure, nozzle type 5 showed the closed-wake condition and Mach disk in front of melt nozzle tip. The transition pressure for open to closed-wake condition for nozzle type 5 was 3.45 MPa and for nozzle type 6 was measured at 2.5 MPa. Table 6 shows the summery of WCP for nozzle set 2.

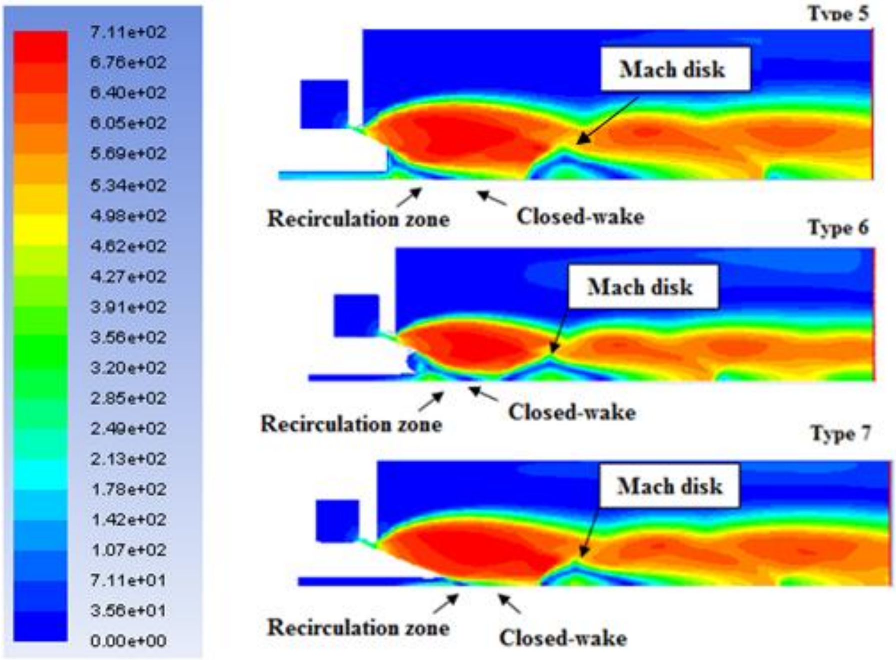

Figure 86. Velocity contour (m s^{-1}) for nozzle set 2 and choked die at atomization gas pressure of 3.45 MPa.

Table 6. The WCP transition pressure at numerical and experimental tests for nozzle set 2 with a cylindrical choked gas die.

Nozzle type	WCP at numerical result (MPa)	WCP at experimental result (MPa)
Type 5	3.45	3.5±0.5
Type 6	2.5	2.5±0.5
Type 7	2	2±0.5

6.2.3 CFD results for nozzle set 1 with the C-D gas die set up

The velocity contours for the C-D gas die design for nozzle set 1 at a gas pressure of 1 MPa is depicted in figure 87. At this pressure, the gas jet flow is over-expanded and a series of diamond shocks formed around and front of the melt delivery nozzle. In this condition, the gas wake in front of the melt tip was in open-wake condition. In addition, the series of Prandtl-Meyer waves formed further down at the front of all melt nozzle tips. This condition was also observed at the gas pressures of 2 MPa.

The underexpanded gas flow condition and a series of Prandtl-Meyer waves observed at the gas pressures above of 4 MPa for all nozzles in set 1. At this pressure, the recirculation zone expanded further in front of melt tip and open-wake condition was still stable. Similar to the experimental test, no significant change was seen to the gas wake condition for any of the melt nozzle set with different internal profile design.

The underexpanded and open-wake condition for each of melt nozzles was also observed at the gas pressure of 5 MPa. Figure 88 depicts this condition. Thus, unlike cylindrical gas die system, which the gas flow pattern was highly affected by changing the internal profile of nozzle tip, the gas flow pattern with the C-D gas die system did not show noticeable change in the gas flow for each of nozzle and the open-wake condition was observed in all of melt nozzles. Ting et al. [10] also observed the open-wake condition during experimental test of a HPGA-III gas die at the atomization gas pressures below of 4.95 MPa.

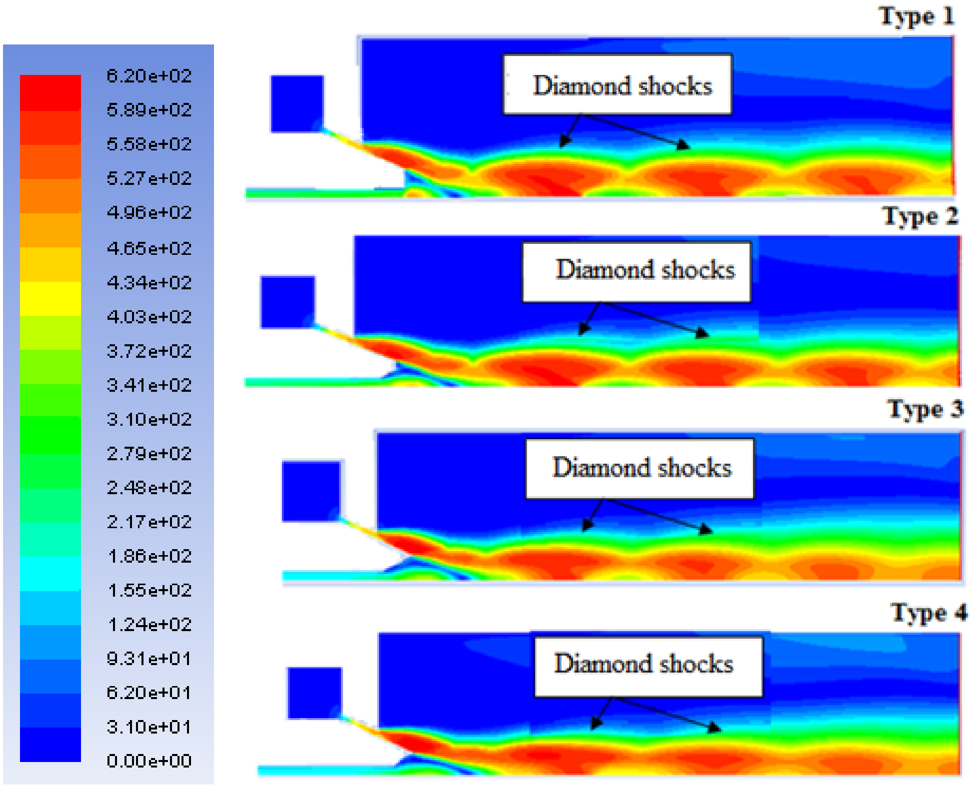

Figure 87. Velocity contour (m s^{-1}) for nozzle set 1 with the C-D gas die and open-wake condition at atomization gas pressure of 1 MPa.

Therefore, it seems that increasing the gas pressure above of 5 MPa can affect the wake condition during use of C-D gas die set-up. Increasing the atomization gas pressure beyond of 5 MPa during experimental test was not possible due to limitation of gas regulator and safety instructions. Therefore, the higher gas pressure tests, just applied on the numerical experiment for nozzles set 1 and 2.

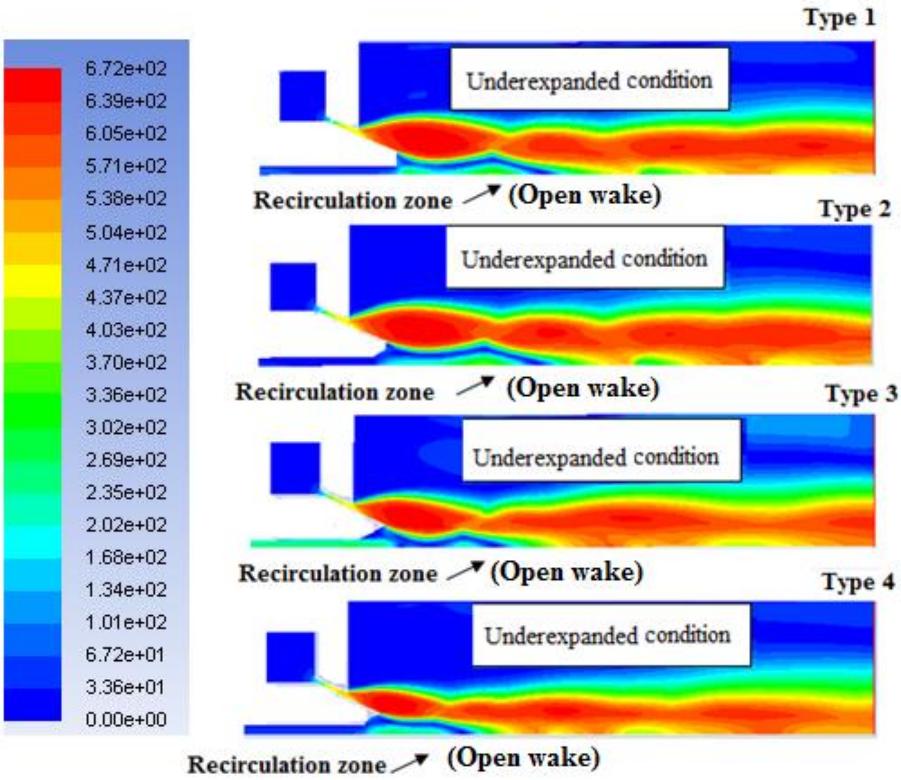

Figure 88. Velocity contour (m s^{-1}) for nozzle set 1 with the C-D gas die and open-wake condition at atomization gas pressure of 5 MPa.

Figure 89 shows the closed-wake condition for nozzle set 1 at the WCP of each nozzle. For nozzles type 1and 2 the closed-wake condition and Mach disk at underexpanded situation occurred at around 5.30 MPa while for nozzles type 3 and 4 it happened at 5.15 and 5.10 MPa, respectively. It seems that similar to the previous choked die, the closed-wake condition occurred for nozzles type 1 and 2 at a higher gas pressure compared to nozzles type 3 and 4. Table 7 shows the summery of WCP for nozzle set 1.

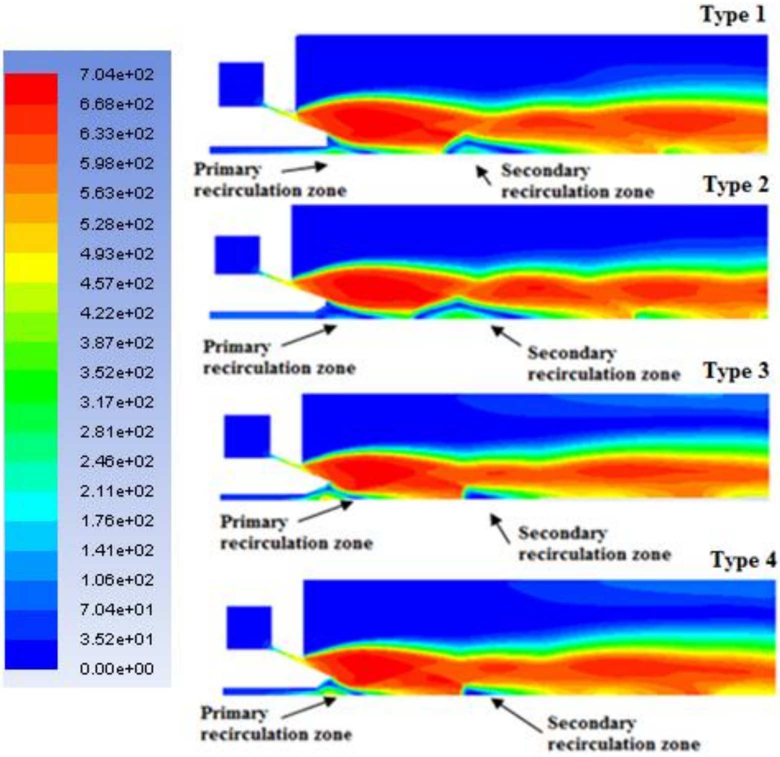

Figure 89. Velocity contour (m s^{-1}) for nozzle set 1 with the C-D gas die and closed-wake at underexpanded condition at WCP of each melt nozzle.

Table 7. The WCP transition pressure for nozzle set 1 with the C-D gas die.

Nozzle type	WCP (MPa)
Type 1	5.3
Type 2	5.3
Type 3	5.15
Type 4	5.10

6.2.4 Numerical results for nozzle set 2 with the C-D gas die design

The same test with the C-D die was also applied for melt nozzles type 5, 6 and 7. The velocity contours for nozzle set 2 at a gas pressure of 1 and 5 MPa are shown in figures 90 and 91, respectively. The overexpanded flow for the gas pressures below of 3 MPa and under-expanded gas flow condition at higher gas pressures of 3 MPa with the open-wake condition is obvious in these figures. Similar to previous results of nozzle set1 with the C-D die, melt tip geometry shows no significant impact on the wake condition.

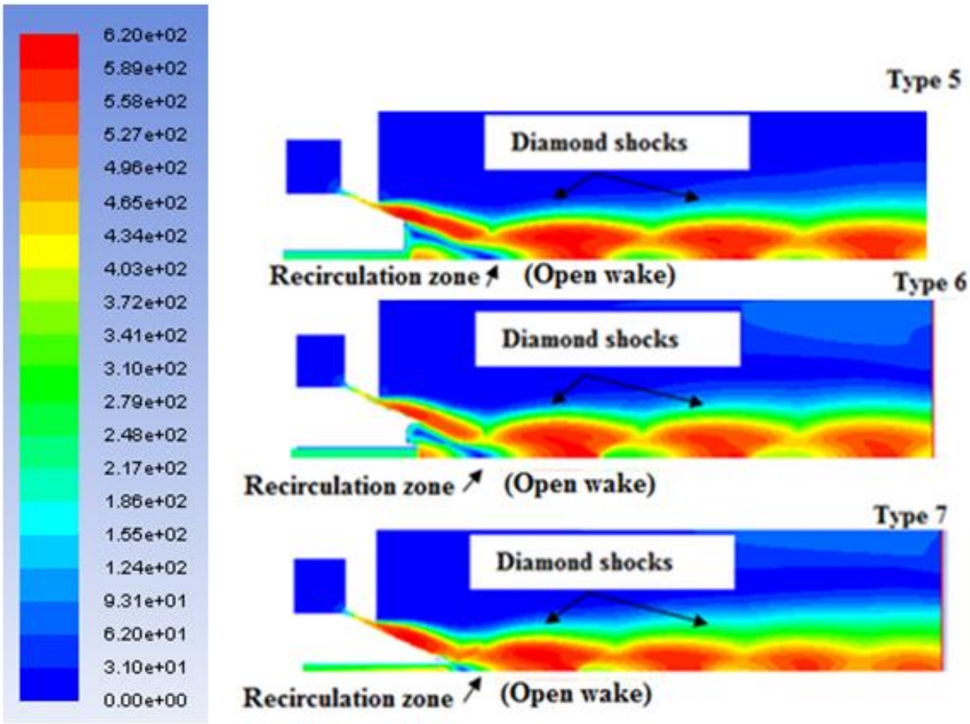

Figure 90. Velocity contour (m s^{-1}) for nozzle set 2 with the C-D gas die and open-wake condition at atomization gas pressure of 1 MPa.

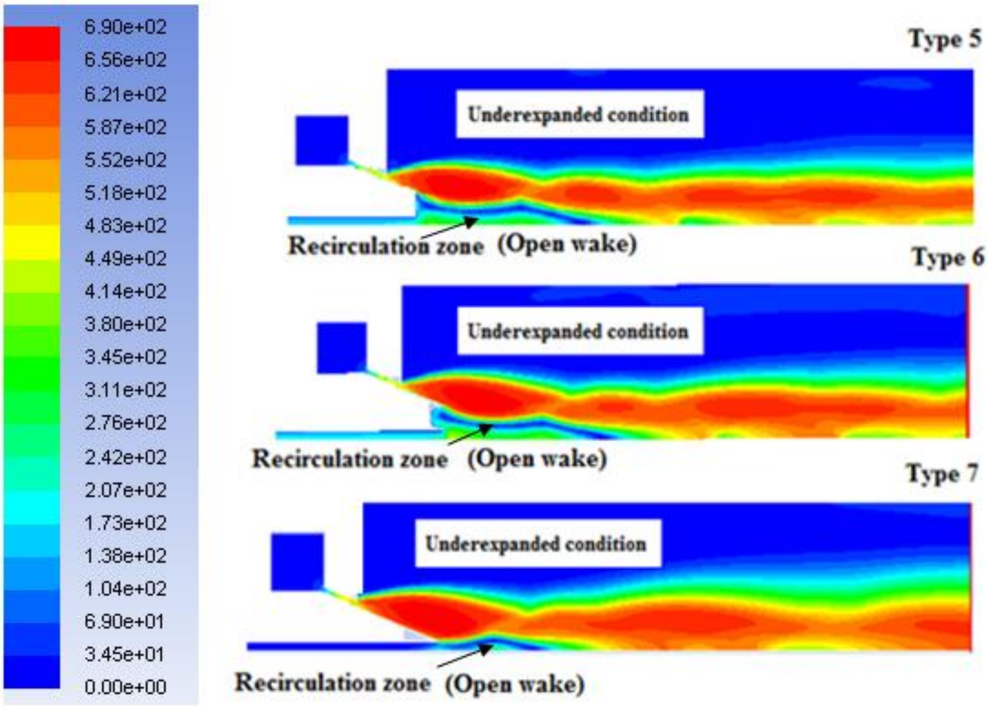

Figure 91. Velocity contour (m s^{-1}) for nozzle set 2 with the C-D gas die and open-wake condition at atomization gas pressure of 5 MPa.

Increasing the gas pressure to 5.25 MPa shows the closed-wake at under expanded condition for nozzle type 5 (Figure 92) and for types 6 and 7 at pressure of 5.15 and 5.10 MPa, respectively (Figure 92). Table 8 shows the WCP for nozzle set 2 at this condition.

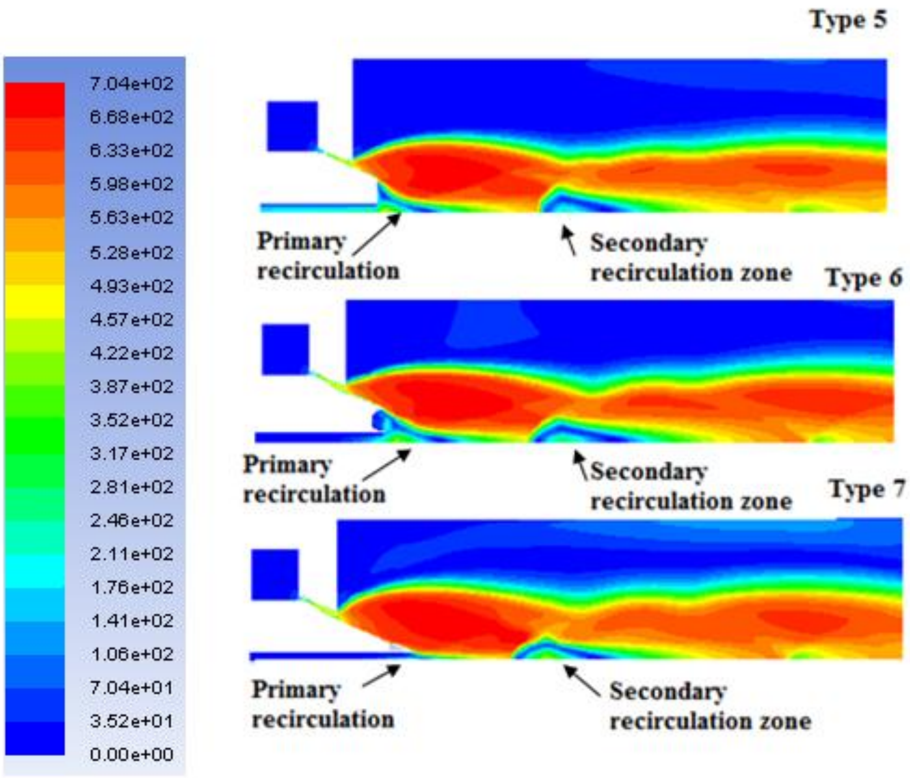

Figure 91. Velocity contour (m s^{-1}) of closed-wake condition for nozzle set 2 with the C-D gas die at WCP of each nozzle and underexpanded condition.

Table 8. The WCP transition pressure for nozzle set 2 with the C-D gas die.

Nozzle type	WCP (MPa)
Type 5	5.25
Type 6	5.15
Type 7	5.10

In summary, the CFD results showed almost similar WCP to experimental Schlieren tests for both nozzles set 1 and 2 with the cylindrical choked die. In addition, it was found out the closed-wake condition with C-D die is more likely to occur for these two nozzles set at atomization gas pressure above 5 MPa and underexpanded condition which should be considered this behaviour during use of C-D gas die system.

6.3 CFD results for gas flow separation study

As mentioned before in the CFD literature review, one of the problems during the CCGA process is gas flow separation around melt delivery nozzle. One explanation suggests gas flow separation in which the gas boundary layers around the outer surface of the melt delivery nozzle wall separate from the wall surface creating a negative pressure gradient in this region [88]. This negative pressure gradient draws the molten metal into this region.

The new hypothesis introduced in this study mostly relates to the C-D discrete gas die systems known as Discrete Jet Pressure Inversion (DJPI). Both of these explanations have the same result with the consequence being the melt freeze-off problem around the melt delivery nozzle. The flow separation phenomenon is a function of some parameters such as melt delivery nozzle tip length and atomization gas pressure [88]. However, unlike the flow separation mechanism, which relates to the external geometry of the melt nozzle (especially melt nozzle tip length), the DJPI has a different mechanism and is more likely to occur in a discrete jet gas die system. To find the effect of melt delivery nozzle length and inclined angle wall of the melt nozzle on the gas flow separation with some series of CFD, modelling test have been conducted. The effect of melt delivery nozzle tip length on flow separation is discussed in this section and the influence of changes in inclined melt nozzle wall angle on discrete jet pressure Inversion will be considered in the next section.

6.3.1 CFD investigation of flow separation

To investigate the effect of melt nozzle tip length on gas flow separation with a cylindrical choked gas die, four different melt nozzle; each differing in melt tip length, but similar in internal profile have been conducted. These nozzles are known as nozzles type 8 to 11. These nozzles have been chosen to determine the optimum melt nozzle length in which flow separation occurs beyond that length. Moreover, it must be noted that this part of the numerical investigation is only applied on the newly designed melt nozzles with dimensions mentioned below. These nozzles are only designed numerically for the flow separation investigation. Due to previous results and reasonable agreement between numerical and experimental results for nozzles set 1 and 2, there is a confidence that these predictions will provide a good insight of the gas flow behaviour based on numerical simulations alone. The tip length dimension of these new melt nozzles is given in figure 93. The annular slit gas die design was also used. In addition, atomization gas pressures of 0.5 to 4 MPa (with an increment of 0.5 MPa) were considered for the pressure inlet boundary condition in the nozzle gas chamber.

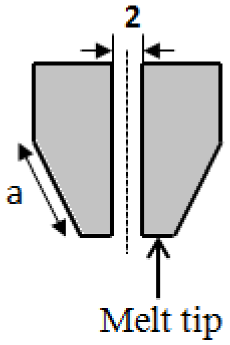

Nozzle type	Type 8	Type 9	Type 10	Type 11
a:Nozzle tip length (mm)	3	7	7.5	10

Figure 92. The melt delivery nozzle tip length for nozzles type 8 to 11. (Dimensions in mm)

Figure 94 shows the total pressure contour around the melt delivery nozzle for 4 melt delivery nozzles at the inlet gas pressure of 0.5 MPa. As can be seen in this figure, the gas flow boundary layers are attached to the outer surface wall of all the four-melt delivery nozzles.

Increasing the atomization gas pressure to 1 MPa, the gas flow layers were detached from the melt nozzle wall for nozzles type 10 and 11, indicating occurrence of flow separation. This situation is shown in figure 95. The flow separation point where the gas layers start to detach from melt nozzle external wall for nozzles type 10 and 11 occurred at around 2±0.1 mm and 5±0.1 mm from the melt nozzle tip, respectively. At the front of the separation point for nozzles type 10 and 11 there is an adverse gradient pressure (blue zone), which is shown in figure 95.

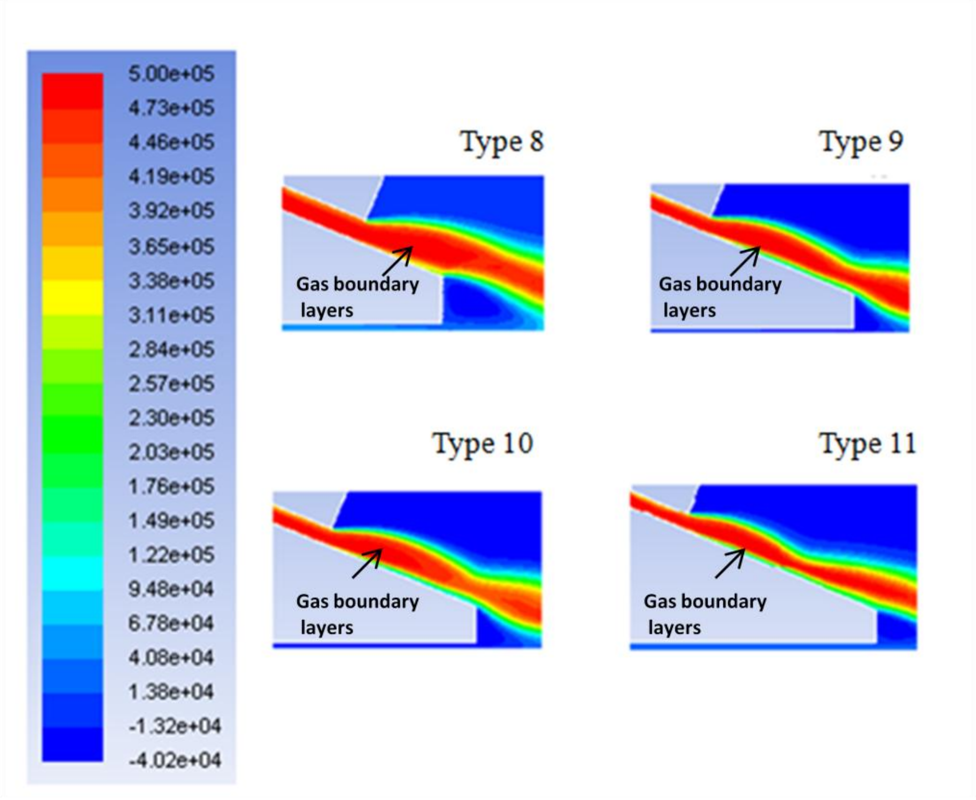

Figure 93. Pressure contours (Pa) of gas flow boundary layers around the melt delivery nozzles at the gas pressure of 0.5 MPa for flow separation study.

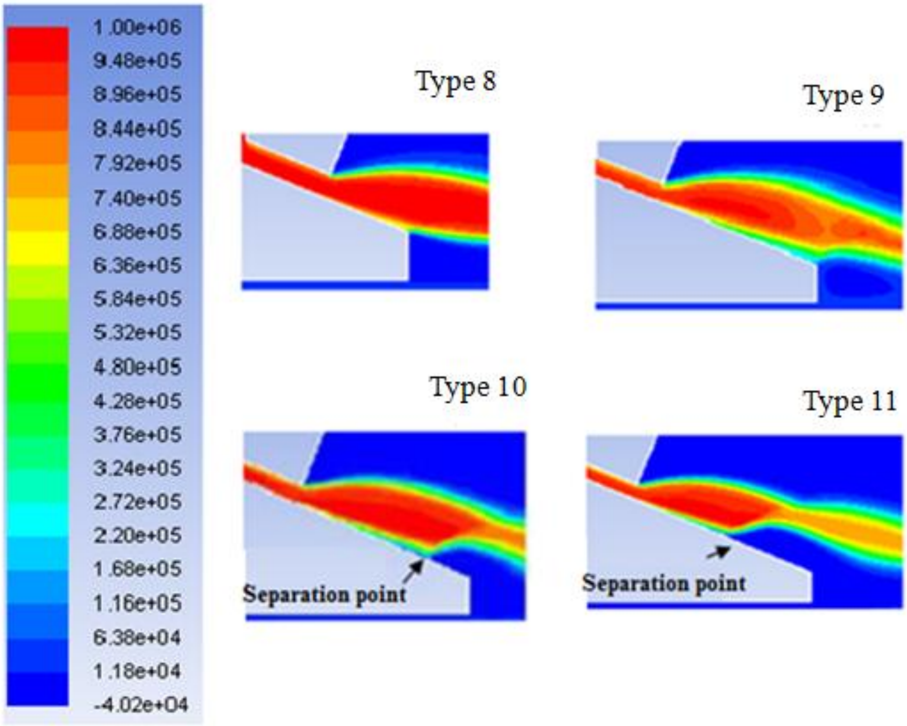

Figure 94. Total pressure contours (Pa) of gas flow pattern and flow separation point at the gas pressure of 1 MPa.

At an atomization gas pressure of 2 MPa in nozzles type 8 and 9, similar to the previous gas pressure of 1 MPa, the boundary layers still were attached to the external wall of the melt delivery nozzle however, in nozzle type 10, the separation point was moved further towards the melt tip edge. At this pressure, the separation point for nozzle type 10 occurred at around 0.94±0.1 mm from melt nozzle tip (Figures are not depicted). In addition, for nozzle type 10, no flow separation observed at the gas pressures of 2.5 MPa and above (Figure 96).

In nozzle type 11, at the gas pressures between 2 MPa and 2.5 MPa, the separation point occurred at 1.35±0.1 mm at the gas pressure of 2 MPa and 0.9±0.1 mm at the gas pressure of 2.5 MPa from the melt nozzle tip (Figure 96).

It is clearly seen that, increasing the atomization gas pressure had no significant effect on the flow separation for the nozzles type 8 and 9. For the nozzles type 10 and 11, flow separation did occur, but the separation point moved closer to the melt delivery tip with increasing the gas pressure.

Increasing the atomization gas pressure at the higher gas pressures of 3, 4 and 5 MPa had no further effect on the boundary layers separation on any of four nozzles (Figures are not presented).

The separation problem is more severe at lower gas pressures than 2 MPa for nozzle type 10 and 2.5 MPa for nozzle type 11. Furthermore, the same tests were applied for different melt nozzle tip length between 7 to 7.5 mm (with an interval of 0.1 mm) and no flow separation observed (Figures are not presented). In addition, figure 97 shows the flow separation point position from the melt tip against atomization gas pressure for types 10 and 11.

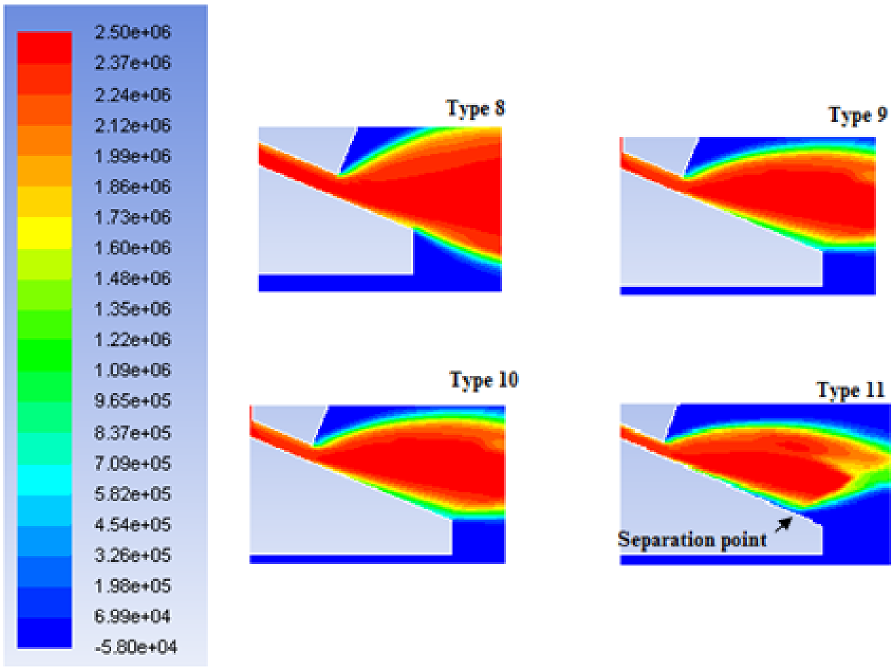

Figure 95. Total pressure contours (Pa) of gas flow pattern and flow separation point at the gas pressure of 2.5 MPa.

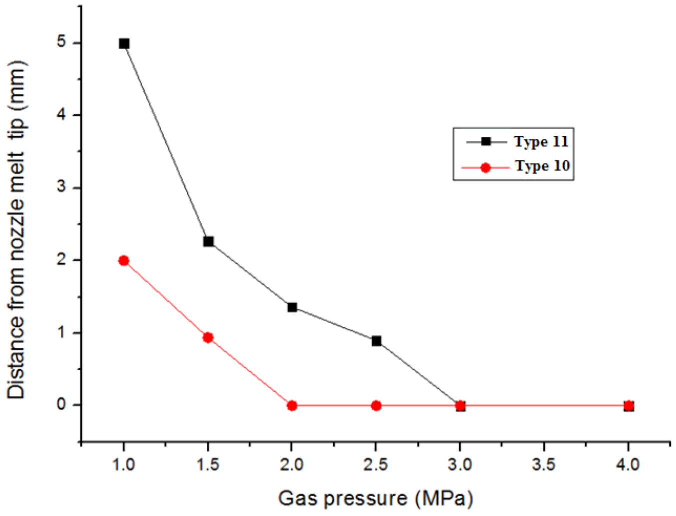

Figure 96. Distance from nozzle melt tip at different atomization gas pressure.

6.3.2 Investigation of Discrete Jet Pressure Inversion (DJPI)

As mentioned before, to analyze numerically the flow separation problem with discrete jet C-D gas die system a series of numerical tests also have been conducted. The DJPI still is not fully investigated by researchers. Therefore, for better understanding of this phenomenon; again three different melt delivery nozzles with the details given in table 9 and figure 98 were designed. The numerical nozzles have been designed numerically based on experimental nozzle geometry [58]. These melt nozzles are recognized as nozzles type 12 to 14. Nozzle type 1 is also used here as the nozzle with no miss-mach angle. These Four melt delivery nozzles have different gas jet mis-match angles (relative to melt delivery external wall).

Moreover, different atomization gas pressures at the inlet of the C-D gas die chamber were applied from 1 to 5 MPa.

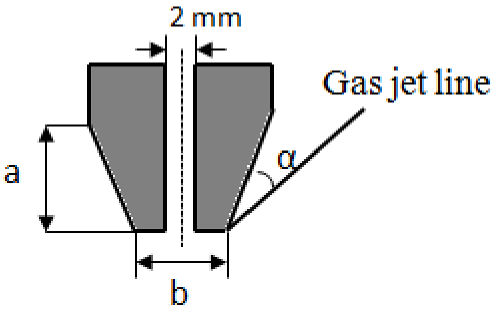

Figure 97. Details of melt delivery nozzle and miss-match angle.

Table 9. Details of melt delivery nozzles type 12 to 14.

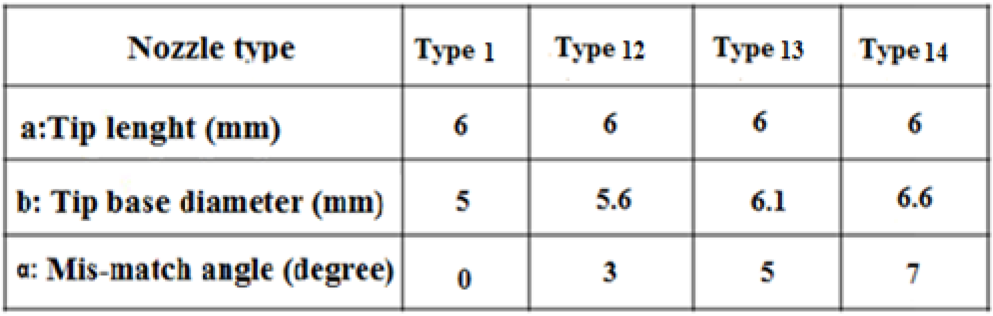

Nozzle type	Type 1	Type 12	Type 13	Type 14
a:Tip lenght (mm)	6	6	6	6
b: Tip base diameter (mm)	5	5.6	6.1	6.6
α: Mis-match angle (degree)	0	3	5	7

The mismatch angle (α) is the measured angle between melt nozzle external wall and the gas jet direction. To verify the numerical tests, the CFD results were compared with an experimental test, which was carried out with an analogue water atomizer. The same melt nozzle profile and 18-hole C-D discrete gas jet die configuration were used for experimental test. McCarthy et al. [58] have done this test previously at University of Leeds. A Pulse Laser Imaging (PLI) technique was employed for filming the back-stream flow phenomenon during water atomization [58]. PLI is an imaging technique, which operates by producing a double pulse laser beam, which can be used to create two consecutive images split by a very short time delay.

Figure 99 [58] shows a close-up PLI image of the four different melt delivery nozzles during the atomization of water with analogue atomizer at an atomization gas pressure of 1±0.5 MPa. The distance between the discrete C-D gas exit jet and the outer wall of the melt nozzle is 1.65±0.1 mm (Figure 100). The whole base of the nozzle tip is wet with the second fluid (pre-filming) as can be seen in the figure 98. For nozzle type 1, with zero melt nozzle wall inclination, corresponding to non-angular mismatch between the gas jets and the melt nozzle, significant back streaming of the atomized fluid is apparent. The amount of back-stream flow decreases by an increase in the angular mis-match of the melt nozzle (increasing the mis-match between the gas jets and the nozzle so the gas flow is inclined toward the nozzle).

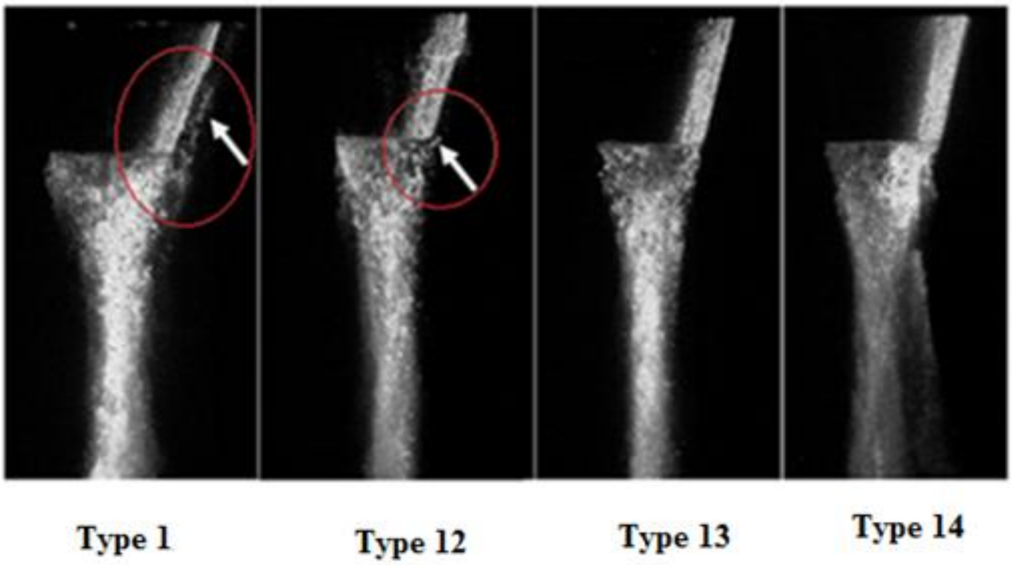

Figure 98. PLI image of back stream flow for different melt nozzle with an analogue atomizer at gas pressure of 1 MPa (arrows show water suction) [58].

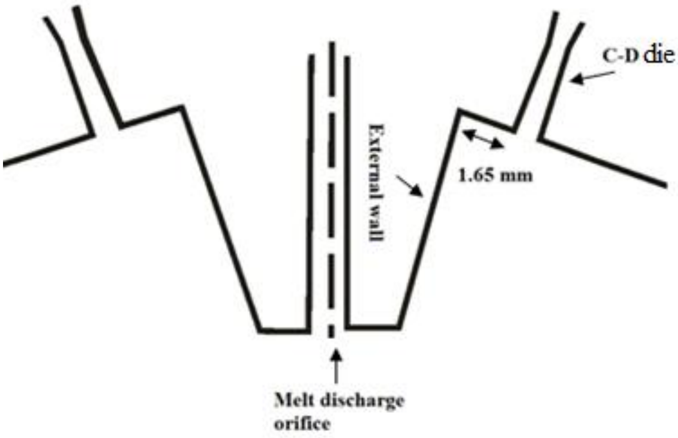

Figure 100. The position of the C-D exit jet from melt nozzle external wall.

For nozzles type 13 and 14 no back-stream flow was observed at this pressure (Figure 99). In an attempt to explain the phenomenon observed in the discrete jet gas set up, CFD modelling has been undertaken to provide further understanding of the gas boundary layer behaviour around the melt delivery external wall.

Figure 101 illustrates the numerical result of the total pressure contour for the four-melt nozzle at the gas pressure of 1 MPa. As can be seen, the flow is overexpanded after the gas jet leaves the C-D nozzle area. The negative pressure zone is a dark blue zone in this image. The region of sub-ambient pressure causes the liquid metal is drawn from the tip of the melt nozzle up to its outer surface. The molten metal is then exposed to a very cold gas jet from the gas die and solidifies rapidly; accumulates around the outer surface of the melt delivery nozzle; so, this will alter the shape of the melt delivery nozzle and clog the gas jets on the die, halting the atomization process.

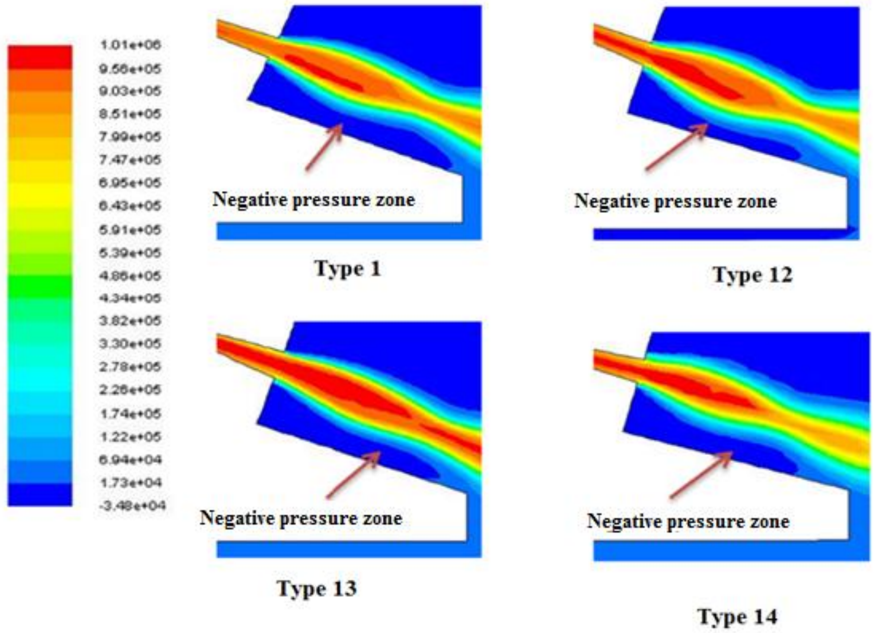

Type 1

Type 12

Type 13

Type 14

Figure 99. Total pressure contour (Pa) of gas flow around melt delivery nozzle and atomization gas pressure of 1 MPa.

For better observation of back-stream flow phenomenon at the negative pressure zone, figure 102 shows a close up of the velocity vectors plot of gas field around the external wall of the different melt nozzles. The colour of the vectors indicates the velocity magnitude; and the end of the gas recirculation region for each nozzle is shown in this figure with an arrow. For nozzle type 1, the end of the recirculation region (closest to the tip edge) reaches to a point around 1mm from the tip edge of the melt delivery nozzle. The arrow in figure 101 indicates the point at which there is a change in direction of the recirculation flow close to the external wall of melt delivery nozzle in the negative pressure zone.

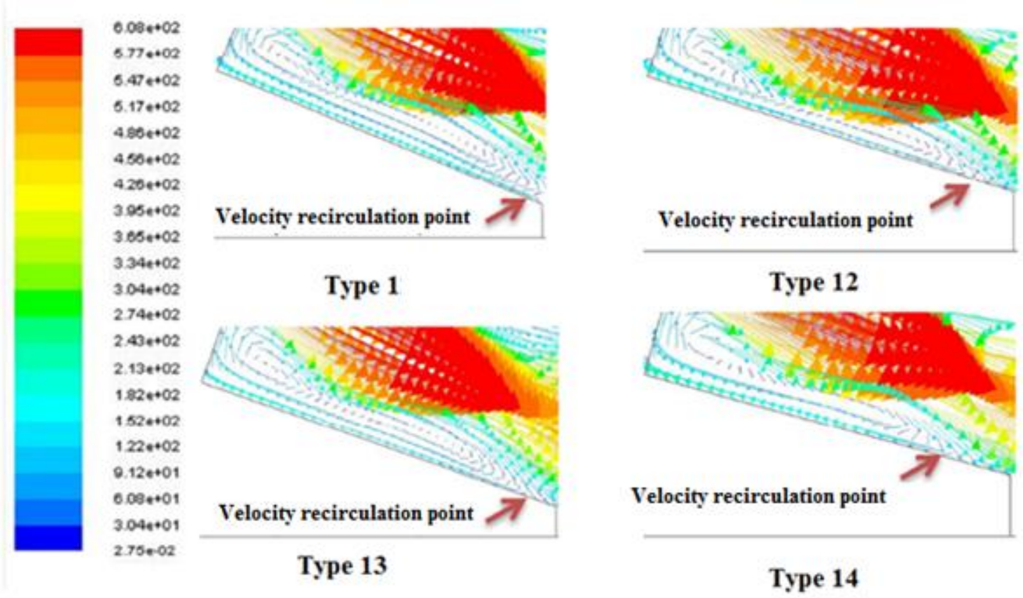

Figure 100. Velocity vector plot (m s^{-1}) of gas flow field around melt nozzle tip and atomization gas pressure of 1 MPa.

This situation arises due to the negative pressure zone. For nozzle type 12, the equivalent recirculation zone ends at a distance of 0.7±0.1 mm from the melt nozzle tip edge. This point for nozzles type 13 and 14 occurs at a distance of 0.93±0.1 mm and 1.2±0.1 mm from melt nozzle tip edge, respectively.

Figure 103 illustrates the velocity vector for all four melt nozzles at atomization gas pressure of 2 MPa. For nozzle type 1, except for a small recirculation zone that occurs at the corner of melt delivery nozzle wall, all of the velocity vectors are close to the external wall of melt nozzle and are parallel to the melt nozzle wall. The same situation was also seen for other nozzles.

In increasing the atomization gas pressure to 3.5 MPa, slightly above the design criterion for the C-D gas die, the gas showed underexpanded behaviour and a velocity of Mach 2.6. Conditions that might give rise to back-stream flow were not observed near the melt tip for any of the melt nozzles at the higher gas pressures of 3, 4 and 5 MPa. This is due to underexpanded gas jet flow where the gas flow expansion is behaving more like a choked jet. Therefore, according to the conditions considered here, it can be concluded that increasing the mis-match angle between the gas jets and the nozzle gas pressure at the gas pressure of 1 MPa, the chance of back-stream flow for nozzles type 12, 13, and 14 is significantly reduced. Also increasing the gas pressure beyond 1 MPa has the same effect on the back stream flow problem for these four nozzles (Figures are not depicted).

These results observed at the C-D gas distance of 1.65 mm from the melt nozzle external wall. So in order to investigate the effect of this distance on the back-flow and determining the maximum distance at which no back-stream flow (DJPI) will occur, the position of C-D gas exit jet has been changed to 1.6, 1.55, 1.5, 1.45 and 1.40 mm from external wall of melt nozzle in turn, for all four nozzles at an atomization gas pressure of 1 MPa.

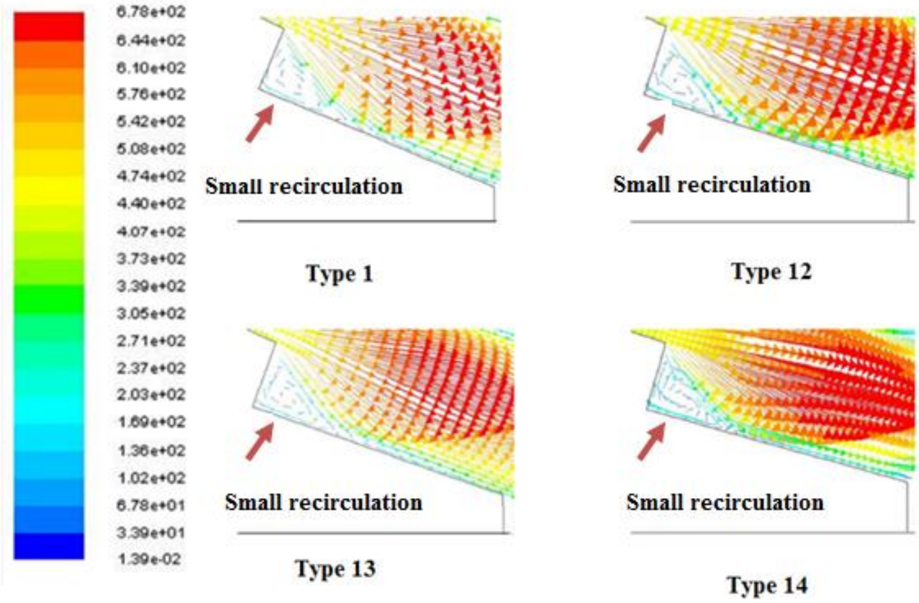

Figure 101. Velocity vector plot (m s^{-1}) of gas flow field around melt nozzle tip and atomization gas pressure of 2 MPa.

As described above, by comparison of the PLI images and the CFD results, it has been found that the back-stream flow is likely to occur when the sub-ambient pressure zone is approaching within 0.7±0.1 mm of the melt nozzle tip. According to this criterion, at gas exit jet distances of 1.6 mm, a strong back-stream flow occurred for nozzle type 1 at an atomization gas pressure of 1 MPa due to the negative pressure zone adjacent to the outer wall of the melt delivery nozzle. The distance to this negative pressure region was measured at around 0.1±0.1 mm from the tip of the melt delivery nozzle. The negative pressure zone at C-D gas exit jet distance of 1.6 mm for nozzle types 12, 13 and 14 was observed at 0.8±0.1, 1±0.1 and 1.2±0.1 mm, respectively, from melt delivery nozzle tip, wherein it conclude that back-stream flow was unlikely to occur for any of these melt nozzles.

For nozzle types 12, 13 and 14 with gas exit jet distance of 1.55 mm and at gas atomization pressure of 1 MPa, the chance of back-stream flow was also thought to be unlikely due to position of gas jet exit distance from melt delivery tip, but for nozzle type 1 the negative pressure zone was took place about 0.28±0.1 mm from melt nozzle tip and it is therefore likely that this will still causes a strong back-stream flow.

Figure 104 shows the total pressure contour of four melt nozzles at atomization gas pressure of 1 MPa with C-D gas jet exit distance of 1.5 mm. For nozzle types 1 and 12, the negative pressure zone occurs at 0.57±0.1 mm and 1.31±0.1 mm from melt delivery tip respectively, while for nozzle types 13 and 14 the corresponding values were 1.63 mm and 1.65 mm from melt nozzle tip. The chance of back-stream flow still exists for nozzle type 1 due to the negative pressure zone being within 0.57±0.1 mm of melt nozzle tip. With decreasing the gas jet exit distance from 1.65 mm to 1.5 mm for nozzle types 12, 13 and 14 the negative pressure zone was measured at a more distance from melt delivery tip and with increasing the gas jet mis-match angle, this negative pressure zone is become smaller and the effect of back-stream flow is significantly decreased.

For a distance between the C-D jet and the external melt nozzle wall of 1.45 mm, the adverse pressure zone was measured to begin around 0.7±0.1 mm from melt nozzle tip edge of a type 1 nozzle at atomization gas pressure of 1 MPa. This is equal to the limit of a weak stream flow occurrence. No back stream-flow is expected for the rest of melt nozzles. In addition, when decreasing the gas jet exit distance to 1.4 mm, back-stream flow is not expected to be a problem with any melt nozzle type. It was therefore decided to measure the maximum limitation in which this phenomenon can occur between the condition of weak to no back-stream flow, particularly for nozzle types 1 and 12. Consequently, the gas jet exit distance of 1.64 mm and 1.44 mm from external melt delivery nozzle was numerically tested to identify this limitation.

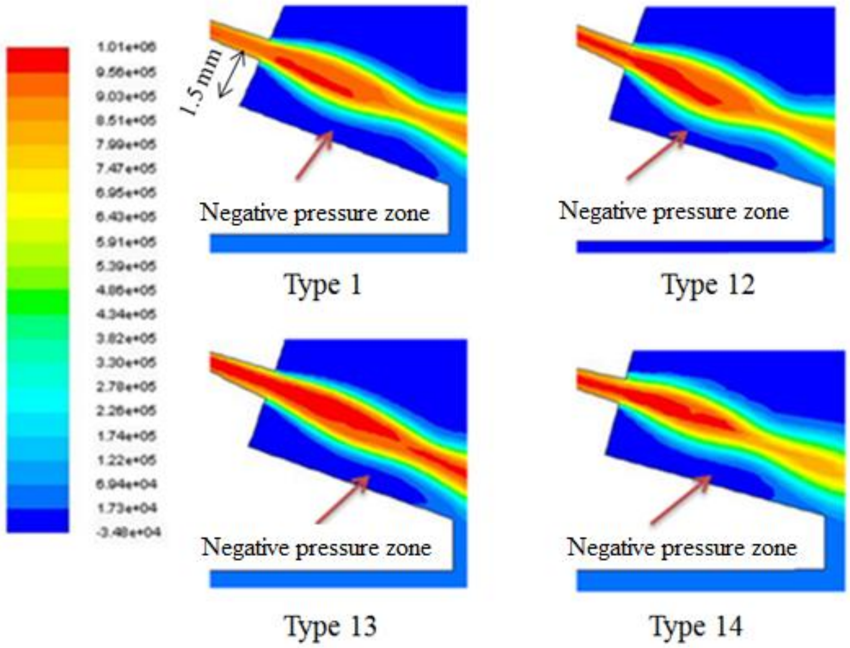

Figure 102. Total pressure contour (Pa) of four melt nozzles at atomization gas pressure of 1 MPa with C-D gas jet exit distance of 1.5 mm.

At a gas jet exit distance of 1.44 mm, the adverse pressure zone was moved to 0.91±0.1 mm from melt nozzle tip edge for nozzle type 1 and for gas exit distance of 1.64 mm this region was placed at 0.73±0.1 mm for nozzle type 12. So, the maximum gas jet exit distance limitation in which no back-stream flow (DJPI) was predicted for nozzle type 1 and type 12 was obtained at 1.44 mm and 1.64 mm, respectively from melt nozzle external wall. At higher atomization gas pressure of 1 MPa like previous condition, no back-stream flow was expected for these two nozzles. For the rest of three melt nozzle types, the negative pressure zone was placed at a distance more than 0.7±0.1 mm from melt tip and back-stream flow is unlikely.

7 Discussion

7.1 Schlieren and CFD results of gas flow for melt nozzle set 1

As noted in section 5 and 6-2, both experimental and CFD studies showed that the most significant difference in WCP was observed between types 1 and 4 designs. A large difference in WCP was also noted when comparing type 5 with type 6 and type 7 designs (Type 7 showed lowest WCP). The transition between open to closed-wake condition appears to be influenced by the combined effects of the melt nozzle tip internal profile and the resulting recirculation zone shape that forms. A useful first step is to clarify how the closed-wake occurs for each nozzle at WCP in terms of considering how the flow behaviour changes as inlet pressure increases. To aid with this explanation, nozzle type 1 has been chosen as a reference case to investigate the flow behaviour leading to WCP. The other nozzle cases can then be understood relative to this case. In the experimental and CFD study this nozzle was observed to have a WCP of 4.5±0.5 MPa and 4.75 MPa, respectively for the choked gas dies. The CFD predictions for the velocity field and velocity streamlines for this nozzle are shown in figures 105 to 107.

The key flow behaviour observed as the pressure is increased towards WCP is outlined below for nozzle type 1. As seen in figure 105, at a gas pressure of 1 MPa the open-wake condition is evident; the gas leaves the die and is seen to expand rapidly as it moves away from the die exit. It forms a ‘convex lens’ shape as the flow first expands then contracts. This situation causes some recompression shocks to form around the melt nozzle tip edges, which reduce the gas velocity. The gas re-accelerates then decelerates to form a set of Prandtl-Meyer waves along the central axis. It can be seen that a recirculation zone forms at the front of the melt tip and beneath the expanding gas jet. Increasing the gas pressure to 2 MPa causes an expansion of the convex lens shape gas wave in both directions (length and width) as seen in figure 106. The recirculation zone, which is surrounded by the expanding gas wave, is squeezed downwards by the convex lens shape expanding gas wave. This causes the change in both shape and size of the recirculation zone compared to the previous lower inlet gas pressure (Figure 106). Finally at the WCP or closed-wake condition (4.75 MPa) the forming recirculation zone is pinched-off by the further expanded (convex lens shape) jet. A Mach disk is seen to form at the front of the melt tip (Figure 107). The transition to closed wake condition is due to the expanding jet increasing in size to the extent that it reconnects with itself at the centre. It is important to note that this mechanism of transmission from open to closed-wake condition is observed to occur for a similar reason (expanding jet meeting itself at the centre) for all of the nozzles tested in experiments, but at different gas pressures.

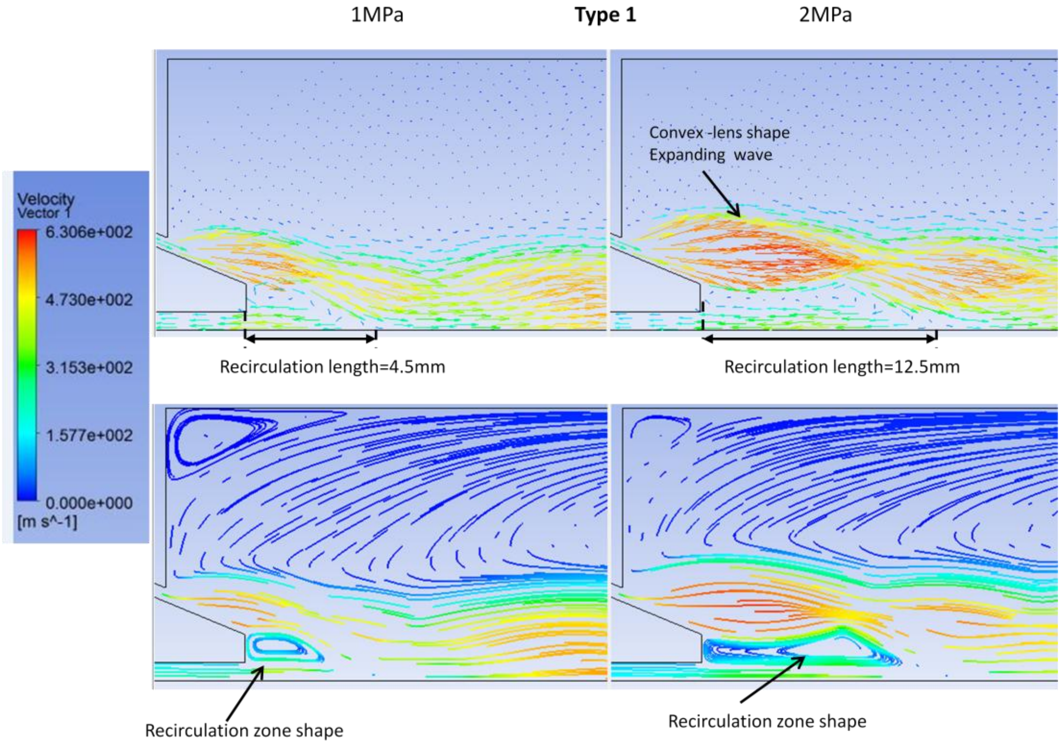

Figure 103. The velocity field and velocity streamline for nozzle type 1 at gas pressures of 1and 2 MPa at the open-wake condition with a choked die.

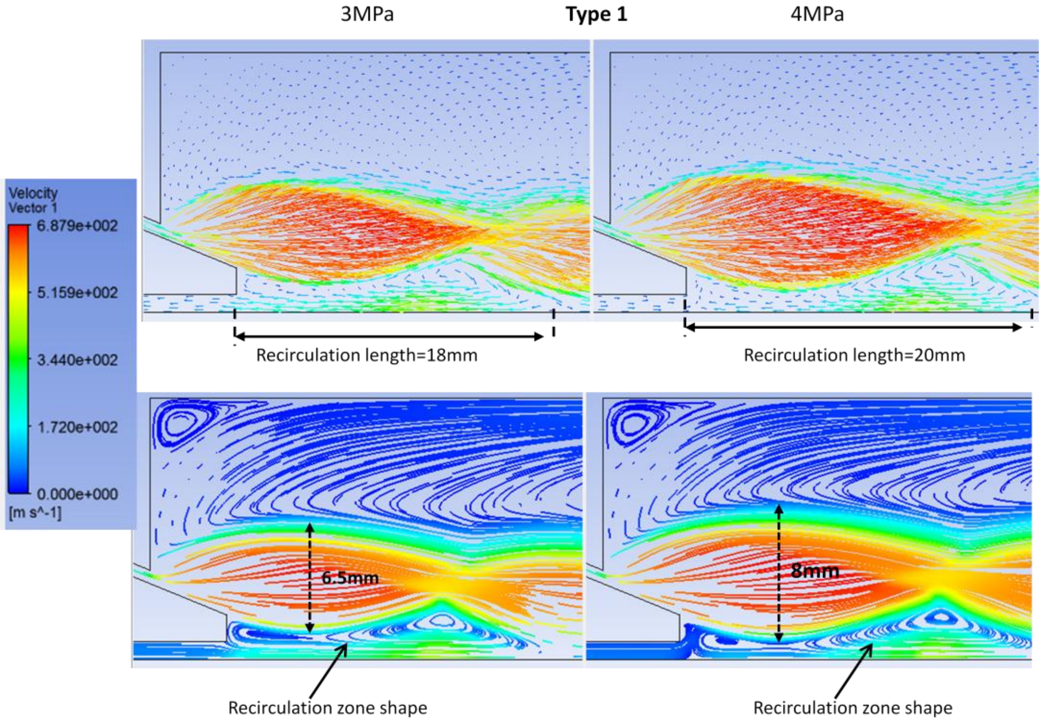

Figure 104. The velocity field and velocity streamline for nozzle type 1 at gas pressures of 3 and 4 MPa at the open-wake condition with a choked die.

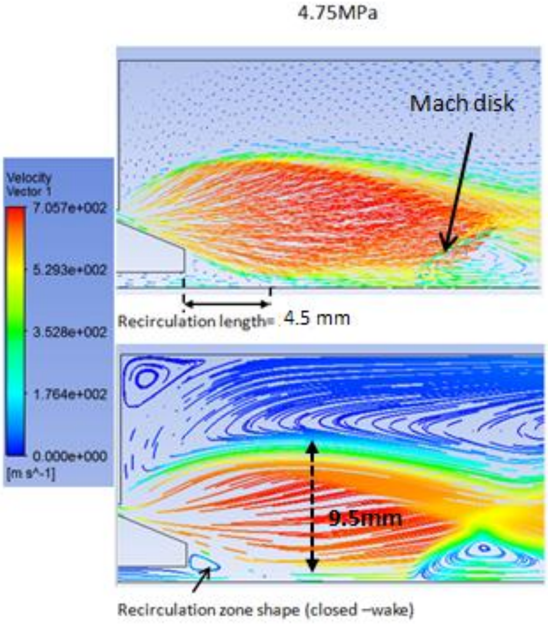

Figure 105. The velocity field and velocity streamline for nozzle type 1 at gas pressure of 4.75 MPa and the closed-wake condition with a choked die.

The open to closed-wake condition for nozzle type 1 with the C-D gas die also was seen to follow the same trend, but with the C-D die always transitioning at a higher WCP for both nozzle sets. To investigate this behaviour the difference in gas flow fields between the choked and C-D gas die (for a given nozzle design) is considered. Figures 108 to 110 show the velocity field and streamlines for type 1 with the C-D and choked gas die at the same inlet gas pressures. As noted, a higher WCP is found in the case of the C-D design. The reason for this can be understood in the context of how the closed-wake occurs. In the case of the C-D design, the overexpanded exiting jet does not expand to the same extent as the choked design (as expected). This can be observed in figure 108.

It was found that the convex-lens shape expanding gas wave width at the open-wake condition with a cylindrical choked die is larger than overexpanded or underexpanded wave width for the C-D gas die. It can be seen that the convex-lens shape gas wave is more collimated in a C-D gas die compared to choked die (Figure 108). In the case of the choked design the larger width of the expanding wave pinches-off the recirculation zone at a lower gas pressure compared to the C-D gas die (Figures 109 and 110). It should be noted that a similar trend is observed for all melt nozzles with the C-D and choked designs regardless of melt tip geometry with the same conclusion that WCP occurs at a higher pressure for the C-D case. This condition is also supported by the argument of Anderson and Ting that WCP for the C-D gas die was measured at a gas pressure of 5 MPa [48].

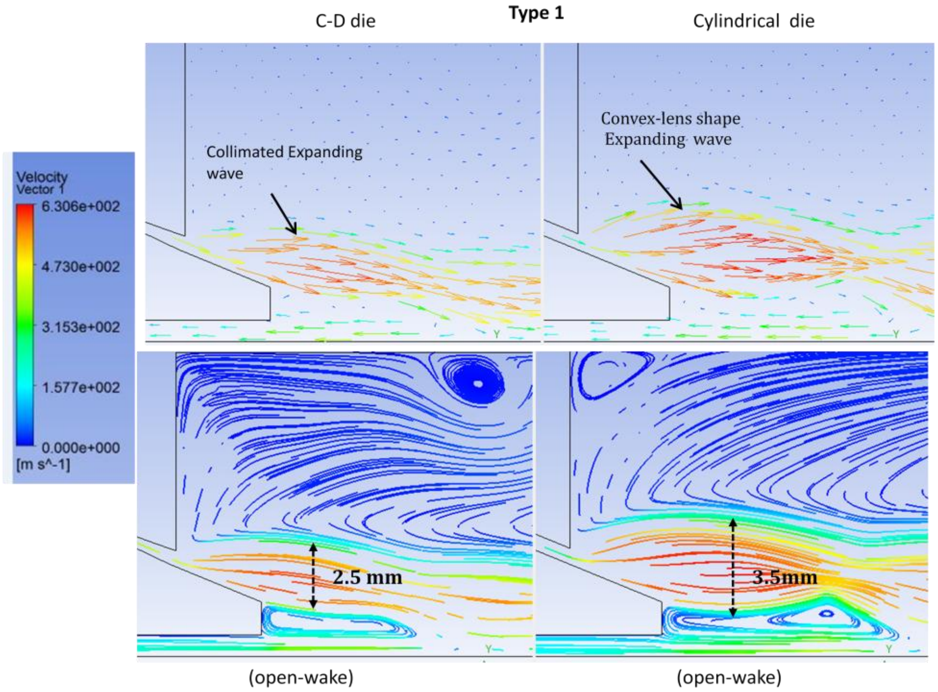

Figure 106. The velocity field and velocity streamline for nozzle type 1 at gas pressure of 2 MPa at open-wake condition with the C-D and cylindrical gas die.

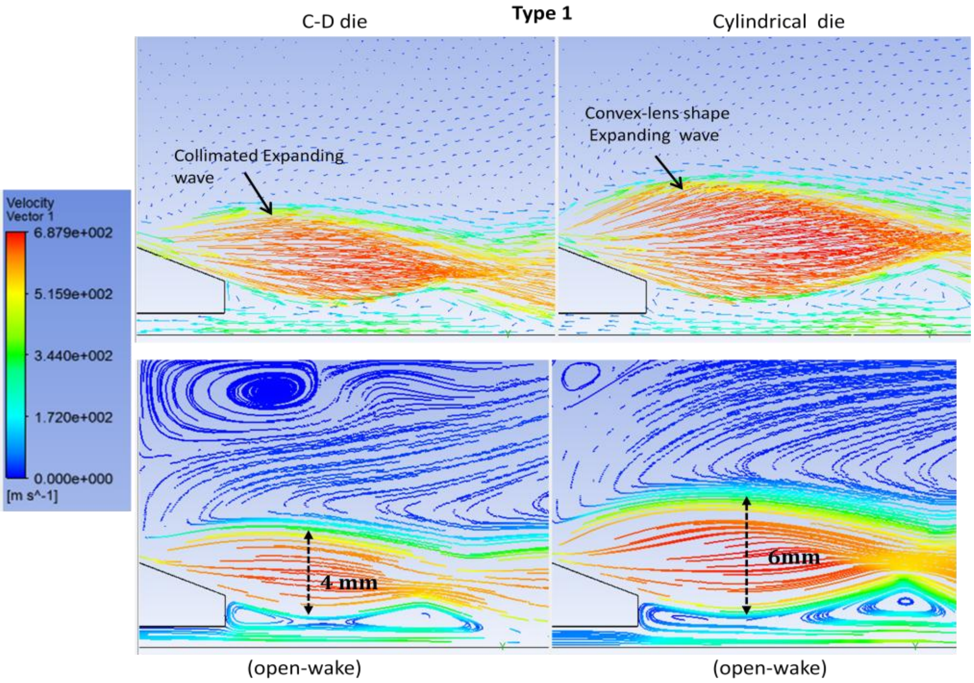

Figure 107. The velocity field and velocity streamline for nozzle type 1 at gas pressure of 4 MPa at open-wake condition with the C-D and cylindrical gas die.

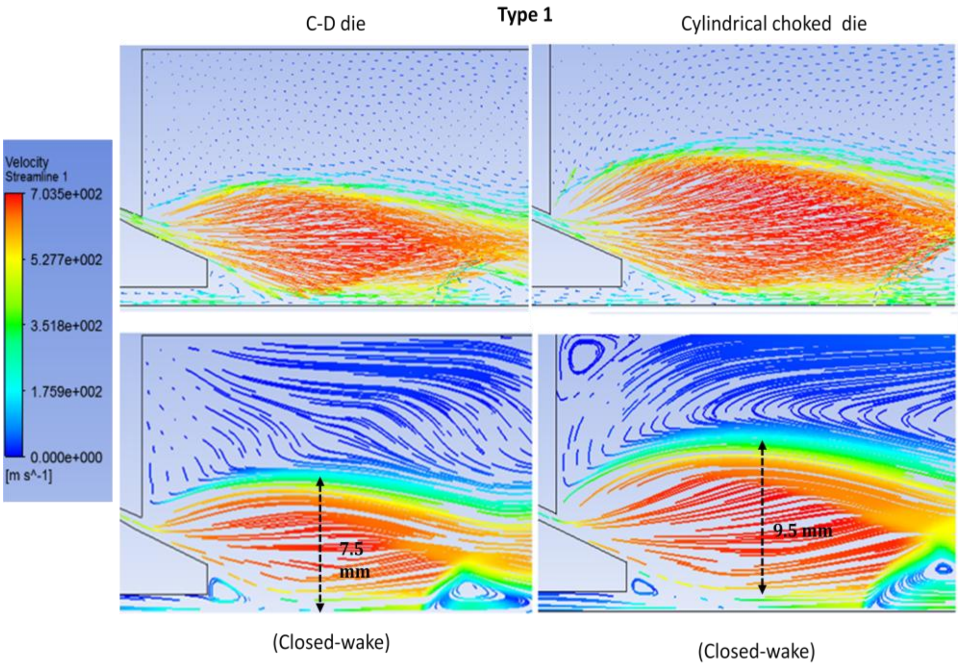

Figure 108. The velocity vectors and velocity streamline for nozzle type 1 at gas pressures of 5.3 and 4.75 MPa at closed-wake condition with the C-D and cylindrical gas die, respectively.

The next step is to consider the reasons of why WCP is depends upon melt nozzle tip design. To do this nozzle type 4 is compared to type 1, which shows a significant difference in WCP. Figures 111 to 113 show the velocity field and streamline for the cylindrical choked die in these two nozzles. Figure 110 demonstrates that the length of the convex-lens shape expanding gas wave for both nozzles design is the same at 1 MPa (4.6±0.1 mm as observed in figure 111). This is also the case at 2 MPa (13±0.1 mm). This shows that convex-lens shape wave extension is not significantly impacted by the change to the melt nozzle design; however, the shape of the convex-lens shape gas wave is different (due to the different geometry and the different resulting recirculation zone shape). It appears that although, the size of the expanding gas wave stays comparably the same, the shape/direction of the expanding wave is different in both nozzles. In addition, the recirculation zone also forms at front of these melt tips.

The length and shape of the recirculation zone is different for both nozzles as depicted in figures 111 to 113. Increasing the gas pressure from 1 to 2 MPa for each nozzle shows the convex-lens shape gas wave expands in both directions, but the force balance between recirculation zone and expanding wave appears to restrict this expansion in width.

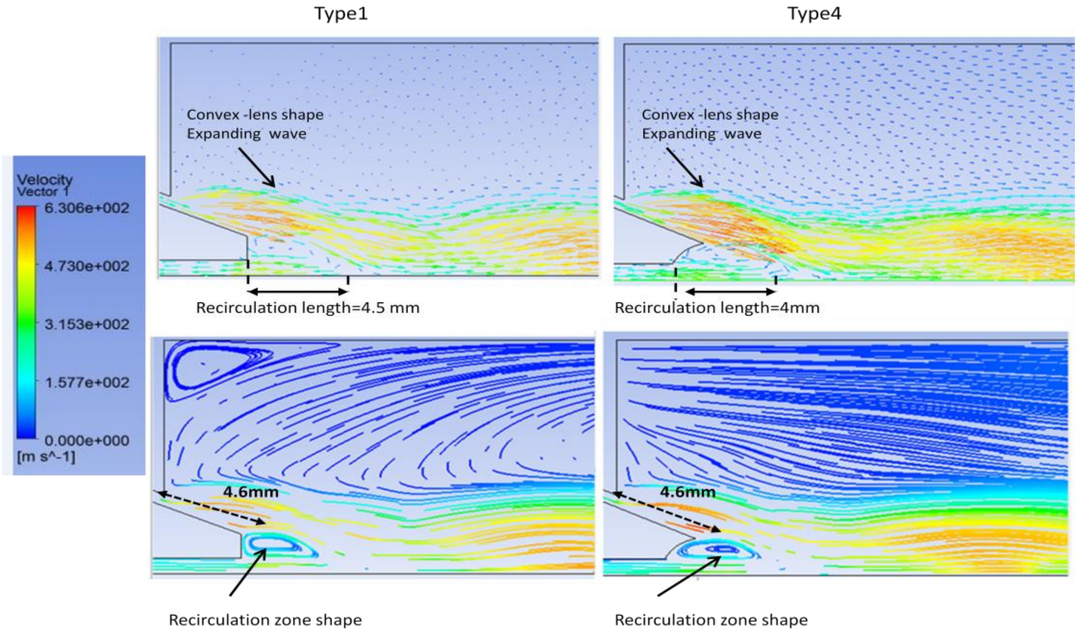

Figure 109. The velocity field and velocity streamline for nozzles type 1 and 4 at gas pressure of 1 MPa and open-wake condition.

Moreover, the shape of the recirculation zone is also influenced by the melt tip shape design. The hemispherical shape of type 4 results in a different shape of the recirculation zone compared to type 1 with the flat tip head (Figures 111 and 112). The observed flow of the gas inside the melt tip cavity appears to influence the direction of the incoming gas jet at the meeting point with the upcoming gas from the recalculation zone (Figure 114). The recirculation shape for type 4 with a hemispherical shape allows the convex-lens shape gas wave to expand further in width, and downward into the recirculation zone. This condition at WCP for type 4 causes earlier pinching-off the recirculation zone at a lower gas pressure compared to type 1. The open to closed-wake mechanism for types 2 and 3 is very similar to type 1 and 4, respectively.

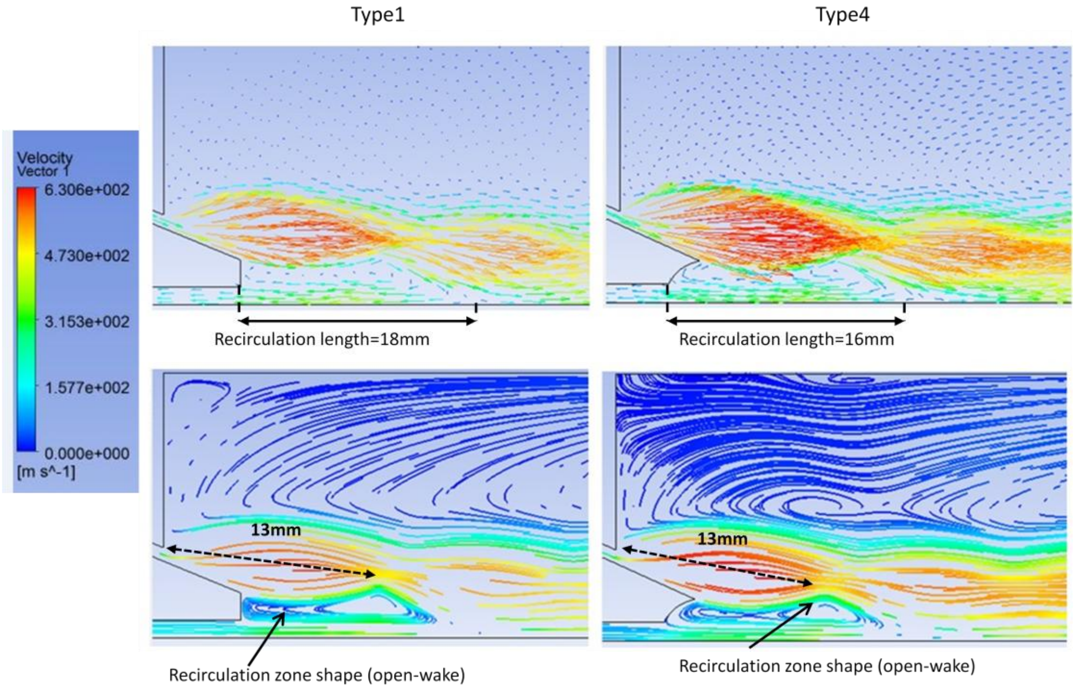

Figure 110. The velocity field and velocity streamline for nozzles type 1 and 4 at gas pressure of 2 MPa and open-wake condition.

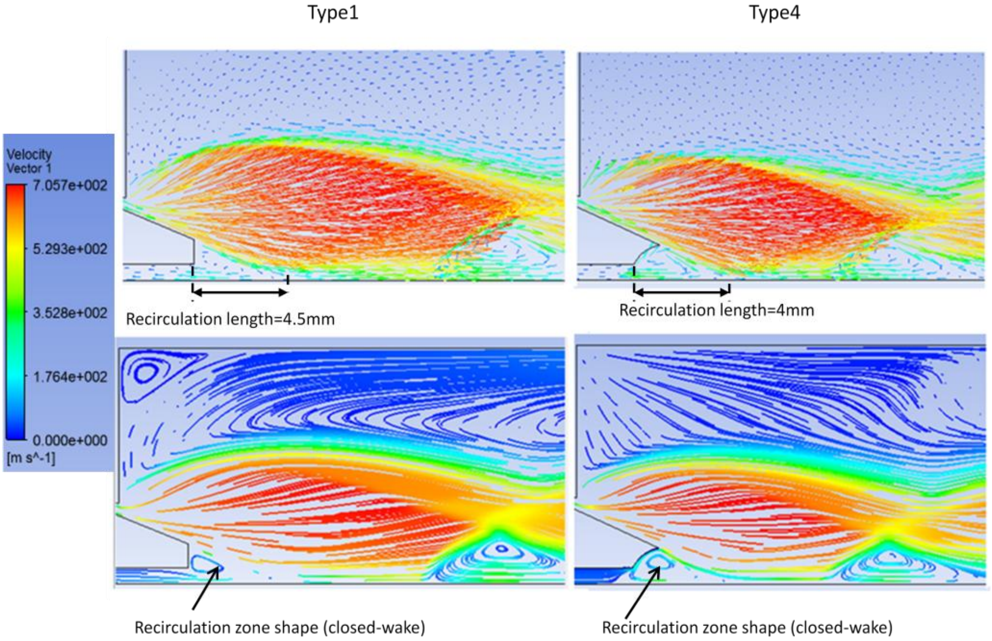

Figure 111. The velocity field and velocity streamline for nozzles type 1 and 4 at gas pressure of 4.75 MPa and 2.75 MPa, respectively and closed-wake condition.

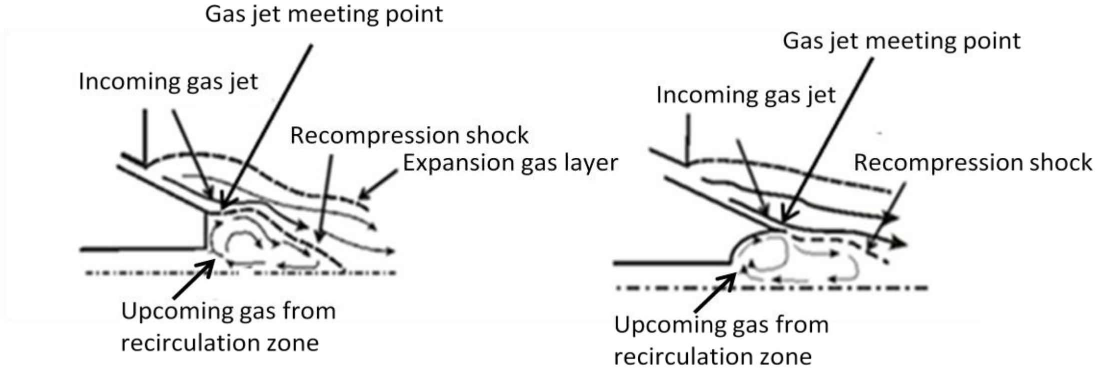

Figure 112. A schematic view of gas flow and gas jets meeting point for nozzles type 1 and 4 at open-wake condition and gas pressure of 1 MPa.

7.1.1 Schlieren and CFD results of gas flow pattern of melt nozzle set 2 with a cylindrical choked die

The same explanation and mechanism of open to closed-wake condition was observed for nozzle set 2. Nozzle type 5 and 6 in the experimental Schlieren tests, which showed the open and closed-wake condition at a gas pressure of 3.5 and 2.5 MPa, respectively. This pressure for nozzle type7 was measured 2 MPa. The CFD results show the WCP at 3.75 MPa in nozzle type 5, 2.5 MPa in type 6 and 2 MPa in type 7. Similar to the nozzle set 1, the CFD velocity field and stream lines (Figures 115 to 118) can help to explain why nozzles set 2 showed different WCP.

At an atomization gas pressure of 1 MPa, nozzle type 5 (Figure 115), shows the convex-lens shape expanding wave at the front of choked gas die and the length of this expanding wave at the gas pressures of 1 and 2±0.5 MPa is about 6±0.1 mm and 15±0.1 mm, respectively (Figures 115 and 116). The same expanding gas wave length is also observed for type 6 at figures 115 and 116. The recirculation zone length at front of melt tip for these two nozzles also depicted in figures 115 and 116. The recirculation zone shape at front of melt tip for types 5 and 6 is also influenced by melt tip shape profile. Similar to nozzle type 4, the gas flow field inside the melt tip cavity changes the incoming gas jet direction at the gas meeting point (Figure 117). This condition for type 6 causes more expansion of the convex shape wave in width. At this condition, the grooved tip design of type 6 influences the shape of recirculation zone and causes earlier pinching-off the recirculation zone at the lower WCP compared to type 5 with a flat tip (Figure 118).

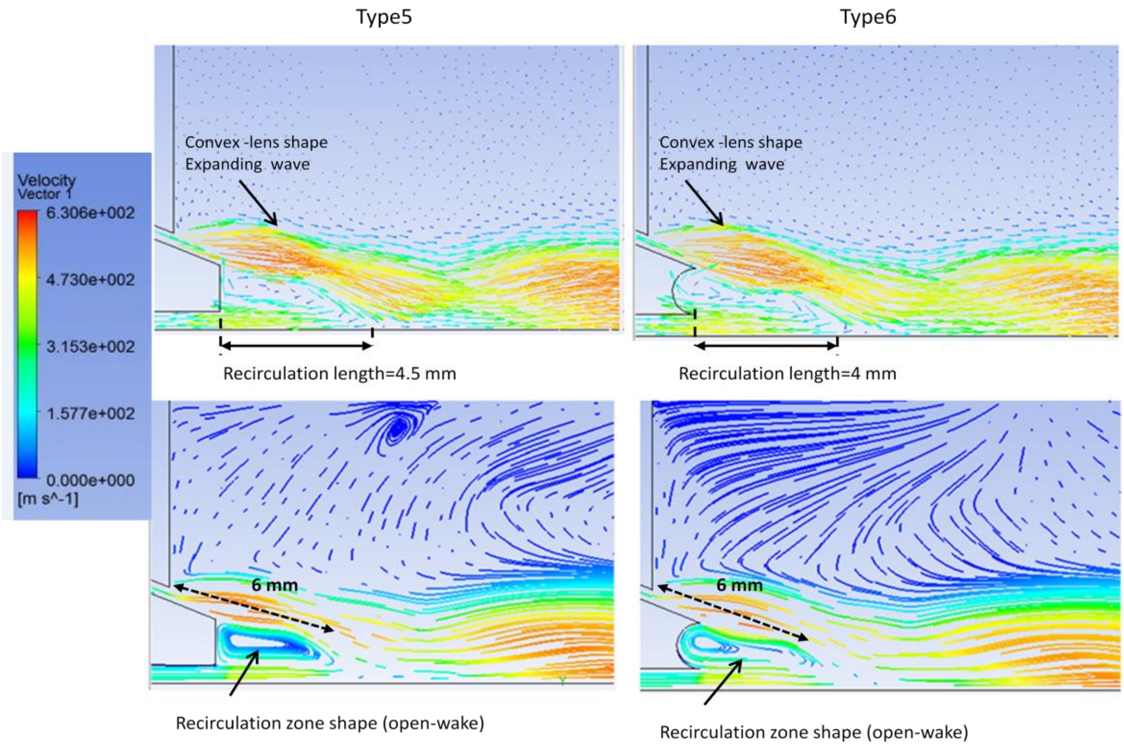

Figure 113. The velocity field and velocity streamline for nozzles type 5 and 6 at gas pressure of 1 MPa and open-wake conditions with choked die.

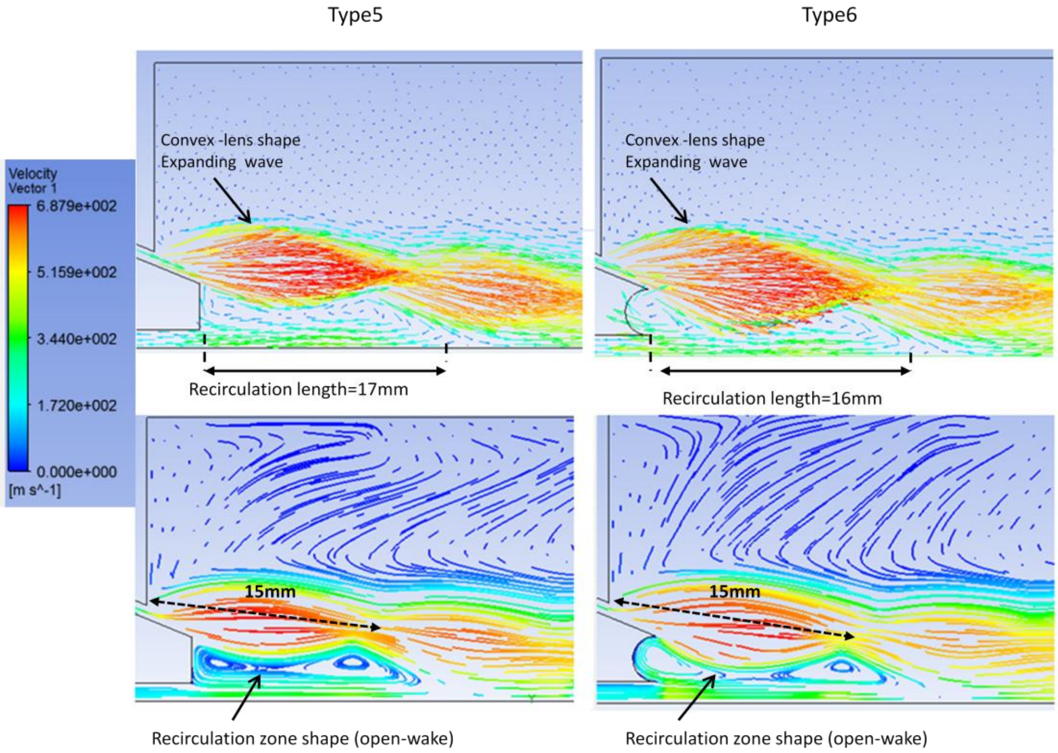

Figure 114. The velocity field and velocity streamline for nozzles type 5 and 6 at gas pressure of 2 MPa and open-wake conditions with the choked die.

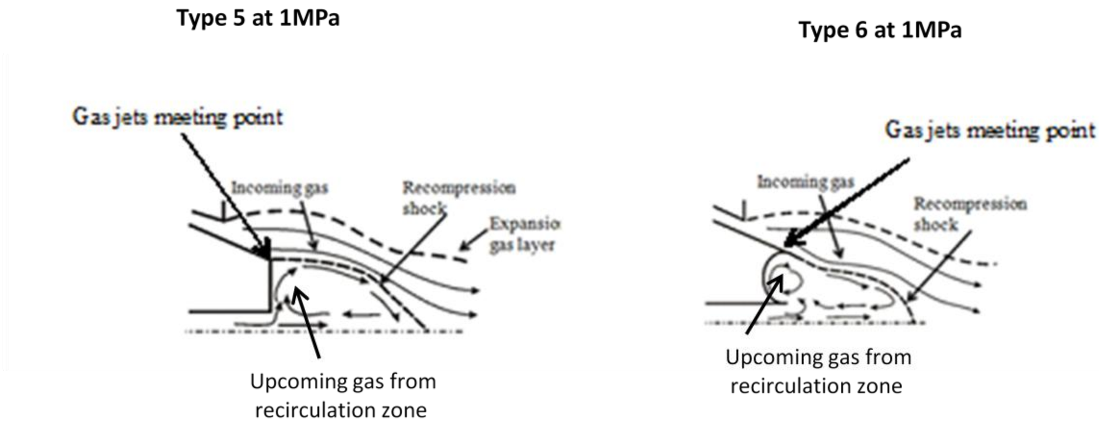

Figure 115. A schematic view of gas flow and gas jets meeting point for nozzles type 5 and 6 at open-wake condition and gas pressure of 1 MPa.

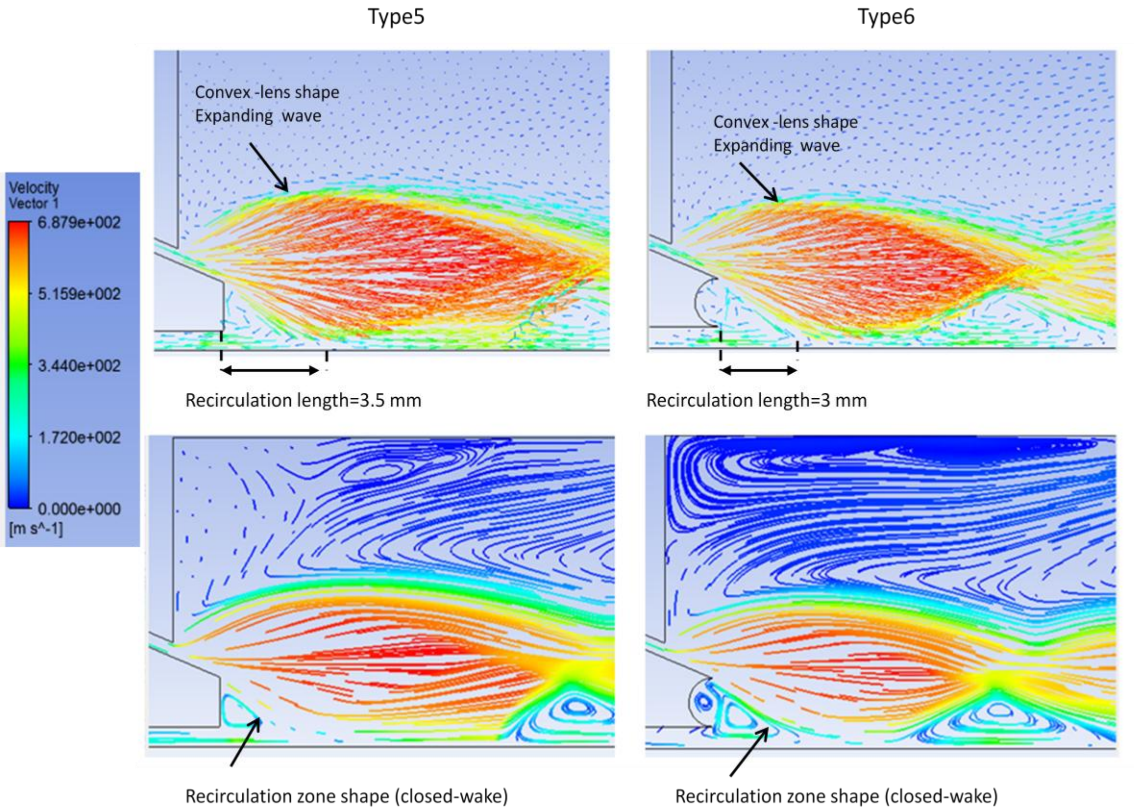

Figure 116. The velocity field and velocity streamline for nozzles type 5 and 6 at gas pressures of 3.75 MPa and 2.5 MPa, respectively and closed-wake condition with the choked die.

Furthermore, nozzle type 7 is a good reference for showing the effect of recirculation zone on the expanding gas wave pinch-off mechanism. This nozzle has no lip at the nozzle tip (Figures 119 and 120) and the upcoming gas from recirculation zone less influences the incoming gas jet direction. Therefore, in the absence of any significant recirculation zone this nozzle type displays the lowest observed WCP of 2 MPa, establishing the link between the expanding gas wave and the recirculation zone coupling forces balance on WCP. The open to closed-wake condition mechanism is similar to previous ones.

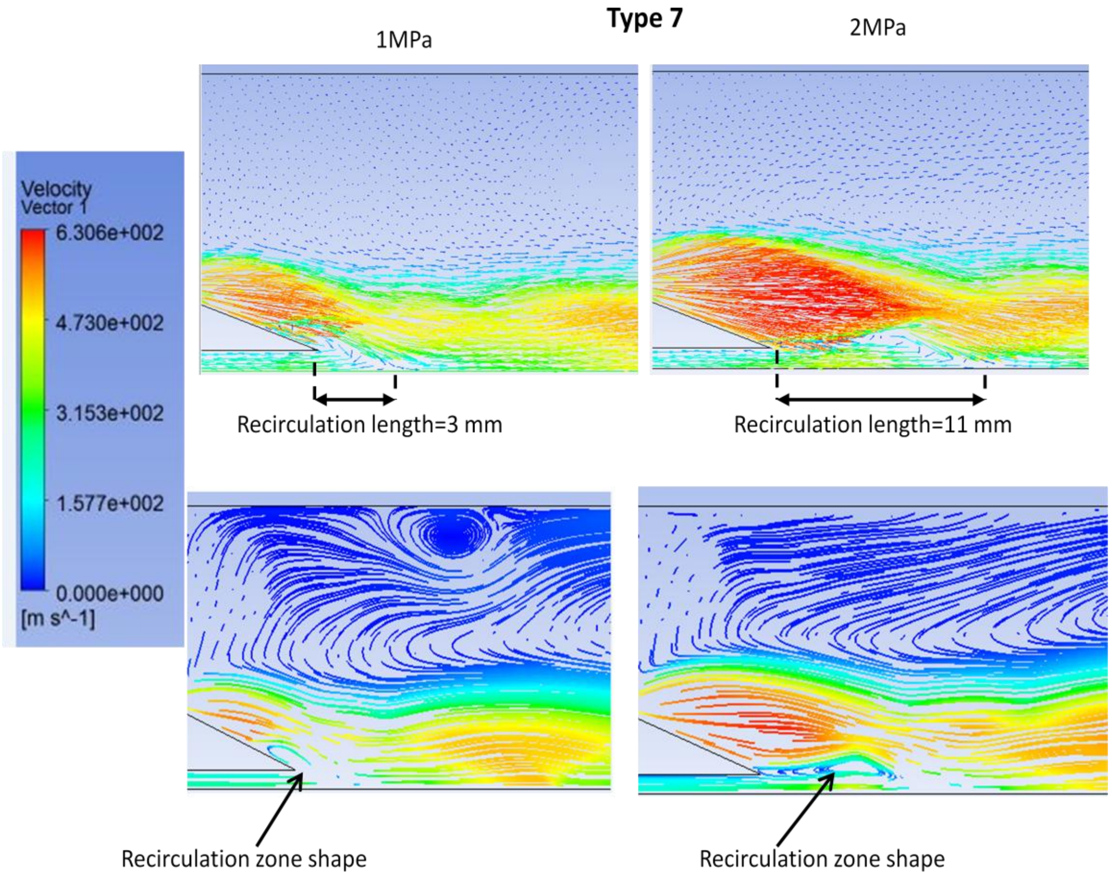

Figure 117. The velocity vectors and velocity streamline for nozzle type 7 at gas pressures of 1 MPa and 1.5 MPa and open-wake condition.

To sum up, it seems that the WCP is influenced by three factors of gas die type (Choked or C-D gas die); melt tip profile design and recirculation zone shape. The recirculation zone and expanding gas wave have a coupling effect to each other ,but To determine which one of these factors may have more effect on WCP more investigation is proposed in future by designing the new melt tip like types 4 and 6 with different size in tip cavity depth.

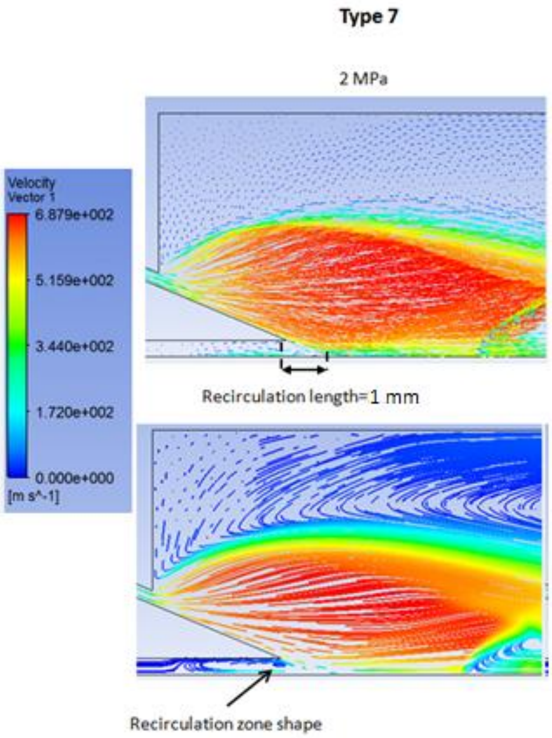

Figure 118. The velocity vectors and velocity streamline for nozzle type 7 at gas pressure of 2 MPa and the closed-wake condition.

7.2 Gas flow separation with a cylindrical choked die

The flow separation investigation by CFD modelling has been done in nozzles type 8 to 11. At low gas pressure of 0.5 MPa (Figure 94), no flow separation occurred for each nozzle; however, increasing gas pressure to 1 MPa, causes flow separation in nozzles type 10 and 11. At this gas pressure, the gas flow layers were detached from these nozzles external wall. The separation point in nozzles 10 and 11 occurred at around 2 and 5 mm from the nozzle tip, respectively. At this point, there is an adverse gas pressure at melt delivery external wall, which is shown in dark blue colour in figure 95. This adverse pressure will cause the liquid metal to be sucked from the end face of the melt delivery nozzle into its outer surface of nozzle in the dark blue area. The liquid metal is then exposed to a very cold gas jet from gas die and solidifies rapidly, accumulating around the outer surface of the melt delivery nozzle. This will alter the shape of nozzle and clog the gas jets on the die, halting the atomization process.

The position of the separation point on nozzle tip plays a crucial role in determining whether this occurs. If, the separation point happens far from nozzle tip, the effect of molten metal back flow will be more intense.

Increasing the gas pressure, accelerates the gas flow boundary layers at the melt nozzle external wall surface and moves the separation point toward the melt tip. This condition for nozzles type 8 and 9 causes the flow separation eliminated and for nozzles type 10 and 11 with longer melt tip causes the separation point occurs at some distance closer to melt tip (Figure 95). Flow separation also eliminated at high gas pressure beyond of 2 MPa for melt nozzles type 8, 9 and 10. According to these results, the separation problem is more likely to occur for nozzle tip length of 7.5±0.1 mm and above in this test.

Therefore, based on these results, the separation phenomenon is more severe at a low atomization gas pressure of 2 MPa in nozzle type 10 and 2.5 MPa in nozzle type 11.

The idea of dimples at outer surface of external nozzle wall brought from gulf balls where dimples at the ball outer surface develop the turbulence flow around the ball; as a result, the airflow separation and drag force decrease. This method was applied on external nozzle wall with random size of dimples. Figures 121 and 122 show schematic and velocity field view of nozzle type 11 at gas pressure 1 MPa where highest separation occurred. Therefore, it has concluded the dimples develop the vortices flow on external wall and decreases the separation phenomenon. It should notice that at this part of this study there are some questions come up such as: how many dimples should are be? How deep and what shape the dimples should have? Answering to these questions need more numerical investigations that proposed for the future work to see the effect of that on nozzle performance.

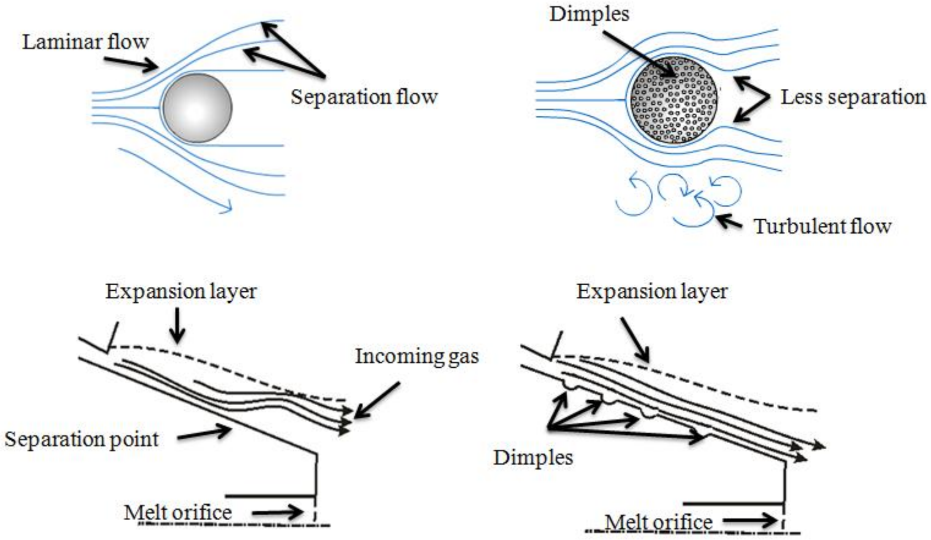

Figure 119. Schematic view of nozzle type 11 with and without dimples at the gas pressure of 1 MPa.

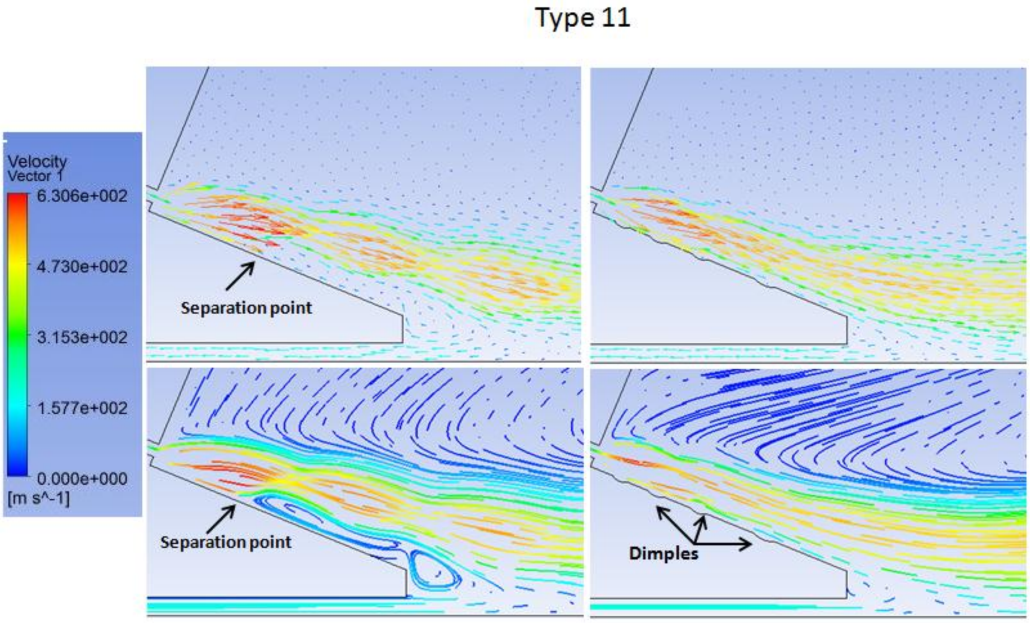

Figure 120. Velocity field and streamlines of nozzle type 11 with and without dimples at the gas pressure of 1 MPa.

7.3 Investigation of mis-match angle on gas flow separation with the C-D gas die

In this part the results of mis-match angle of nozzle external wall on flow separation is discussed.

The Discrete Jet Pressure Inversion (DJPI) is another mechanism, which is more likely to occur in a discrete C-D gas jet die system where the exit gas is more collimated. This phenomenon is still not fully investigated by researchers.

Figure123 demonstrates the schematic representation of the gas flow separation problem at annular slit die and the proposed DJPI mechanism that has been observed in this experiment with discrete jet die.

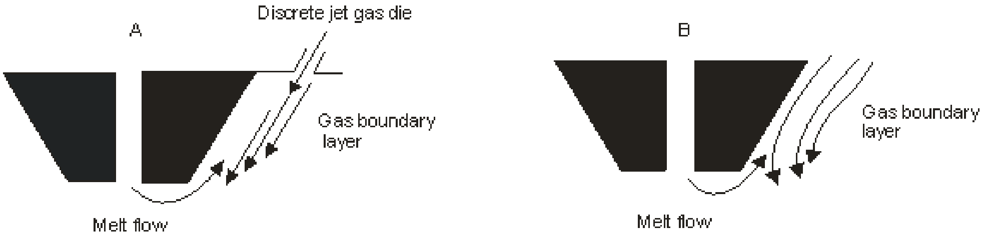

Figure 121. The Schematic view of gas flow separation mechanism by A: DJPI, B: flow separation at annular slit die system.

By comparing the PLI images shown in figure 99 with CFD pressure contour on figure 101, it is anticipated that nozzle type 1 with zero mis-match angle showed the highest DJPI and more liquid (water in analogue atomizer) was drawn back to the sub-ambient or negative pressure recirculation zone around melt delivery external wall; and as mentioned on section 6-3-2, the end of recirculation region (closest to the melt tip edge) was measured around 0.1±0.1 mm. The region of sub-ambient pressure causes the liquid metal to be drawn from the tip of the melt nozzle up to its outer surface.

For nozzle type 12 (Figure 102), the recirculation region ending in distance of 0.7mm from the melt nozzle tip would give rise to marginal back streaming behaviour, since the recirculation flow in this case would be just isolated from the atomisation region.

It can be observed that (Figure 102) by moving from nozzles type 1 to type 14 at the atomization gas pressure of 1 MPa, the position of the end of the recirculation region moves further away from the nozzle tip. This indicates that the suction, which results in back-streaming of the melt, appears to reduce as the angular mismatch between the gas jets and the melt nozzle external wall increases. Therefore, under the conditions considered above, it conclude that increasing the nozzle wall mis-match angle as well as gas pressure beyond 1 MPa, the chance of back-stream flow is significantly reduced. This situation occurs due to the gas being overexpanded when exiting the C-D gas exit jet, wherein further expansion will occur beyond the exit such that no negative pressure region occurs near the external wall of the melt delivery nozzle (Figure 103).

According to the above-mentioned results; the CFD results and commonly observed experience, back-stream flow is unlikely to occur for a closed coupled gas atomizer with cylindrical choked gas jets due to the choked flow within the jet-giving rise to rapid expansion of the gas upon exiting the die.

To sum up, it believes that for nozzles type 1 and 12 at an atomization gas pressure of 1 MPa (Figure 102), the back-stream flow happens due to the physical distance between the position of exit jet of the C-D gas die and external wall of the melt delivery nozzle. This phenomenon was not observed in the case of flow separation problem discussed in section 7-2, in which the gas boundary layer separation highly relates to the gas travel distance or melt delivery tip length where the greater given distance to the boundary layer flow distance, the greater flow separation occurs. So investigating the effect of decreasing the physical distance of the C-D gas jet die from external nozzle wall may give an optimum distance in which no back streaming occur.

Base on CFD results in section 6-3-2, with changing the physical distance of C-D gas die from 1.65 mm to the closer position of external nozzle wall (Figure 104), the chance of back streaming decreases. The summery result of changing this distance is given in table 10. In type 1, the safe distance of gas exit die from external nozzle wall is observed at 1.44 mm. This distance in type 12 is measured at 1.64 mm. it can propose that for decreasing the chance of DPJA with the C-D gas die, the gas distance from melt external wall should be designed less than 1.45 mm .

Table 10.The relation between gas die exit distance and nozzle type.

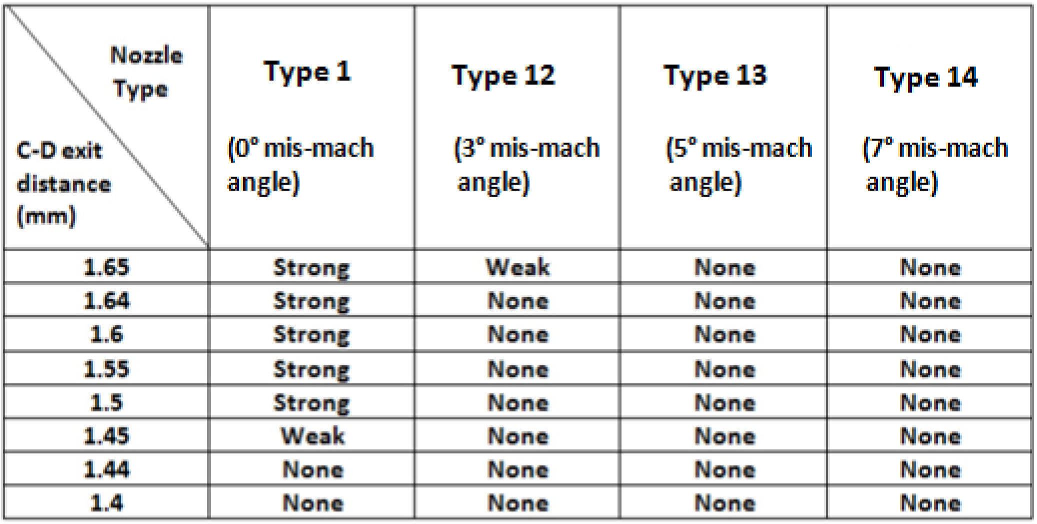

Nozzle Type C-D exit distance (mm)	Type 1 (0° mis-mach angle)	Type 12 (3° mis-mach angle)	Type 13 (5° mis-mach angle)	Type 14 (7° mis-mach angle)
1.65	Strong	Weak	None	None
1.64	Strong	None	None	None
1.6	Strong	None	None	None
1.55	Strong	None	None	None
1.5	Strong	None	None	None
1.45	Weak	None	None	None
1.44	None	None	None	None
1.4	None	None	None	None

8 Conclusions

This thesis has investigated the gas flow field changes at close-coupled gas atomization with different melt delivery nozzle design and gas die system by series of numerical and optical technique such as CFD and Schlieren methods. The results of these experiments have drawn number of conclusions, which are listed below:

8.1 Schlieren technique and analogue atomizer

Use of combination of high-speed imaging and optical Schlieren technique for observing the gas flow pattern around melt delivery nozzle with an analogue atomizer has revealed invaluable results of open and closed-wake condition for different melt delivery nozzle geometry and two types of gas die system. The Schlieren results were also used for validation of the CFD results of gas-only flow experiments for the equivalent melt delivery nozzles. The Schlieren results for nozzle set 1 with cylindrical gas die showed the WCP occurred at lower gas pressure for type 3 and 4 compared to 1 and 2. The same results were also observed for nozzle set 2 where the lowest WCP was measured for type 7 with no lip around the nozzle. Moreover, the Schlieren images of the C-D gas die showed open-wake condition at over and underexpanded conditions up to gas pressure of 5 MPa.

8.2 CFD results of gas-only flow investigation

Use of CFD methods for investigation the gas flow field behaviour around melt nozzle at CCGA process helped better understanding of open to closed-wake condition with varying the melt nozzle tip design. The CFD investigation was done for different melt delivery nozzle at different gas atomization pressure as a different boundary conditions.

The results showed that the numerical model with proposed tested boundary conditions satisfied the numerical validation process and can be validated with experimental tests. To confirm this, nozzle type 4 has been chosen as a reference and the position of Mach disk in CFD result was compared with its Schlieren result at the same condition, which showed a good similarity.

In addition, in this research the conservation equations were solved with two turbulent models of *k*-ε and *k*-ω. The sensitivity of the numerical model was tested with these models and *k*-ω turbulent model, which has been shown previously to be a reliable model for internal flows of this kind, has been chosen as turbulence model for the numerical solutions in all the studies.

8.3 The effects of gas die design on WCP

According to the CFD and the experimental results of choked die, the closed-wake condition achieved with different melt nozzles design at the moderate atomization gas pressures below of 4.5 MPa. On the other hand, the C-D gas die tested in this investigation was designed to operate an ideal flow condition at the gas pressure of 3 MPa and expected to reach to closed-wake condition at higher gas pressures of 3.5 MPa, but the closed-wake condition observed in this gas die at the gas pressures above of 5 MPa. This condition in the atomizer industries may have some advantages and disadvantages.

Previous investigations by Ting et al. [50] on atomizing the Ni base alloy showed that atomizing at the pressure just above of WCP produces finer powder size distribution, lower melt flow rate and higher GMR compared to atomization at open-wake condition which is less efficient. Consequently, use of choked gas die with regardless of melt nozzle design leads to achieve the closed-wake condition at a lower gas pressure (lower WCP) compared to the C-D gas die. On the other hand, the C-D gas die produces more collimated gas jet wave with almost constant supersonic jet in velocity, which has more energy to disintegrate the metal stream at the primary break up situation. However, atomizing at the higher pressure and closed-wake condition causes more gas consumption (higher GMR) and therefore, increases the production cost. Thus, based on results of this investigation the C-D gas jet die should be designed at operating pressures above of 5 MPa. This condition can be achieved by changing the throat and exit area ratio. Doing this with keeping the specific internal dimensions of C-D die with manufacturing tolerance is very difficult. Although, operating the atomizer at such high gas pressures and closed-wake condition may produce finer particles, but it increases the production cost as well. Finding the appropriate condition for choosing the right gas jet system of choked or C-D gas die is a challenging effort for industries.

8.4 Open to closed-wake formation with different melt nozzle tip design and two gas dies

The CFD results helped better understanding of open to closed-wake conditions for different melt nozzles and gas dies. This research proposed a new explanation of open and closed-wake condition regarding to the melt tip and gas die design variation. The previous model proposed by Ting et al. [50] showed only the sketch view of what happen during open to closed-wake condition at gas-only operation with a C-D gas die and a flat tip melt nozzle base on Schlieren images and it was not supported by CFD investigation. However, the model proposed in this research explains the open and closed-wake condition regarding to gas die and melt tip design variation in more details and is supported by the CFD modelling results.

Nozzle type 1 was selected as a reference and the gas velocity field and the streamlines were compared at the same pressure. It was found that, the closed-wake condition occurs when the convex-lens shape expanding gas wave expands gradually by increasing inlet gas pressure until it pinches-off the recirculation zone. This mechanism for both gas dies and nozzles was observed.

Comparison between the velocity field of the choked and C-D gas die at the same inlet gas pressure and type 1 showed that the convex-lens shape over or underexpanded gas wave is more collimated compared to the expanding gas wave with the cylindrical choked gas die. It also noted that the coupling of force balance between recirculation zone and expanding gas wave plays as a restriction zone against the gas expansion. Therefore, the expanding gas wave in the choked die pinches-off the recirculation zone at a lower gas pressure (lower WCP). This phenomenon explains why the WCP occurs for the C-D gas die at the higher gas pressures.

In addition, comparing the velocity field between nozzle type 1 and 4 with the choked or C-D gas die, showed the melt tip profile design affects the shape and length of the recirculation zone. As a result, hemispherical melt tip shape (Type 4) helps the convex-shape expanding wave expands further downward to the recirculation zone and pinches-off this region at a lower gas pressure (lower WCP). This condition was followed in types 2, 3, 5 and 6 with the same mechanism.

The nozzle type 7 with no lip and lowest WCP, confirmed that the how the recirculation zone can affect the open and closed-wake condition. In this nozzle, the convex-lens shape expanding gas wave is less influenced by the upcoming gas from the recirculation zone and as a result; the recirculation zone is pinched-off by expanding gas at the lowest WCP.

8.5 CFD of flow separation

For investigating the flow separation problem at different gas pressure, four melt nozzles (Types 8 to 11) with different melt tip length were designed numerically. The CFD results showed that at the gas pressure of 0.5 MPa no flow separation occurred around melt tip external wall for each of nozzles while at higher gas pressure of 1 MPa the separation observed for type 10 and 11 with nozzle tip length of 7.5 and 10 mm, respectively. It was also found that the negative pressure zone around the melt tip at this pressure may suck the molten metal from melt tip and causes sudden solidification. In addition, the results showed that no flow separation happened in type 10 at the gas pressures above 2 MPa and 2.5 MPa in type 11.

It is concluded that, the atomization gas pressure and the melt tip protrusion length influence the separation point. The separation problem is more likely to happen for these specific melt tip design at gas pressures below of 2.5 MPa and with nozzle tip length of 7.5 mm and above. On the other hand, base on previous results on relation between the WCP and melt tip protrusion length, finding the appropriate melt tip length design to consider both of the flow separation problem and gas wake condition are a challenge for atomizer industries. Moreover, the new solution also proposed with designing some series of dimples at external wall of melt nozzle to decrease the flow separation problems. More investigation on number and shape of those dimples is also proposed for the future works.

8.6 CFD results of Discrete Jet Pressure Inversion

In this research, the effect of changing the angular mis-match angle between the external wall of the melt nozzle and the gas jet line on back-stream flow problem with a C-D discrete gas die was numerically investigated. The results compared with the experimental PLI images obtained with an analogue water atomizer. The nozzle type 1 with zero mis-match angle has been chosen as a reference and compared with the three different melt nozzles (Types 12, 13 and 14) with the mis-match angles of 3, 5 and 7 degree, respectively.

The numerical results of single phase gas flow predicted that for discrete C-D gas die with exit distance of 1.65 mm, the nozzle type 1 (zero mis-match angle) showed the highest back-stream flow (DJPI) around external melt delivery nozzle at the gas pressure of 1 MPa. This situation was also approved by PLI images technique. With increasing the mis-match angle this effect decreased and a weak back-stream flow was observed in type 12 and no back stream was seen in nozzle types 13 and 14. In addition, the effect was totally suppressed at gas pressure above 1 MPa for these particular melt nozzle designs.

Moreover, decreasing the distance between the gas jets and the wall of melt delivery nozzle could sharply reduce the back-stream effect for nozzle types 1 and 12. The maximum gas jet exit distance in which no back-stream flow (DJPI) was predicted for nozzle type 1 was 1.45 mm and this number for nozzle type 12, was 1.64 mm.

Base on these results, the 1.65 mm distance of gas jet to the external wall of nozzle type 1 causes a strong back stream problem. So decreasing this distance can reduce this problem, but designing a desecrated C-D gas die close to the external nozzle wall with keeping the specific dimensions of throat and exit area of die with manufacturing tolerance is very challenging. Use of nozzles with a mis-match angle as much close to types 13 and 14 maybe the solution, but changing the mis-match angles may affect the apex angle of gas jet and influences the other atomization parameters such as mean particle sizes and standard deviations. Consequently, finding an appropriate relation between these parameters in gas die and nozzle design is a challenging effort for the atomizer industries.

9 Future works

More investigation with CFD modelling on melt tip internal shape geometry especially types 4 and 6 on open and closed wake condition is proposed for future work. The internal shape can be changed by designing different conical shape for type 4 and 6 to observe the effect of that on recirculation zone shape and WCP. In addition, CFD modelling of two-phase flow of gas-liquid interaction with different melt nozzles geometry can be very interesting in result to observe more realistic situation at CCGA process. Moreover, the gas flow separation at external wall of melt nozzles with designing different dimples in shape and numbers is another interesting research, which proposed for future work.

References

1. Sheppard.L ,"The powder metallurgy industries worldwide 2007-2012", Materials technology publication, September 2012.

2. White.D.G," Powder metallurgy concept "Advances in Powder Metallurgy and Particulate Materials, MPIF Ed, USA, Part 1, pp 1-12, 2002.

3. Takeuchi.K, the P/M Materials from the View Point of Environment, Proceedings of 2000 Powder Metallurgy World Congress, Kyoto, Japan, JPMA Ed, 2000.

4. Franz.H, Plochl.L and Hohmann.M, "Vacuum system and technologies for metallurgy heat treatment", Vacuum Technologies GmbH Millennium Steel, 2007.

5. Minagawa.K, Kakisawa.H, Takamori.S, Osawa.Y and Halada. K, "Hybrid atomization method suitable for Fabrication of Fine Spherical Lead-Free Solder Powder", Advances in Powder Metallurgy and Particulate Materials, **vol 10**, pp.1-6, 2006.

6. Otaigbe.J and Mcavoy.J,"Gas atomization of polymers, feasibility studies and process development**",** Advances in Polymer Technology, **vol 17**, No. 2, pp.145-160, 1998.

7. Zhoa.Y, "Considerations in Designing a Centrifugal Atomizer for Metal Powder Production", Materials and Design, **vol** 27, pp.745-750, Sept 2005.

8. Anderson.I.E, Filogliola.R.S. and Morton.H,”Flow mechanisms in high pressure gas atomization”, Materials Science and Engineering, **vol 148**, pp.101-114, 1991.

9. Mates.S and Settles.G.S,”High speed imaging of liquid metal atomization by two different close-coupled” Advances in Powder Metallurgy and Particulate Materials Part 1, Metal Powder Industries Federation, Princeton, pp.15-29, 1995.

10. Ting.J, Peretti.M and Eisen.W,” The effect of wake-closure phenomena on gas atomization performance”, Materials Science and Engineering, **vol 326**, pp.110-121, 2002.

11. Anderson.I.E, Terpstra.R.L, and Figliola.R.S,”Visualization of Enhanced Primary Atomization for Powder Size Control,” in Advances in Powder Metallurgy and Particulate Materials,2005, compiled by C. Ruas and T. A. Tomlin,Metal Powder Industries Federation, Princeton, NJ, Part 2, pp.1-17, 2005

12. Lawley.A, “Atomization, the Production of Metal Powders”, MPIF, Princeton, NJ, pp.102-107, 1992.

13. Jiang.G, Hemein. H and Siegal, M.V, ”Intelligent sensor for atomization processing of molten metals and alloy”, Technical report, defence technical information centre, June 1998.

14. Grant,P.S. Solidification in spray forming. Metall. Mater. Trans, **vole 38**, pp.1520-1529, 2005.

15. Savart.F, Ann. Chim. 53, 337; plates in **vol 54**, 1833.

16. Plateau. J, Acad. Sci. Bruxelles M´em. XVI, 3, 1843.

17. Rayleigh,L ,“On the stability of jets “Processed of the London mathematical society, **vol 10**, pp.4-13, 1878.

18. Eotvos. L, Wied. Ann. 27, 448, 1886.

19. Quincke. G. H, Wied. Ann. 2, 145, 1877.

20. Lenard. P, Ann. Phys, 30, 209, 1887.

21. Bohr. N., Phil. Trans. Roy. Soc, A 209, 281, 1909.

22. Kuehn.R,”Atomization of liquid fuels”, T.M, Nos, N.A.C.A, pp.329-331, 1925.

23. Weber.G,”ZumZerfall eines Flussigkeitsstrahels”,Zeitschrift fure,angewandte mathematic and mechanic, **vol 11**, pp.136-154, 1931.

24. Dejuhasz.K.J,”Dispersion of sprays in solid injection oil engines“, Trans .A.S.M.E, pp.53-65, 1931.

25. Laufer.J,”Investigation of turbulent flow in a two-dimensional channel”,

Tech. Note 2123, Natl. Adv. Comm. For Aeronaut, Washington, D.C, 1950.

26. Ranz.W, on sprays and spraying. Dep. Eng. Res, Penn State University, pp.53-65, 1956.

27. Tennekes,H. and Lumley.J.L.,“A First Course in Turbulence”, Cambridge, MA: MIT Press, ISBN 0-262-20019-8, 1972.

28. Hinze,J.O. Turbulence, McGraw-Hill, New York, 1975.

29. Schlichting.H, Boundary layer theory, 7th ed. McGraw-Hill, New York, 1979.

30. Koalewski,T.A, ”On the separation of droplets from a liquid jet”, Fluid dynamics research, **vol 17**, pp.121-145, 1996.

31. Fargo,Z and Chigier.N,”Morphological classification of disintegration of round liquid jet in coaxial air stream”, Atomization and spray, **vol 2**, pp.203-214, 1993.

32. Frazer.R.P and Eisenklam, P,”Reserch into performance of atomization for liquids”, Imperial college chemical engineering society journal, **vol 7**, pp.52-68, 1953.

33. Mansour.A. and Chigier.N,” Disintegration of liquid sheets”, Physics of fluid A, **vol 2**, pp.706-719, 1990.

34. Carvalho.I.S, Heitor. M.V,”Liquid film break-up in a model of a pre-filming airblast nozzle,”Experiments in Fluids”, **vol 24**, pp.405-415, 1998.

35. Gifen.E, and Muraszew.A,”Shock tube investigation of the break-up of drops by air blast”, The Atomization of Liquid Fuels, **vol 6**, pp.1070-1080, 1953.

36. Hinze.J,"Fundamental of the hydrodynamic mechanism of splitting in dispersion process", AICHE, **vol 1**, pp.289-295, 1955.

37. Hsiang,L.P,Feath,G,M,,"Near limit drop formation and secondary breakup ", International journal of multiphase flow, **vol 18**, pp.635-652, 1992.

38. Ranger.A.A, and Nicholls.J,"Aerodynamic shattering of liquid drops", AIAAJI, **vol 7**, pp.285-290, 1969.

39. Dai.Z and Faeth.G.M,"Temporal properties of secondary drop breakup in the multimode breakup regime", International journal of multiphase flow, **vol 27**, pp.217-236, 2001.

40. Thompson.J.S, "A Study of Process Variables in the Production of Aluminium Powder by Atomization ", J. Inst. Metal., **vol 74**, pp.101–132, 1948.

41. Anderson.I.E, Byrd.D and Meyer.J," Highly tuned gas atomization for controlled preparation of coarse powder", Mat.-wiss. U.Werkstofftech, **vol 41**, pp.504-512, 2010.

42. Anderson.I.E, and Terpstra.R.L,"Progress toward gas atomization processing with increased uniformity and control", Material science and engineering A, **vol 27**, 326, pp.101-109.

43. Anderson.I.E, Morton.H and Figliola.R.S,"Flow mechanism in high pressure gas atomization", Material science and engineering, **vol 148**, pp.101-114, 1991.

44. Miller,S.A, "Apparatus for melt atomization with a concave melt nozzle for gas deflection", United state patent, 1986.

45. Mates.S.P, Settles.G.S," A study of liquid metal atomization using close coupled nozzles", Atomization and spray, **vol 15**, pp.20-27, 2005.

46. Mates.S.P and Settles.G.S,"A study of liquid metal atomization using close-coupled gas atomization", Part1, Atomization and spray, **vol 15**, pp.19-40, 2005.

47. Anderson.I.E, Figliola.R.S and Morton.H," Flow mechanisms in high pressure gas atomization", Materials science and engineering A, **vol 148**, pp.104-114, 1991.

48. Ting.J, Anderson.I.E, Terpstra, R.L, and Mi. J," Design and testing of an improve convergent-divergent discrete jet high pressure gas atomization nozzle" Advances in powder metallurgy and particulate materials, **vol 3**, pp.105-1112, 1998.

49. Srivastava.V.C, Ojha.S.N,"Effect of processing Variables on Particle size during Inert Gas Atomization Process", Powder Met. Sci. & Tech. B, **vol 13,** No.3, pp.5-9, 2001.

50. Ting.J, Peretti.M.W and Eisen.W.B,”The effect of wake-closure phenomenon on gas atomization performance”, Material Science and engineering, **vol 326**, pp.110-121, 2002.

51. Anderson.I.E and Figliola.R.S,”Observations of Gas Atomization Process Dynamics in”, Modern Developments Powder Metallurgy, **vol 20**, pp.205-223, 1998.

52. Unal,A,”Influence of gas flow on performance of confined atomization nozzle”, Metallurgy transaction B, **vol 20**, pp.833-843, 1989.

53. Anderson.I.E, Terpstra.R.L, and Figliola.R.S,”Melt feeding and nozzle design modification for enhanced control of gas atomization”, Advances in powder metallurgy an particulate materials, **vol 2**, pp.26-30, 2004.

54. Ting. J, Anderson. I. E and Terpstra. R, ”Optimizing melt tip geometry for high pressure atomization ”, Advances in powder metallurgy and particulate materials, **vol 3**, pp.53-63, 1997.

55. Nilsson. E.O. F and Hagelin. E.G, Nilsson. S. I, US patent 2997245, **vol** 23 August 1961.

56. Miller.S.A, and Strauss.J.T.E,”Use of two-phase flow aspiration pressure for improved close-coupled nozzle performance”, Metal Powder report 57, **vol 6**, pp.58-68, 2002.

57. McCarthy.I.N, Adkins N.J, Aslam Z, Mullis A. M. and Cochrane1 R. F, “High speed imaging and Fourier analysis of the melt plum during closed coupled gas atomization, Powder Metallurgy, **vol 52**, No 3 pp. 205-212, 2009.

58. McCarthy.I.N,”Optical investigations into close-coupled gas atomization”, PhD thesis, University of Leeds, 2010.

59. Mille.S.A, Savkar.S, and Miller.R.S, ”Global and Midfield Imaging of Liquid Metal Atomization”, in A. Lawley and A. Swanson (compilers), Advances in Powder Metallurgy and Particulate Materials, Metal Powder Industries Federation, Princeton, NJ, pp.25-34, 1993.

60. Unal.A,”Flow separation and liquid rundown in a gas atomization process”, Metallurgical transaction B, **vol 20**, 1989.

61. Mates.S.P and Settles. G,”A flow visualization study of the gas dynamic of liquid metal atomization”, Advances in Powder Metallurgy and Particulate Materials, Part 2, Metal Powder Industries Federation, Princeton, NJ, 1995.

62. Settles.G,”Schlieren and shadowgraph techniques: Visualizing phenomena in transparent media”, Berlin: Springer-Verlag, 2001.

63. Anderson.I.E and FigliolaR.S,”Modern Developments in Powder Metallurgy”, P.U. Gummeson and D.A. Gustafson, Editors, MPIF, Princeton, NJ, pp.205-210, 1988.

64. Thomas.S, ”A Study of Process Variables in the Production of Aluminium Powder by Atomization”, J. Inst. Metal., **vol 74,** pp.101-132, 1948.

65. Wigg,L.D,"Drop-size prediction for twin-fluid atomisers", J.Inst. Fuel **vol 11**, pp. 46-52, 1964.

66. Lubanska.H,"Correlation of spray ring data for gas atomization of liquid metals", J. Metals, **vol 22**, pp.45-49, 1970.

67. Strauss.J.T,"Close-Coupled Gas Atomization Using Elevated Temperature Gas", Advances in Powder Metallurgy and Particulate Material, Part 1, Metal Powder Industries Federation, Princeton, NJ, 2000.

68. Issa.R.I, and Oliveira.P.J,"Numerical prediction of phase separation in two-phase flows through T-junctions", Computers and Fluids, **vol 23**, pp.347-372, 1994.

69. EspinaP.I, Piomelli. U," Numerical simulation of the gas flow in gas-metal atomizers", In Proceedings of FEDSM'98, 1998 ASME fluids engineering, division summer meeting, Washington, DC, USA, pp.21-25, 1998.

70. Hess.J.and Smith.L.A, "Calculation of potential flow about arbitrary bodies", Progress in Aeronautics Sciences, **vol 8**, pp.1-138, 1967.

71. Launder.B.E. and Spalding.D.B., The Numerical Computation of Turbulent Flows, Computer Methods App. Mech., pp. 269-275.

72. Gosman,A.D., Khalil.E.E. and Whitelaw.J.H."The Calculation Of Two Dimensional Turbulent Recirculating Flows", Proc. Symposium On Turbulent Shear Flows, **vol 1**, pp .237-255, 1979

73. Bradley.D, ”On the atomization of liquids by high-velocity gases”, Part one J. Phys. D: Appl. Phys, **vol 6,** pp.1724–1736, 1973.

74. Markus.S, Fritsching.U and Bauckhage.K, “Jet break up of liquid metals”, Materials Science Engineering A, **vol 326**, pp.122-133, 2002.

75. Scardovelli.R, Zaleski.S,”Direct numerical simulation of free- surface and interfacial flow”, Annu. Rev, Fluid Mech, **vol 31**, pp.567-603, 1999.

76. Thomas.B, Boeck.T, and Zaleski.S,”Numerical simulation of liquid-gas Interfaces with applications to atomization”, Processings of XXI congress of theoretical and applied machanics,Warsaw,Ploland, pp.15-21, 2004.

77. Li.J, Lopez.E, Yecko.P and Zaleski.S,**”**Ligament formation in sheared liquid-gas layers”, Theor. Compute. Fluid Dynamics, **vol 21**, pp.59-76, 2007.

78. Tong.M, and Browne.D,”Direct numerical simulation of melt–gas hydrodynamic interactions during the early stage of atomisation of liquid intermetallic”, Journal of Materials Processing Technology, **vol 202**, pp.419-427, 2008.

79. Mi.J, Figliola.R.S, and Anderson. I.E, ”A numerical simulation of gas flow field effects on high pressure gas atomization due to operating pressure variation”, Materials Science and engineering, **vol 208**, pp.20-29, 1996.

80. Mi.J, Figliola.R.S, and Anderson. I.E,”A numerical investigation of gas flow effect on high pressure gas atomization due to melt tip geometry variation”, Metallurgical and Materials transactions B, **vol 28B**, pp.935-941, 1997.

81. Xinming.Z, XU Jun, ZHU Xuexin, ZHANG Shaoming, “Effect of atomization gas pressure variation on the gas flow field in the supersonic gas atomization”, Science in China Series, **vol 52**, pp.3046-3053, 2009.

82. Ting. J, and Anderson.I.E,”Computational fluid dynamics investigation of wake closure phenomena “, Material science and engineering, **vol 379**, pp.264-276, 2004.

83. Zeoli.N, and Gu.S,”Computational validation of an isentropic plug nozzle design for gas atomization”, Computational Material Science, **vol 42**, pp.245-258, 2008.

84. Zeoli.N and Gu.S,”Numerical modelling of droplet break-up for gas atomisation”, Computational Materials Science, **vol 38**, pp.282-292, 2006.

85. Wenxiang.C,”Applying Numerical Simulation to Analyse the Performance of Nozzles”, International Conference on Energy and Environment Technology,**vol 38**, pp.207-210, 2009.

86. Tong.M, and Browne.D.J,”Modelling compressible gas flow near the nozzle of a gas atomiser using a new unified model”, Computer and Fluids, **vol 38**, pp.1183-1190, 2009.

87. Aydin.O,”Experimental and numerical modelling of the gas atomization nozzle for gas flow behaviour”, Computers & Fluids, **vol 42**, pp.37-43, 2011.

88. Fluent 6.1 User’s Guide, Fluent Inc, Centerra Resource Park, 10 Cavendis Court, Lebanon, NH 03766, USA, 2003.

89. Fluent Inc., GAMBIT User’s Guide, Fluent Inc., Lebanon; 2002.

90. White FM. Fluid mechanics. 2nd McGraw-Hill Book Co, 1988.

91. Yakhot.V and Smith. L. M,”The Renormalization Group, the e-Expansion and Derivation of Turbulent Models”, to appear in Journal of Science & Computer, 1992.

92. Kolmogorov.A.N,”Equations of turbulent motion of an incompressible fluid”, Izv Akad Nauk SSR Ser Phys, **vol 1/2**, pp.56-70, 1942.

93. Saiy.M,”Turbulent mixing of gas streams”, PhD Thesis, Imperial College, University of London, 1974.

94. SpaldingD.B,”Mathematical models of turbulent transport processes”, HTS/79/2, Imperial College, Mech.Eng.Dept, 1979.

95. Wilcox.D.C,"Reassessment of the scale determining equation for advanced turbulence models", AIAA J, **vol 26**, No.11, pp.1299-1304, 1988.

96. Speziale.C.G, Abid.R and Anderson.E.C,"A critical evaluation of two-equation turbulence models for near-wall turbulence", AIAA Paper 90, pp.1481, 1990.

97. Menter.F.R,"Improved two-equation k-ω turbulence model for aerodynamic flows", NASA TM-103975, 1992.

98. Georgia Tech http://www.ae.gatech.edu/people/ejohnson/ae1350-Fall2007/13rockets.